NUREG/CR-3998 Vol. I
ANL-84-60 Vol. I

NUREG/CR-3998 Vol. I
ANL-84-60 Vol. I

LIGHT-WATER-REACTOR SAFETY MATERIALS ENGINEERING RESEARCH PROGRAMS: QUARTERLY PROGRESS REPORT

January – March 1984

ARGONNE NATIONAL LABORATORY, ARGONNE, ILLINOIS
Operated by THE UNIVERSITY OF CHICAGO

Prepared for the Office of Nuclear Regulatory Research
U. S. NUCLEAR REGULATORY COMMISSION
under Interagency Agreement DOE 40-550-75

Argonne National Laboratory, with facilities in the states of Illinois and Idaho, is owned by the United States government, and operated by The University of Chicago under the provisions of a contract with the Department of Energy.

NUREG/CR-3998 Vol. I
ANL-84-60 Vol. I

Distribution
Code: R5

ARGONNE NATIONAL LABORATORY
9700 South Cass Avenue
Argonne, Illinois 60439

LIGHT-WATER-REACTOR SAFETY MATERIALS ENGINEERING RESEARCH PROGRAMS: QUARTERLY PROGRESS REPORT

January—March 1984

Date Published: September 1984

Previous reports in this series

ANL-83-85 Vol. I	January—March 1983
ANL-83-85 Vol. II	April—June 1983
ANL-84-36	October 1982—September 1983
ANL-83-85 Vol. IV	October—December 1983

Prepared for the Division of Engineering Technology
Office of Nuclear Regulatory Research
U. S. Nuclear Regulatory Commission
Washington, D. C. 20555
Under Interagency Agreement DOE 40-550-75

NRC FIN Nos. A2212, A2243, A2250

LIGHT-WATER-REACTOR SAFETY
MATERIALS ENGINEERING RESEARCH PROGRAMS:
QUARTERLY PROGRESS REPORT

January-March 1984

ABSTRACT

This progress report summarizes work performed by the Materials Science and Technology Division of Argonne National Laboratory during January, February, and March 1984 on water reactor safety problems. The research and development areas covered are Environmentally Assisted Cracking in Light-Water Reactors, Long-Term Embrittlement of Cast Duplex Stainless Steels in Light-Water-Reactor Systems, and Nondestructive Evaluation and Leak Detection.

NRC Fin No.	FIN Title
A2212	Environmentally Assisted Cracking in Light-Water Reactors
A2243	Long-Term Embrittlement of Cast Duplex Stainless Steels in LWR Systems
A2250	Nondestructive Evaluation and Leak Detection

TABLE OF CONTENTS

		Page
EXECUTIVE SUMMARY		v
I.	ENVIRONMENTALLY ASSISTED CRACKING IN LIGHT-WATER-REACTORS	1
	A. Long-term Aging and Analysis of Reactor Components (J. Y. Park)	2
	B. Crack Growth Rate Studies (J. Y. Park and W. J. Shack)	4
	1. Introduction	4
	2. Technical Progress	5
	C. Evaluation of Nonenvironmental Corrective Actions (P. S. Maiya and W. J. Shack)	11
	1. Introduction	11
	2. Technical Progress	12
	a. Impurity and Strain Rate Effects	12
	b. Stress/Strain/Strain-rate Relations for Sensitized Materials	19
	c. Residual Stress Measurements	22
	D. Evaluation of Environmental Corrective Actions (W. E. Ruth[illegible], W. K. Soppet, and T. F. Kassner)	30
	1. Introduction	30
	2. Technical Progress	30
	a. Source of Anion Impurity Species and Their Effect on SCC Susceptibility	30
	b. Effect of Temperature on SCC Susceptibility	38
	E. References for Chapter I	49
II.	LONG-TERM EMBRITTLEMENT OF CAST DUPLEX STAINLESS STEELS IN LWR SYSTEMS (O. K. Chopra and H. M. Chung)	52
	A. Material Characterization and Mechanical Tests	53
	B. Microstructural Characterization of the Aged Material	59
	1. Characterization of Precipitates in Aged Cast Duplex Stainless Steel	59

TABLE OF CONTENTS (Contd.)

		Page
	2. SEM Fractographic Characteristics.....	61
	C. References for Chapter II.....	68
III.	NONDESTRUCTIVE EVALUATION AND LEAK DETECTION (D. S. Kupperman, T. N. Claytor, and R. N. Lanham).....	69
	A. Objectives.....	70
	B. Ultrasonic NDE for Cast Stainless Steel.....	70
	1. Variation of Sound Velocity with Microstructure.....	71
	2. Microstructure and Deviation of Ultrasonic Beams.....	75
	C. Distinguishing Intergranular Cracks from Geometrical Reflectors.....	78
	D. References for Chapter III.....	85

LIGHT-WATER-REACTOR SAFETY
MATERIALS ENGINEERING RESEARCH PROGRAMS:
QUARTERLY PROGRESS REPORT

January-March 1984

EXECUTIVE SUMMARY

I. ENVIRONMENTALLY ASSISTED CRACKING IN LIGHT-WATER REACTORS[a]

Cracks in the heat-affected zones of weldments in austenitic stainless steel piping and associated components in boiling water reactors (BWRs) have been observed since the mid-1960s. Since that time cracking has continued to occur, and indications have been found in all parts of the recirculation system including the largest diameter lines. Proposed remedies include procedures that produce a more favorable compressive residual stress state at the inner surface of the pipe at the welds, replacement with materials that are more resistant to stress corrosion cracking (SCC), and changes in the reactor coolant environment that decrease susceptibility to cracking. The overall objective of this program is an independent evaluation of these remedies. The main areas of investigation during this quarter are (1) impurity effects on the SCC susceptibility of conventional and nuclear grades of austenitic stainless steel, (2) crack growth rate measurements, (3) finite-element studies and experimental measurements of residual stresses in weldments with weld overlays, and (4) the effects of long-term, low-temperature aging.

Additional information has been obtained on the SCC behavior of Type 304 SS and Type 316 NG materials in constant extension rate tensile (CERT) experiments in 289°C water containing dissolved oxygen and impurity species at low concentrations. In the case of lightly sensitized Type 304 SS, various anion species, present either as acids or as sodium salts (total conductivity values of ≤ 1 μS/cm), differ considerably in their effects on the IGSCC behavior of the steel. Sulfur species, namely sulfate, sulfite, thiosulfate, and sulfide, were found to be the most deleterious of the ~12 anions that were

[a]RSR FIN Budget No. A2212; RSR Contact: J. Strosnider.

evaluated. The effect of temperature on the SCC behavior of lightly sensitized Type 304 SS was investigated over the range of 110 to 320°C in high-purity water and in water containing 0.1 and 1.0 ppm sulfate (added as H_2SO_4) at a dissolved oxygen concentration of 0.2 ppm. In high-purity water ($\lesssim$0.2 μS/cm) the greatest IGSCC susceptibility occurs at temperatures between ~200 and 250°C. Sulfate additions to the feedwater increased both the degree of susceptibility and the temperature range over which maximum susceptibility occurs. The crack-growth-rate data and fracture mode of specimens in the CERT experiments were correlated with the electrochemical potential of the steel.

CERT tests on Type 316 NG stainless steel in high purity water at 289°C with a dissolved oxygen concentration of 0.2 ppm showed no evidence of SCC. Since transgranular SCC occurred in previous tests with 0.1 ppm sulfate (added as H_2SO_4), these results confirm that impurities play a critical role in the cracking process. Currently experiments are being performed at sulfate levels between 0.01 and 0.05 ppm to determine the concentration necessary to produce IGSCC. A phenomenological model for stress corrosion crack growth has been developed which provides a method to extrapolate the CERT results to very low strain rates ($\leq 10^{-8}$ s^{-1}). The model appears to be valid for both intergranular and transgranular cracking in a number of environments.

Measurements of through-wall residual stresses have been made on 12-in. schedule 100 pipe (supplied by Georgia Power and NUTECH) with a standard weld overlay that was prepared using procedures identical to those used to repair reactor piping at Hatch-2 . The residual stresses on the inner surface of the weldment were very compressive, and the throughwall distributions were in general agreement with those predicted by finite-element calculations. Although the experimental results confirm the analytical predictions of strongly compressive stress fields on the inner surface of the overlay, other types of tests are needed to verify the predicted stress fields at crack tips.

II. LONG-TERM EMBRITTLEMENT OF CAST DUPLEX STAINLESS STEELS IN LWR SYSTEMS[b]

Metallographic evaluation of various cast materials is in progress to characterize the chemical composition, ferrite content, hardness, and grain structure. The results indicate some differences in hardness and ferrite content for material from different locations of the castings. The ferrite content is lower and the hardness is higher toward the inner surface of the various cast pipes. The hardness of the static-cast keel blocks is higher toward the top of the casting. However, variations in the ferrite content of the cast keel blocks depend on the Cr_{eq}/Ni_{eq} ratio in the material. The grain structure of the centrifugally cast pipes is either equiaxed or columnar (oriented in the radial direction). The cast keel blocks have a mixed structure of equiaxed and columnar grains.

Material for Charpy impact and 1-T compact tension specimens is being aged at 450, 400, 350, 320, and 290°C. The aging times range from 100 to 50,000 h. Charpy-impact tests are in progress on the unaged material and material that was aged up to 1000 h at the different temperatures.

Microstructural evaluation has continued on the aged specimens of cast duplex stainless steel obtained from Georg Fischer Co. of Switzerland. The α' precipitate was not observed in any of the specimens aged for up to 70,000 h at temperatures between 300 and 400°C. However, three different types of precipitates have been identified in these specimens. Characterization of the fracture surfaces of the specimens, which were impact tested at room temperature, is in progress.

---

[b]RSR FIN Budget No. A2243; RSR Contact: J. Muscara.

III. NONDESTRUCTIVE EVALUATION AND LEAK DETECTION[C]

Variations in the velocity of sound have been measured in cast stainless steels with well-characterized equiaxed and columnar grains and in materials with an ill-defined coarse-grain structure. The velocity of sound can be used to distinguish between well-defined equiaxed and columnar structures; however, the variability in the velocity is too large to characterize the microstructure of complex coarse-grain material. A method to distinguish columnar from equiaxed grain structures that incorporates the ultrasonic-wave beam skewing phenomenon is described, and the possibility of using the technique under field conditions is discussed. Information on the detection of intergranular stress corrosion cracks, including field-induced cracks in 28-in. pipe sections, with a multi-element skew angle probe is presented along with results from a field test of the probe.

[C]RSR FIN Budget No. A2250; RSR Contact: J. Muscara.

I. ENVIRONMENTALLY ASSISTED CRACKING IN LIGHT WATER REACTORS

Principal Investigators:
W. J. Shack, T. F. Kassner, P. S. Maiya,
J. Y. Park and W. E. Ruther

The objective of this program is to develop an independent capability for prediction, detection, and control of intergranular stress corrosion cracking (IGSCC) in light-water reactor (LWR) systems. The program is primarily directed at IGSCC problems in existing plants, but also includes the development of recommendations for plants under construction and future plants. The scope includes the following: (1) evaluation of the influence of metallurgical variables, stress, and the environment on IGSCC susceptibility, including the influence of plant operations on these variables; and (2) examination of practical limits for these variables to effectively control IGSCC in LWR systems. The initial experimental work concentrates primarily on problems related to pipe cracking in LWR systems. However, ongoing research work on other environmentally assisted cracking problems involving pressure vessels, nozzles, and turbines will be monitored and assessed, and where unanswered technical questions are identified, experimental programs to obtain the necessary information will be developed to the extent that available resources permit.

The effort is divided into five subtasks: (A) Long-term Aging and Analysis of Reactor Components, (B) Crack Growth Rate Studies; (C) Evaluation of Nonenvironmental Corrective Actions; (D) Evaluation of Environmental Corrective Actions; and (E) Mechanistic Studies. These subtasks reflect major technical concerns associated with IGSCC in LWR systems, namely: the role of materials susceptibility, the role of stress in crack initiation and propagation, and the role of the environment. The program seeks to evaluate potential solutions to IGSCC problems in LWRs, both by direct experimentation (including full-scale welded pipe tests) and through the development of a better basic understanding of the various phenomena.

A. Long-term Aging and Analysis of Reactor Components (J. Y. Park)

Microstructural changes resulting from thermal exposure that produce susceptibility to intergranular corrosion are collectively known as sensitization. It is one of the major causative factors in the IGSCC of austenitic stainless steels in LWR environments. Under normal isothermal heat treatments, sensitization of austenitic stainless steels such as Types 304 and 316 stainless steel (SS) occurs in the temperature range of about 500 to 850°C. However, Type 304 SS may be sensitized at temperatures below this range if carbide nuclei are present at grain boundaries. This low-temperature sensitization (LTS) phenomenon in Type 304 SS has been demonstrated in laboratory experiments in the temperature range from 350 to 500°C. Extrapolations of this behavior to plant operating temperatures (288°C) yield estimated times ranging from 10 to 1000 years for significant LTS to occur. This wide variation has been attributed to differences in the amounts of strain, dislocation densities, and/or impurity element contents of the materials, but with the current level of understanding, the susceptibility to LTS of arbitrary heats of material cannot be assessed.

It is also not clear that the susceptibility to IGSCC produced by long, relatively low-temperature thermal aging can be adequately assessed by conventional measures of the degree of sensitization (DOS), such as the electrochemical potentiokinetic reactivation (EPR) technique or ASTM A262 Practices A through E. These tests have been developed and qualified primarily on the basis of the IGSCC susceptibility produced by high-temperature furnace sensitization or welding.

The objectives of this subtask are to establish the importance of LTS of materials under long-term reactor operating conditions and to evaluate the effect of thermomechanical history on the correlation of IGSCC susceptibility with tests such as the EPR technique and ASTM A262 Practices A through E.

Investigations on the effect of plastic strain on the sensitization behavior of Type 304 SS are continuing. Type 304 SS specimens from Heat Nos. 10285 and 53319 were heat treated at 1050°C for 0.5 h, and at 700°C for 10 minutes in order to nucleate carbide precipitates, and were plastically deformed to 2, 5, and 10% strain levels. The deformed specimens are being aged at 289, 315, 350 and 400°C, along with undeformed control specimens and companion button specimens. EPR values were measured for the companion button specimens after the nucleation heat treatment (700°C/10 minutes). The average value was 5.9 C/cm^2 for Heat No. 10285 and 7.3 C/cm^2 for Heat No. 53319. A larger increase in EPR value after low temperature aging is expected for the deformed specimens compared to the undeformed ones. Preliminary results from short-term high-temperature aging (450-600°C) were reported previously[1] and are consistent with the expected results.

Low-temperature aging of the specimens from 4-inch diameter Type 304 SS (Heat No. 53319) pipe weldments with the IHSI, CRC, HSW, and LPHSW treatment is continuing. The specimens aged at 400°C for 4000 h were taken out for examination. ASTM-262-A and EPR tests will be performed.

Preparation of scanning-transmission-electron-microscopy (STEM) specimens from Type 304 SS (Heat Nos. 10285 and 30956) is continuing. Specimens were furnace-sensitized at a temperature range 600-700°C, which produced EPR values from 2 to 64 C/cm^2. The STEM specimens were prepared by jet electropolishing of thin disks in an electrolyte of 30 vol.% HNO_3 plus 70 vol.% methanol at 20 volts DC, 24 mA/mm^2 and -15 to -20°C. Grain boundary chromium depletion profiles for a sensitized (650°C/4 h, EPR = 11 C/cm^2) specimen from Heat No. 10285 were presented in a previous report.[1] Future STEM work will focus on specimens sensitized by different thermomechanical treatments, particularly LTS. The results from STEM, CERT, EPR and ASTM A262-E will be compared.

The general sensitization behavior of Type 304 SS Heat No. 9T2796 was examined. Heat No. 9T2796 is being considered as an additional heat for the program. This heat of material has been extensively studied in the LMFBR program, and its mechanical and metallurgical properties have been well characterized. EPR values were measured after a solution heat treatment

(SHT) at 1050°C for 30 minutes and aging at 700°C for the time periods between 5 and 240 minutes. The values varied from 0.2 C/cm^2 (SHT plus 700°C/5 min) to 32 C/cm^2 (SHT plus 700°C/240 min).

B. Crack Growth Rate Studies (J. Y. Park and W. J. Shack)

1. Introduction

The early instances of IGSCC in operating BWRs generally occurred in small pipes, and the response to the detection of IGSCC was generally to repair or replace the cracked piping immediately. It is now clear that for reactors with standard Type 304 SS piping material, cracking can occur anywhere in the recirculation system, including the main recirculation line. Because of the severe economic consequences of long forced outages for repair or replacement, utilities must consider other approaches for dealing with cracked pipe. The possibilities include continued operation and monitoring for any subsequent growth for an indefinite period, continued operation and monitoring until a repair can be scheduled to minimize outage, or immediate repair and replacement.

Understanding crack growth behavior is, of course, important for other reasons besides assessing the safety implications of flawed piping. A better understanding would permit a more rational extrapolation of laboratory test results to the prediction of behavior in operating plants. Current work on the measurement of crack growth rates seeks to characterize these rates in terms of the linear elastic fracture mechanics (LEFM) stress intensity as well as the level of sensitization and the amount of oxygen present in the coolant. The work in this subtask is aimed at a systematic evaluation of the validity of the use of LEFM to predict IGSCC growth. The capability of data obtained under one type of loading history to predict crack growth under a different loading history will be investigated. The effect of flaw geometry on crack propagation rates will also be considered.

2. Technical Progress

Crack growth rate tests for furnace-sensitized Type 304 SS (Heat No. 10285) 1TCT specimens (304-C-07, -11, -17) in high-purity water with 8 ppm dissolved oxygen at 289°C were performed. The crack length was monitored throughout the tests by the compliance method using in-situ clip gages. Figure 1.1 shows crack length vs test time for three 1TCT specimens. Interruption or changes in the test conditions (load ratio R, frequency f, or stress intensity K) occurred at points I through XXI. A change in the test conditions often caused retardation of crack growth for about 200-500 hours. Crack lengths for specimens C-09 and C-17 were not measured beyond the point IX, because the clip gages failed. Average crack propagation rates for each test condition were obtained by least-square linear regression analysis. The results were presented in a previous report[2] and are included in Table 1.1 for completeness. The crack growth tests were terminated after an accumulated test time of 14,932 h, because the length of the uncracked ligament in specimen C-11 decreased to 18 mm. Post-test calibration of the clip gage remained within 2% of the initial calibration. Hence no correction is needed for the previously reported growth rates. Crack growth rates varied from 1×10^{-10} to 3×10^{-9} m/s over the range R = 0.5 to 1.0, and f = 1×10^{-1} to 2×10^{-3} Hz, at maximum K = 28-39 MPa·$m^{\frac{1}{2}}$. The cracks propagated faster at low R values than at high R values. However, the growth rate at R = 0.95 was not significantly different from that under constant load. As reported earlier, no significant correlation could be established between the propagation rate and an LEFM estimate of crack-tip strain rate based on the cyclic loading rate ($\dot{\epsilon}_T = -1/T \ln[1 - (1 - R)^2/2]$). The data is being re-examined using an alternative estimate of crack tip strain rate with an additional term for constant load creep deformation at the tip.

The crack surfaces of the specimens were examined after fracturing the uncracked ligament. Large variations in crack length across the thickness of the specimens were observed (Fig. 1.2). The cracks were generally longer at the side surfaces than at the center sections ("inverse thumbnails"). Similar behavior has been observed in other test specimens. Average crack lengths were determined from the areal average of the crack lengths on the exposed surface and compared with the lengths obtained by the

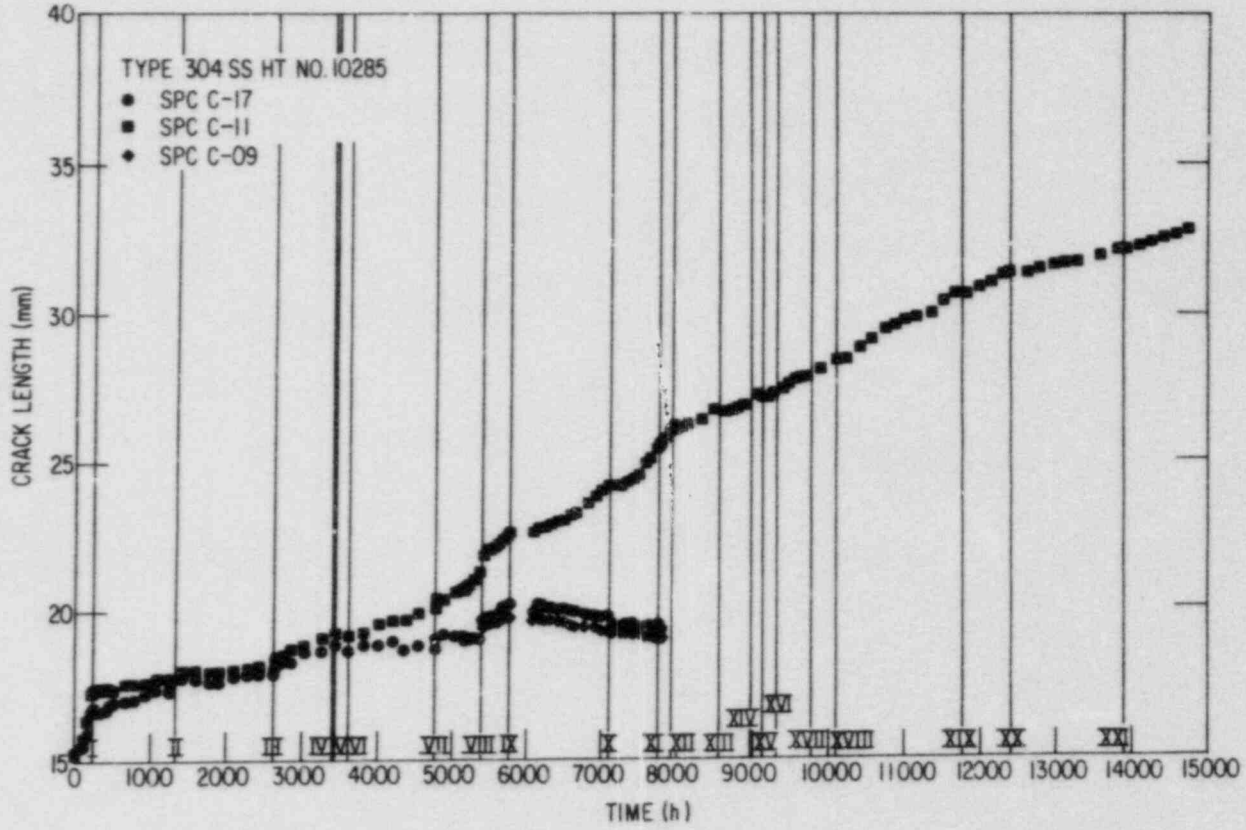

Fig. 1.1. Plots of Crack Length vs Time for Heat No. 10285 Specimens.

TABLE 1.1. Crack Propagation Rates in Type 304 SS Specimens (Heat No. 10285) Sensitized to Two Different Levels and Tested in 289°C Water with 8 ppm O_2

f(Hz)	R	$\dot{\epsilon}_T(s^{-1})$[a]	K_{max} (MPa.$m^{\frac{1}{2}}$)	$\dot{a}$(m/s)	Fracture Mode[b]
		Specimen 300-C-11, EPR = 1.4 C/cm^2			
0	1	-	33-34	1.2×10^{-10}	IG
0	1	-	36-37	2.9×10^{-10}	↓
0	1	-	37-38	4.5×10^{-10}	↓
1×10^{-3}	0.5	1.4×10^{-4}	31-32	2.6×10^{-10}	TG
2×10^{-3}	0.5	2.7×10^{-4}	30-31	8.9×10^{-10}	↓
2×10^{-3}	0.5	2.7×10^{-4}	30-33	3.4×10^{-9}	↓
2×10^{-3}	0.6	1.7×10^{-4}	32-33	6.6×10^{-10}	↓
2×10^{-3}	0.7	9.3×10^{-5}	30-31	3.4×10^{-10}	↓
2×10^{-3}	0.7	9.3×10^{-5}	32-33	5.9×10^{-10}	↓
2×10^{-3}	0.79	4.5×10^{-5}	31-32	5.5×10^{-10}	↓
2×10^{-3}	0.79	4.5×10^{-5}	34-36	5.4×10^{-10}	↓
2×10^{-3}	0.8	4.1×10^{-5}	29-32	7.4×10^{-10}	↓
2×10^{-3}	0.8	4.1×10^{-5}	30-31	4.4×10^{-10}	↓
1×10^{-1}	0.94	1.8×10^{-4}	30-31	3.1×10^{-10}	↓
1×10^{-1}	0.94	1.8×10^{-4}	31-32	1.9×10^{-10}	↓
2×10^{-3}	0.95	2.53×10^{-6}	35-36	1.7×10^{-10}	↓
2×10^{-3}	0.95	2.53×10^{-6}	36-37	1.5×10^{-10}	↓
2×10^{-3}	0.95	2.53×10^{-6}	38-39	2.0×10^{-10}	↓
		Specimen 304-C-17, EPR = 1.8 C/cm^2			
0	1	2.7×10^{-4}	32-33	2.2×10^{-10}	IG
2×10^{-3}	0.5	1.7×10^{-4}	30-32	2.8×10^{-9}	TG
2×10^{-3}	0.6	1.7×10^{-4}	28-29	5.6×10^{-10}	↓
1×10^{-1}	0.94	1.8×10^{-4}	30	2.1×10^{-10}	↓

[a] $\dot{\epsilon}_T = -1/T \ln[1 - (1 - R)^2/2]$.

[b] IG = intergranular, TG = transgranular.

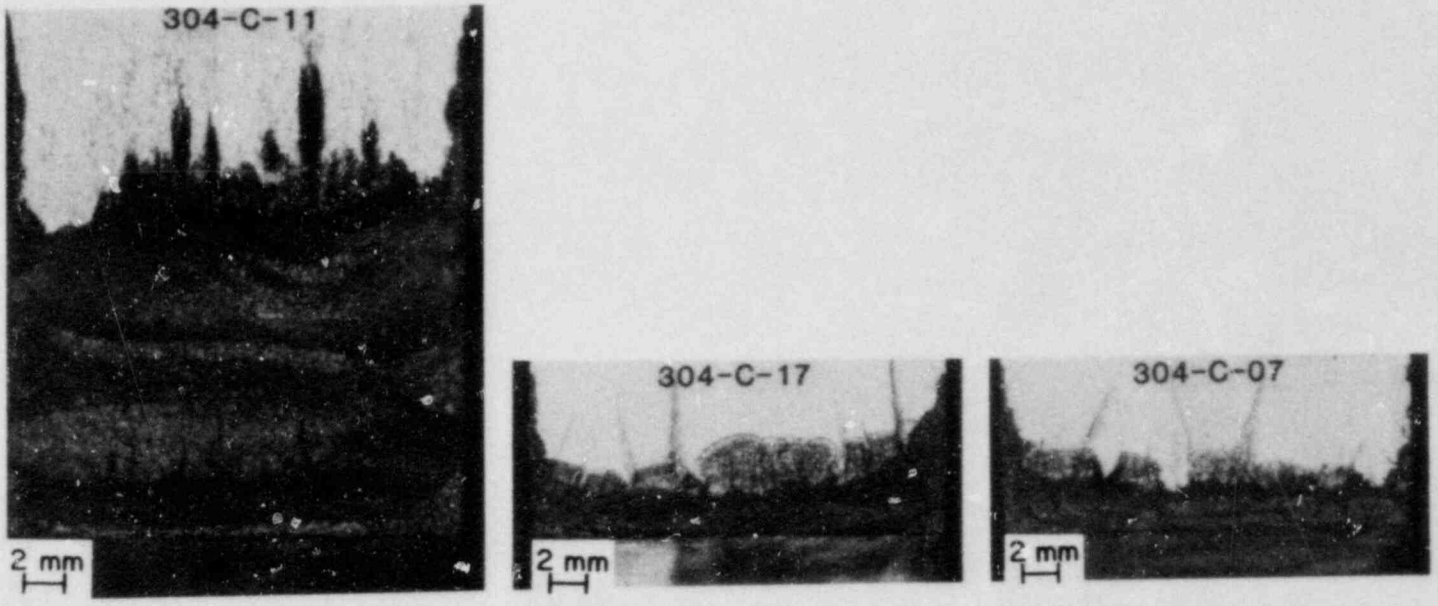

Fig. 1.2. Crack Surfaces of the Specimens 304-C-07, -11, and -17. Large variations in crack length across the thickness of the specimens are observed.

compliance method. The results from both methods are in good agreement as shown for specimen C-11 in Table 1.2. The crack surface was covered with deposits of iron-rich corrosion products. There was no observable correlation between the composition of the corrosion products (as determined by EDX analysis) and position on the crack surface. The corrosion products were removed by use of Dowcon NS-1 solution to permit the determination of the mode of fracture (i.e., intergranular and transgranular) by scanning electron microscopy. The crack growth during the constant-load portion of the tests was intergranular; transgranular cracking was observed during the cyclic-loading portions of the tests (Fig. 1.3).

Direct measurements of the degree of sensitization were made on the specimens (304-C-09, -11, -17) using ASTM A262-A and EPR tests. Significantly lower degrees of sensitization were obtained than those measured on the companion coupon specimens and previously reported (4-15 C/cm^2). The ASTM A262-A gave dual structures for C-09, -17 and a step structure for C-11. The EPR values were 1.6 C/cm^2 (C-09), 1.4 C/cm^2 (C-11), and 1.8 C/cm^2 (C-17). It appears that the nucleation heat treatment (700°C/10 min) was less effective for the 1TCT specimens than for the small-sized coupon specimens. It is, however, interesting that intergranular cracking was observed for these low EPR values under constant-load.

TABLE 1.2. Crack Lengths in 1TCT Specimens Determined by Different Methods

Specimen	Crack Length (mm)		
	Areal Average	Compliance	Side Face
304-C-07	4.45	-	9.01
C-11	18.90	17.59	24.62
C-17	5.20	-	8.99

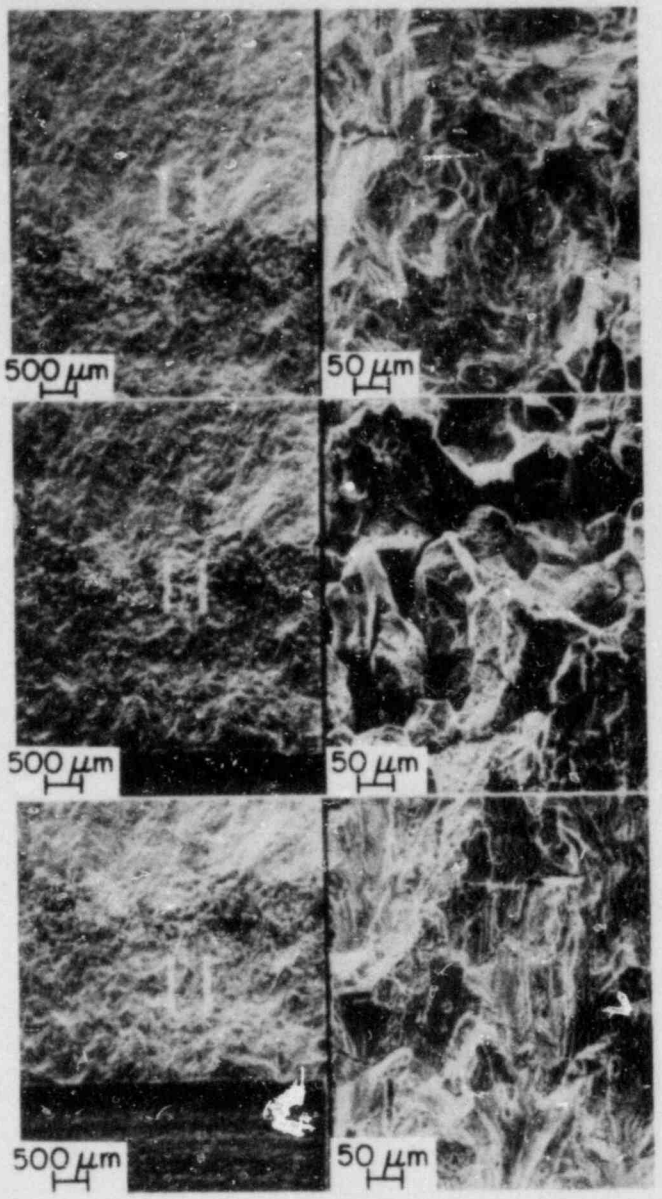

Fig. 1.3. Crack Surfaces of Specimen 304-C-17 Showing Intergranular and Transgranular Modes of Crack Growth.

Fatigue crack growth rate tests are being performed on Type 304 SS (Heat No. 30956) 1TCT specimen in a high purity water at 289°C to calibrate a new a.c. potential system for crack length measurements. The overall sensitivity of the system is estimated to be 0.1 V/mm of crack extension. The preliminary data show that the long-term stability of the system is better than ±5 mV or ±0.05 mm at 289°C.

C. Evaluation of Non-environmental Corrective Actions (P. S. Maiya and W. J. Shack

1. Introduction

The fundamental premise of current efforts to prevent IGSCC in BWR piping is that IGSCC involves a complex interaction among material susceptibility (sensitization), the stresses acting on the material, and the environment and that suitable alteration or variation of these parameters can produce immunity to IGSCC. Nonenvironmental corrective actions seek to mitigate either the material susceptibility or the state of stress on the inside surface of the weldment. They include techniques for improving the margin against IGSCC of a susceptible material like Type 304 SS and the identification of alternative materials that are inherently more resistant to IGSCC.

The objective of the current work is an independent assessment of the proposed remedies developed by the utilities and the vendors. Additional research has been carried out to eliminate gaps in the existing data base on alternative materials and fabrication and to develop a better understanding of the relation between the existing laboratory results and satisfactory in-reactor operating performance. Current efforts in this task include additional screening tests for alternative materials and studies of the residual stress distributions associated with weld overlays.

2. Technical Progress

a. Impurity and Strain Rate Effects

Additional CERT test results on Type 316NG SS (Heat No. P91576) have been obtained in simulated BWR environments over a range of strain rates from 10^{-7} to 10^{-5} s^{-1} and compared with those obtained from Type 316 SS (Heat No. 0590019) under similar heat treatment, environmental and mechanical loading conditions. The results are discussed in terms of the phenomenological model presented in previous reports.[3-5]

The specimens are solution annealed at 1050°C/0.5 h followed by aging at 650°C/24 h. This heat treatment produces no measurable sensitization in Type 316NG SS, but Type 316 SS sensitizes as assessed by the EPR method (EPR $\simeq$ 17 C/cm^2). Heat treated specimens of both Types 316NG and 316 SS were examined by transmission electron microscopy. As can be seen from Fig. 1.4, a typical grain boundary in Type 316 SS shows the presence of Cr-rich carbide precipitates, but there is no evidence of grain boundary precipitation in the NG material. These observations are consistent with the EPR measurements.

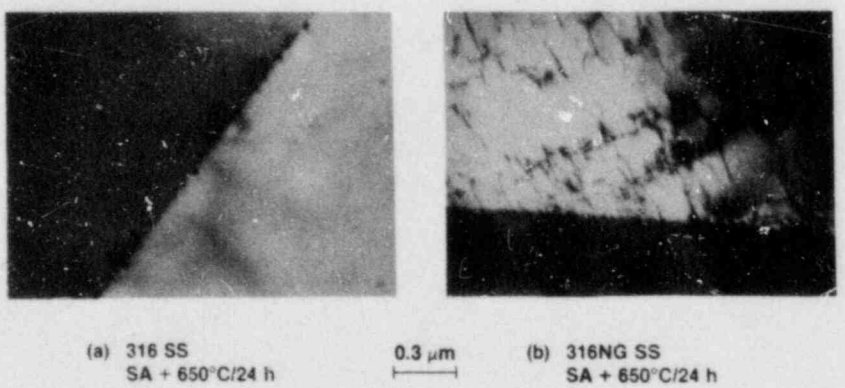

Fig. 1.4. Transmission Electron Micrographs of the Heat Treated Types 316 and 316NG SS.

The CERT test results are summarized in Tables 1.3 and 1.4. Examination of the data shows that TGSCC occurs in Type 316NG SS at $\dot{\varepsilon} \lesssim 1 \times 10^{-6}$ s^{-1}, whereas IGSCC occurs in Type 316 SS at $\dot{\varepsilon} \lesssim 2 \times 10^{-6}$ s^{-1}. Thus the critical strain rates at which cracking occurs are similar for the two materials, although it is somewhat lower for the NG material. Consistent with previously reported results,[6] the transgranular crack growth appears to be unaffected by dissolved oxygen content in the range between 0.2 and 8 ppm. The transgranular crack growth rates in the Type 316NG SS are about a factor of 3 lower than the intergranular crack growth rates in the Type 316 SS. An order of magnitude difference was observed[6] in a more aggressive environment (8 ppm O_2 + 0.5 ppm Cl^-).

The phenomenological model discussed in Refs. 3-5 predicts that crack length at failure (a_f) and time-to-failure (t_f) in CERT tests conducted at different strain rates are related by

$$a_f = A\, t_f^{\frac{1}{2}}, \tag{1.1}$$

where A is a constant. The model also assumes that failure of the specimen occurs when the J-integral approaches the value J_c, which can be related to ε_f and a_f as follows:

$$J_c = C\, \varepsilon_f^{n+1}\, a_f \tag{1.2}$$

$$\simeq C\, \varepsilon_f\, a_f \qquad \text{(assuming } n << 1 \text{ near fracture)}$$

where J_c depends on the material and geometry but is assumed to be independent of $\dot{\varepsilon}$, C is a material parameter, ε_f is the strain at failure ($\simeq \dot{\varepsilon} t_f$), and n is the strain hardening exponent. Figures 1.5 and 1.6 show that the CERT test results in Tables 1.3 and 1.4 are consistent with Eqs. (1.1) and (1.2). Since the fracture characterization parameter J_c is expected to be only weakly dependent on the environment, the results obtained in the more aggressive chloride environment are also included in Fig. 1.6.

TABLE 1.3. CERT Test Results for Type 316NG SS (Heat No. P91756, 1050°C/0.5 h + 650°C/24 h) in Oxygenated Water (0.2 ppm O_2) with 0.1 ppm Sulfate. T = 289°C, ε_o = 1.0% and a_o = 1 μ

Test Number	$\dot{\varepsilon}$, s^{-1}	t_f, h	ε_f, %	$\Delta A/A_o$,	σ_{max}, MPa	Failure Mode	$\dot{a}_{av}$, m/s
157	1×10^{-5}	9.7	34.9	68	430	Ductile	
159	2×10^{-6}	53.5	38.5	67	453	Ductile	
160	1×10^{-6}	100.6	35.9	65	450	TGSCC	1.51×10^{-9}
154[a]	1×10^{-6}	109.4	39.0	56	458	TGSCC	1.50×10^{-9}
169	4×10^{-7}	217.4	31.3	59	462	TGSCC	9.74×10^{-10}
172	2×10^{-7}	474.0	34.1	44	461	TGSCC	7.35×10^{-10}
148	9.5×10^{-8}	565.9	20.3	61	472	TGSCC	6.73×10^{-10}

[a] 8 ppm O_2 + 0.1 ppm sulfate.

TABLE 1.4. CERT Test Results for Type 316 SS (Heat No. 0590019, 1050°C/0.5 h + 650°C/24 h, EPR ~ 17 C/cm²) in Oxygenated Water (0.2 ppm O_2) with 0.1 ppm Sulfate. T = 289°C, ε_o = 1.0% and a_o = 1 μm.

Test Number	$\dot{\varepsilon}$, s^{-1}	t_f, h	ε_f, %	$\Delta A/A_o$,	σ_{max}, MPa	Failure Mode	$\dot{a}_{av}$, m/s
156	1×10^{-5}	10.3	37.1	64	468	Ductile	-
61	2×10^{-6}	49.6	35.7	52	477	IGSCC	5.70×10^{-9}
68	2×10^{-6}	49.8	35.8	41	475		5.42×10^{-9}
176	1×10^{-6}	79.2	28.5	37	463		4.01×10^{-9}
162	4×10^{-7}	173.7	25.0	33	417		3.65×10^{-9}
109	2×10^{-7}	264.2	19.0	18	441		2.25×10^{-9}
194	2×10^{-7}	261.0	19.0	24	396		2.49×10^{-9}

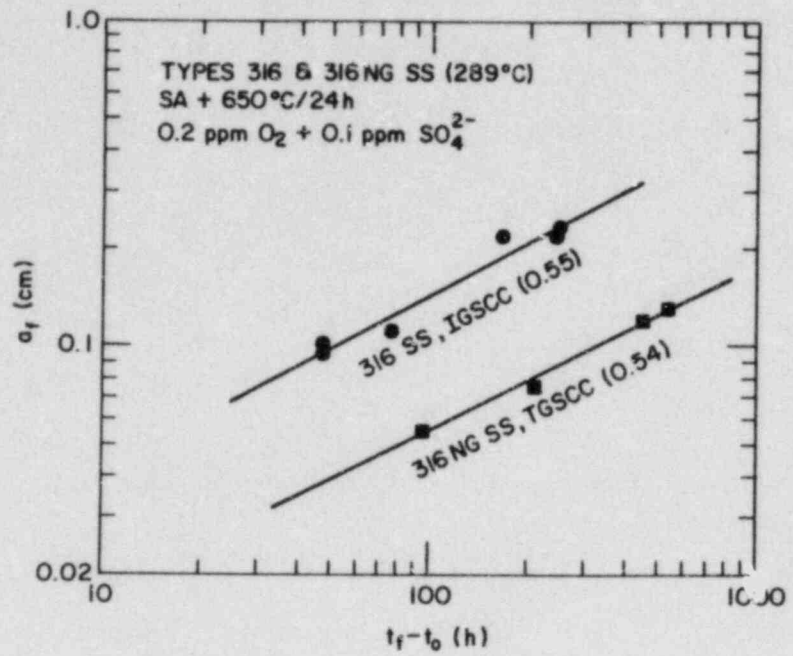

Fig. 1.5. Correlation between Crack Length at Failure (ε_f) and Function of Time-to-Failure (Corrected for Crack Initiation Time) in Tests Conducted at Different Strain Rates.

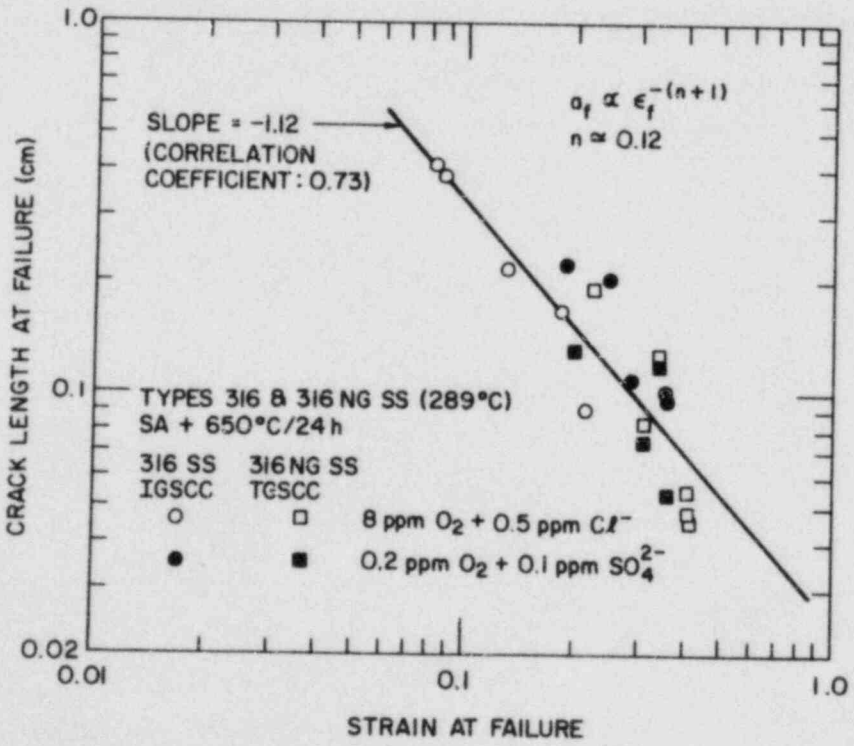

Fig. 1.6. Correlation between Crack Length at Failure (a_f) and Strain at Failure (ε_f).

Figure 1.6 suggests that $n \simeq 0$ is a reasonable approximation. The predictions of the model can also be expressed in terms of correlations between $\dot{\epsilon}$ and SCC susceptibility parameters such as t_f and $\dot{a}_{av}$,

$$t_f = \left(\frac{J_c}{AC}\right)^{2/3} \dot{\epsilon}^{-2/3} \tag{1.3}$$

and

$$\dot{a}_{av} = A \left(\frac{AC}{J_c}\right)^{1/3} \dot{\epsilon}^{1/3} . \tag{1.4}$$

The agreement between the experimental data and the correlations derived from the model is shown in Figs. 1.7 and 1.8. These results suggest that the model may provide a useful way to extrapolate to very slow strain rates ($\lesssim 10^{-8}$ s^{-1}) assuming that the cracking susceptibility continues to increase with a decrease in strain rate. Figures 1.6 and 1.7 also suggest that $\dot{a}_{av}$ is a more sensitive measure of SCC susceptibility than t_f.

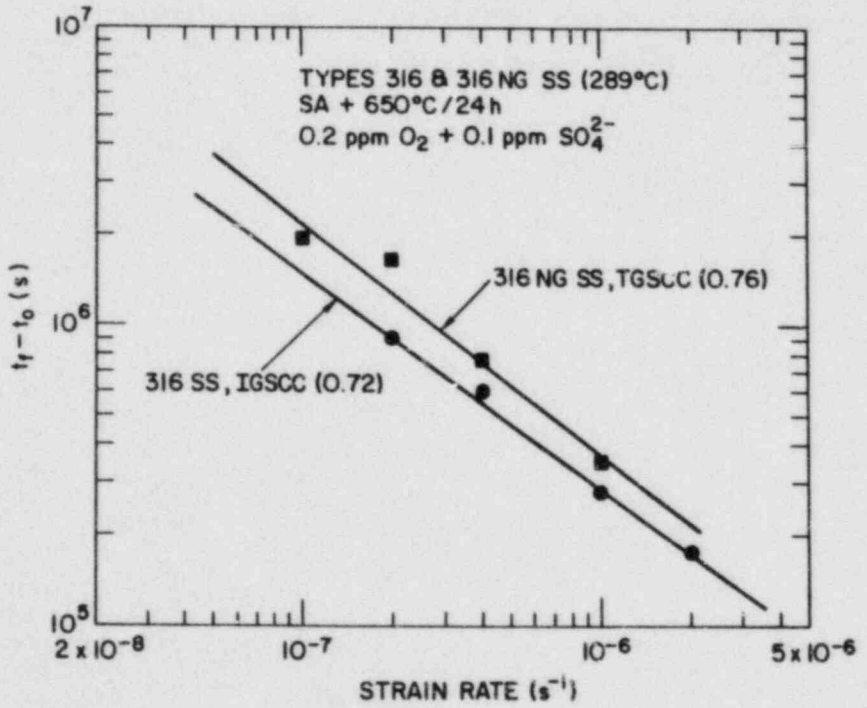

Fig. 1.7. Correlation between Time-to-Failure and Strain Rate for Failure by IGSCC and TGSCC.

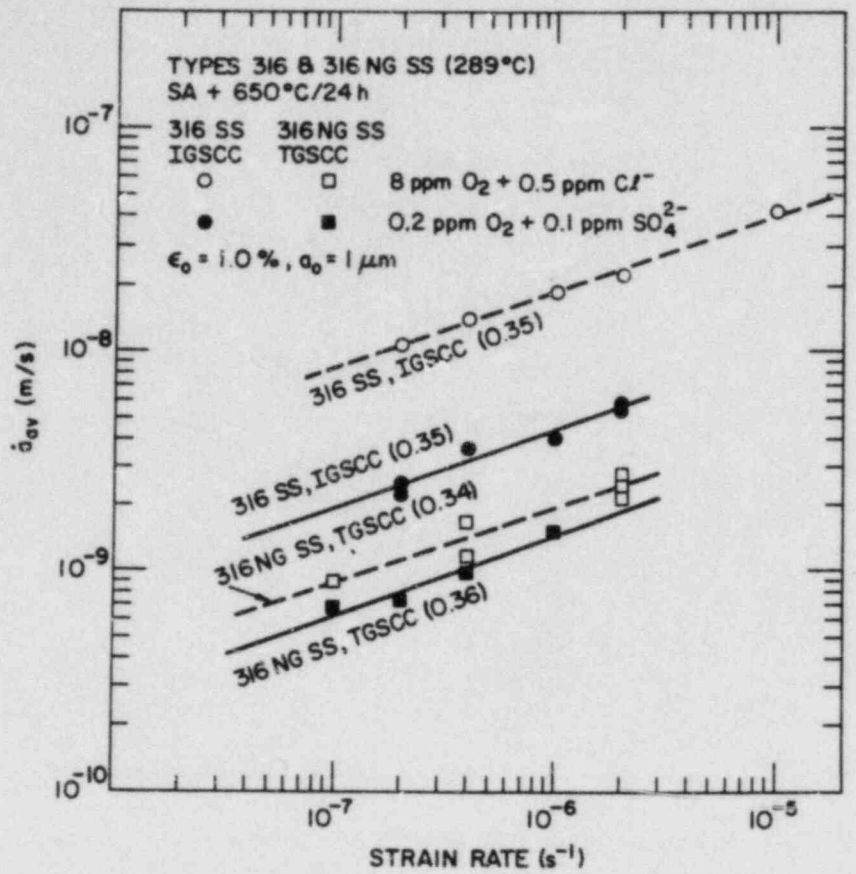

Fig. 1.8. Correlation between Average Stress Corrosion Crack Growth Rate and Strain Rate.

Figure 1.9 shows that the dependence on strain rate predicted by the model appears to be valid for both IGSCC and TGSCC in a number of different environments. In going from an aggressive chloride environment to an environment with impurity levels within the current allowable BWR water-chemistry limits, the average IG crack growth rate decreases by a factor of ~4, but the average TG crack growth rate decreases by a factor of less than two. Hence, the relative crack growth rate for the conventional and the NG materials is dependent on the testing environment.

CERT test results on Type 316NG SS in high-purity water (0.2 ppm O_2) over the same range of strain rates ($\dot{\varepsilon} \simeq 10^{-6}$-$10^{-7}$ s^{-1}) as encompassed in the impurity environment are summarized in Table 1.5. No evidence of SCC was observed in these tests. As Table 1.3 shows, under similar loading conditions TGSCC occurs in the presence of 0.1 ppm sulfate.

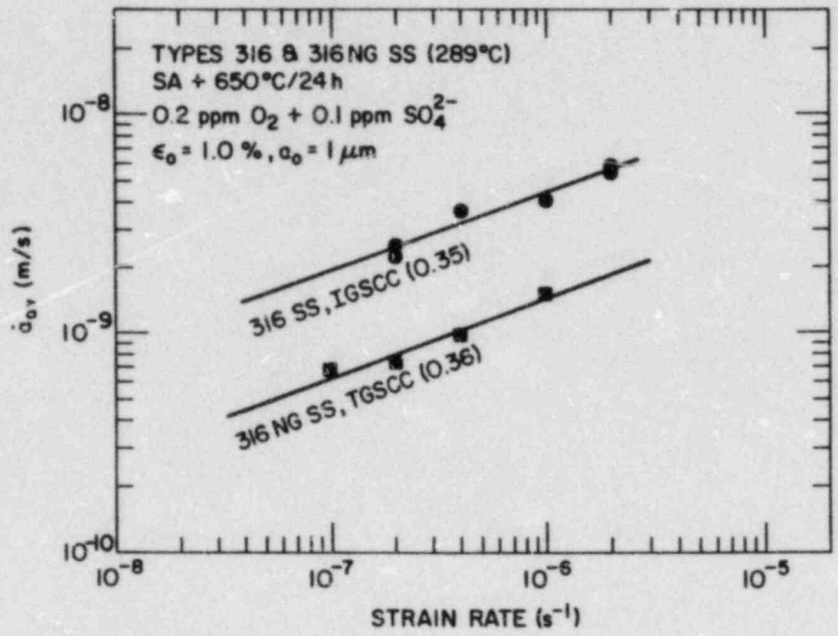

Fig. 1.9. Effects of Different Environments and Strain Rate on the Relative Average Crack Growth Rates of Types 316 and 316NG SS.

TABLE 1.5. SCC Resistance of Type 316NG SS (1050°C/0.5 h + 650°C/24 h) in High Purity Water (0.2 ppm O_2) at 289°C

Specimen No.	a (s^{-1})	t_f (n)	ϵ_f (%)	$\epsilon_{uniform}$ (%)	σ_{max} (MPa)	Failure Mode
PM9-35	1×10^{-6}	100.3	36.1	30.9	457	Ductile
PM9-43	2×10^{-6}	47.9	34.5	29.1	448	Ductile
PM9-39	4×10^{-7}	246.3	35.5	30.5	456	Ductile
PM9-27	1×10^{-7}	917.0	33.0	28.4	485	Ductile

[a]At these strain rates, presence of 0.1 ppm sulfate (added as acid) causes TGSCC to occur in the material.

These results confirm that impurities play a crucial role in the cracking process. Currently, experiments are being performed in water containing 0.2 ppm O_2 and sulfate impurity levels between 0.01 and 0.05 ppm to determine the concentration of sulfate necessary to produce TGSCC in the NG material.

b. Stress/Strain/Strain-rate Relations for Sensitized Materials

Stress-relaxation experiments have been performed on Types 304 and 316 SS at 28°C for different degrees of sensitization. The data were used to determine stress/strain/strain-rate relations, which are required to relate the laboratory results obtained under different loading histories (CERT, pipe, constant load tests, etc.) to loading histories encountered under reactor operating conditions. Currently, experiments are being planned to obtain similar information at 289°C. However, the analysis of data obtained at 28°C is also applicable to data at temperatures between 20 and 300°C, since the relationship between σ, the applied stress, and $\dot{\epsilon}$, the (non-elastic) strain rate, is invariant over this temperature range for stainless steels. In a previous report,[6] typical results for sensitized Type 316 SS were analyzed using the constitutive equations developed by Hart.[7] Glide friction-controlled flow governs the constitutive behavior and in Hart's model[7] is given by

$$\dot{\epsilon} = \dot{a}^* \left(\frac{\sigma - \sigma^*}{G} \right)^M \tag{1.5}$$

or

$$\sigma = \sigma^* + \left(\frac{G^M}{\dot{a}^*} \right)^{1/M} (\dot{\epsilon})^{1/M} . \tag{1.6}$$

In Eq. (1.5), $\dot{a}^*$ is the glide friction rate parameter, σ is the applied stress, σ^* is the hardness, G is the shear modulus, and M is a constant. Equation (1.5) describes the data remarkably well for non-elastic strains of $\geq$1.0% in sensitized material (solution-annealed at 1050°C/0.5 h and aged at 650°C/50 h), since for large strains the change in strain during a relaxation run is small, and the material microstructural state remains

constant (assuming that no other structural changes such as strain aging occurs). This is not the case for small strains (<1.0%) as has been discussed previously.[6]

Further tests have shown that Eq. (1.5) also provides a good description of the data for $\varepsilon \geq 1.0\%$ for material in three different heat-treatment conditions: as-received, solution-annealed at 1050°C/0.5 h, and solution-annealed followed by sensitization at 650°C/50 h. However, for the sensitized material, the description of the data over the range of strain rates from 10^{-4} to 10^{-9} s^{-1} by this approach is less accurate than for the other material conditions.[6] This suggests that modification of the constitutive approach to take into account structural changes during relaxation is required. In these tests the initial stresses prior to relaxation varied between 255 and 385 MPa and the corresponding strains varied from 0.2 to 8.5% depending on the material condition.

The value of M [in Eq. (1.5)] is approximately constant for $\varepsilon > 1.0\%$. The average values of M are 0.0865, 0.071 and 0.073 for the steel in the as-received, solution-annealed, and sensitized conditions, respectively.

For material in the as received and sensitized conditions, an initial stress of 255 MPa produced non-elastic strains of ∿0.2 and 0.58%, respectively, and for these cases, the values of M are 0.017 and 0.027, respectively, which are significantly smaller than the values determined at higher strains.

The values of $\dot{a}^*$ and σ^* that were obtained by analysis of the data for $\varepsilon > 1.0\%$ are given in Tables 1.6-1.8. The value of $\dot{a}^*$ decreases with an increase in hardness, and the values of $\dot{a}^*$ are vastly different for the as-received and the heat-treated materials.

TABLE 1.6. Stress Relaxation Parameters for Type 316 SS (As-Received)
σ = 256 MPa, T = 30°C, n = 0.0865

σ_i	ϵ_n, %	σ^*, MPa	a^*, s^{-1}
1.2 σ	0.93-1.02	250	2.14×10^{32}
1.3 σ	2.08-2.17	279	2.08×10^{32}
1.4 σ	3.51-3.59	308	1.38×10^{32}
1.5 σ	5.05-5.14	337	9.59×10^{31}

$G = 7.53 \times 10^4$ MPa

TABLE 1.7. Stress Relaxation Parameters for Type 316 SS (Solution-Annealed at 1050°C/0.5 h), σ = 256 MPa, T = 30°C, M = 0.073

σ_i	ϵ_n, %	σ^*, MPa	a^*, s^{-1}
1.0 σ	1.26-1.34	199	8.14×10^{38}
1.1 σ	2.27-2.36	224	4.53×10^{38}
1.2 σ	3.60-3.68	252	2.14×10^{38}
1.3 σ	5.09-5.17	281	1.20×10^{38}
1.4 σ	6.71-6.80	310	5.97×10^{37}
1.5 σ	8.47-8.56	338	1.32×10^{37}

$G = 7.53 \times 10^4$ MPa

TABLE 1.8. Stress Relaxation Parameters for Type 316 SS (Solution-Annealed at 1050°C/0.5 h and Aged at 650°C/50 h), σ = 256 MPa, T = 30°C, M = 0.071

σ_i	ε_n, %	σ*, MPa	a*, s^{-1}
1.1 σ	1.77-1.84	224	6.57×10^{39}
1.2 σ	2.91-2.99	249	1.83×10^{39}
1.3 σ	3.79-3.86	279	1.91×10^{39}
1.4 σ	8.80-5.88	305	5.04×10^{38}
1.5 σ	7.38-7.46	334	1.80×10^{38}

$G = 7.53 \times 10^4$ MPa

For the solution-annealed and sensitized materials, σ* and ε are related by a power law (see Fig. 1.10). However, å* does not appear to be related to strain in a simple manner. Hence, the constitutive equation for the sensitized material involves at least two variables (σ* and å* or å* and ε_n). This is also expected to be the case for the higher temperature (289°C) encountered in BWRs.

c. Residual Stress Measurements

Measurements of throughwall residual stresses have been made on the standard overlay mock-up supplied by Georgia Power and NUTECH. The weldment was fabricated from 12-in. Schedule 100 pipe with overlay welding procedures identical to those used in the repairs on the Hatch reactors. Four azimuths 90° apart were instrumented with strain gages. Miniature 60° strain-gage rosettes (Micro-Measurements EA-09-030YB-120) with an active length of 0.76 mm (30 mils) were used. After the complete weldment was instrumented, full thickness bars 63 mm wide and 340 mm long were cut from the weldment at the four azimuthal positions where the strain gages were mounted. The stress changes produced by the removal of the bars indicated that the stress distributions were reasonably axisymmetric (as was the case

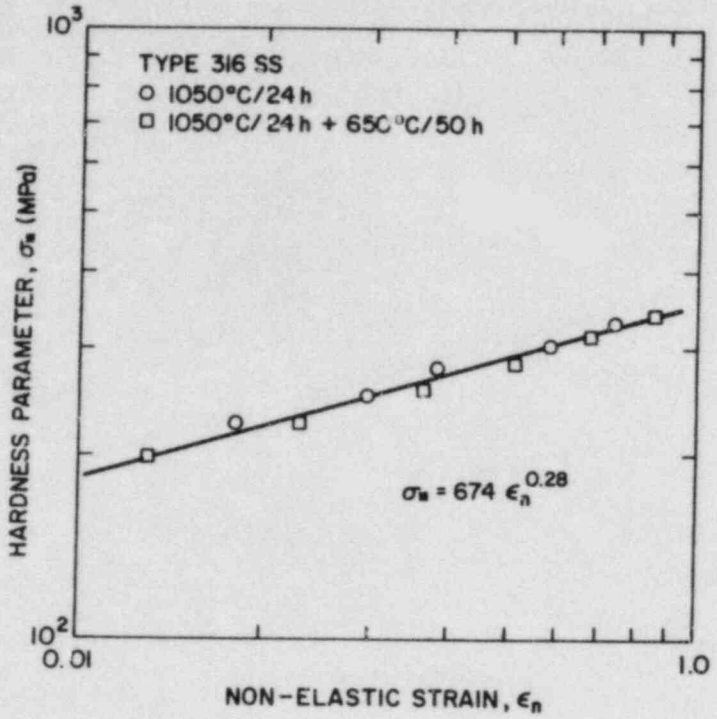

Fig. 1.10. Correlation between Hardness Parameter and Strain for Heat-Treated Type 316 SS.

also for the minioverlays). Hence, inner surface and throughwall stresses were measured at only one azimuth. Measurements were made at seven axial locations on the side with the long weld prep geometry typical of that used in Hatch 1 and at six axial locations on the side with the short weld prep geometry characteristic of that used in Hatch 2. The axial locations are indicated on Fig. 1.11.

The stress changes measured on the inner and outer surfaces during the parting out of the full thickness bars can be used to calculate the net forces and moments acting on the bars before they were cut from the complete weldment. However, they are not accurate measures of the actual streases on the inner and outer surfaces, since substantial self-equilibrating stresses remain in the full-thickness specimens. To determine the actual stresses on the inner surface, a thin slab (3 mm thick) was removed from the inner surface of each specimen using electrical discharge machining. This provides almost complete stress relief for the gages on the inner surface.

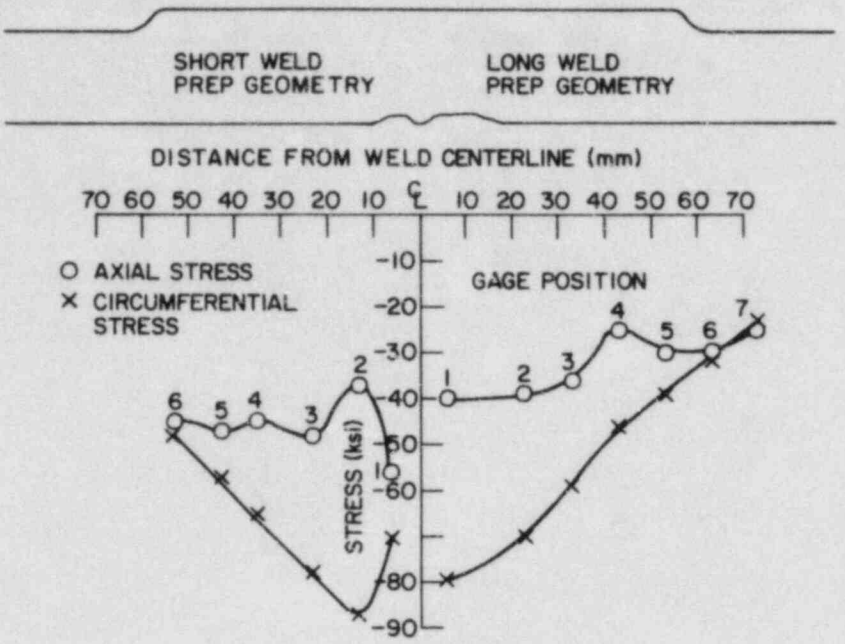

Fig. 1.11. Inside Surface Axial and Circumferential Residual Stresses and Axial Locations of Strain Gage Rosettes on the Hatch Standard Overlay Mockup.

To determine the throughwall distribution of stresses in the weldment, thin layers of material were removed from the inner surface by milling. The resultant strain relief measured by the gages mounted on the outer surface of the weldment was used to compute the throughwall stress distribution. A detailed discussion of the experimental procedures and analysis used is given in Ref. 8.

As Fig. 1.11 shows, the overlay was very successful in inducing compressive residual stresses on the inner surface of the weldment for both weld prep geometries. The measured results are in general agreement with the finite element predictions supplied by NUTECH. However, the measured residual stresses on the inner surface are significantly more compressive than those predicted by the calculations. The finite element calculations also show some very rapid oscillations near the weld fusion line. The parting out stresses at the four azimuths do show more scatter near the fusion line, which is consistent with this prediction, but it is difficult to resolve stress gradients on this scale. Finite element

calculations on an uncracked weldment have also been performed recently by E. F. Rybicki, Inc. under subcontract to ANL. Although the finite element model used in this work does not exactly duplicate the mock-up (no attempt was made to model the weld prep geometries and the welding parameters used are not exactly the same as those used in preparing the mock-up), the predicted stresses on the inner surface are closer to the experimentally measured values. The reasons for the differences between the two finite element calculations are not immediately apparent.

Throughwall axial residual stresses for the locations under the overlay are shown in Figs. 1.12-1.15. The solid curves are fourth order polynomials that were fit to the data by use of a least-squares procedure. The depth shown in the figures is nondimensionalized with respect to the total thickness, i.e., wall plus overlay. As expected, the stresses are strongly compressive on the inner portion of the wall and tensile on the outer portion. These distributions should not be interpreted to indicate that the overlay will be effective for cracks roughly halfway through the wall and ineffective for deeper cracks, since finite element results[9] show that the presence of a crack strongly perturbs the stresses produced by the overlay process. Although these results do confirm the analytical predictions of strongly compressive stress fields produced on the inner surface by the overlay, other types of tests are needed to verify the predicted stress fields at crack tips.

The residual stresses measured for the standard overlay are similar to those obtained for the minioverlay.[6] On the side of the weldment with the long weld prep, the stresses are generally less compressive for the standard overlay than for the minioverlay. On the side of the weldment with the short weld prep, the situation is reversed. However, the differences are small and are within the variations that might be expected from weld to weld with a single procedure.

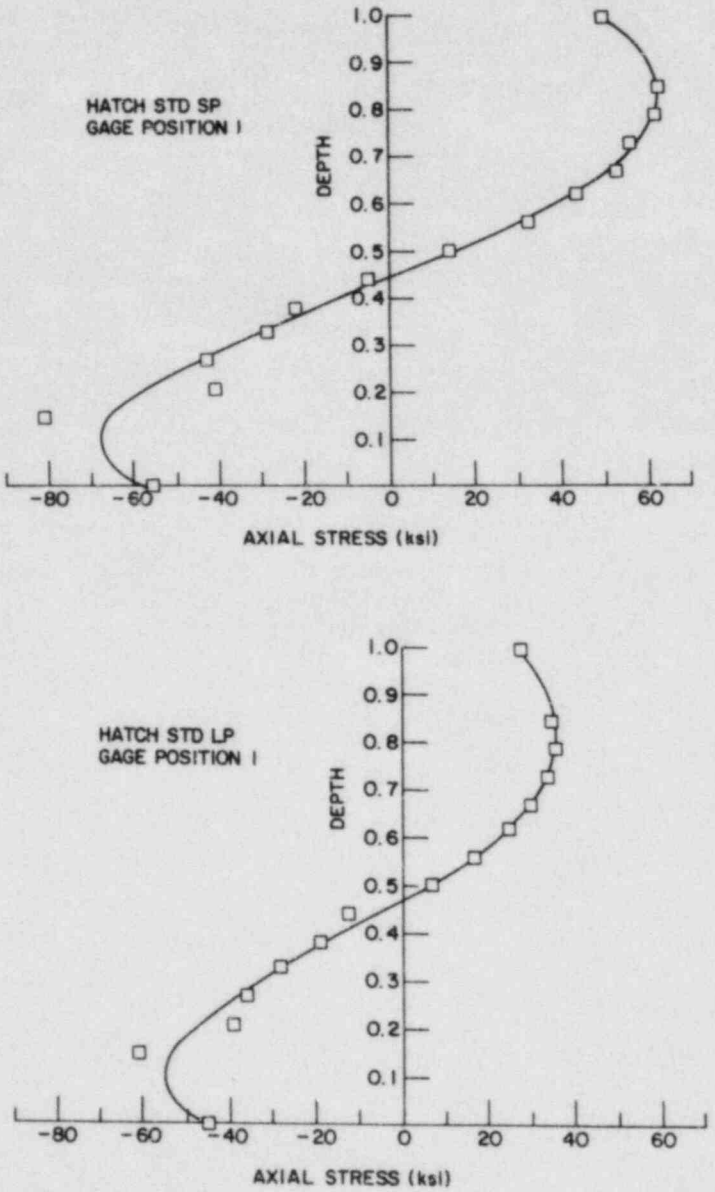

Fig. 1.12. (a) Throughwall Axial Residual Stresses at Gage Position 1 on the Short Weld Prep Side of the Hatch Standard Overlay Mockup Weldment; (b) Throughwall Axial Residual Stresses at Gage Position 1 on the Long Weld Prep Side of the Hatch Standard Overlay Mockup Weldment.

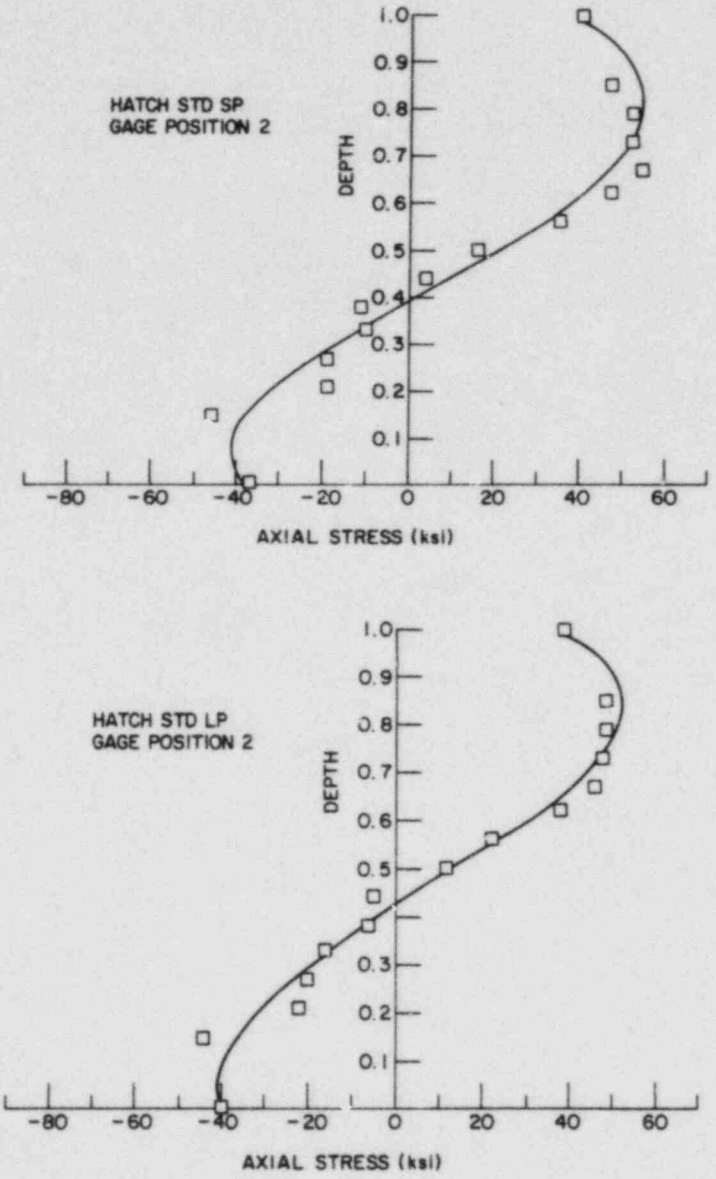

Fig. 1.13. (a) Throughwall Axial Residual Stresses at Gage Position 2 on the Short Weld Prep Side of the Hatch Standard Overlay Mockup Weldment; (b) Throughwall Axial Residual Stresses at Gage Position 2 on the Long Weld Prep Side of the Hatch Standard Overlay Mockup Weldment.

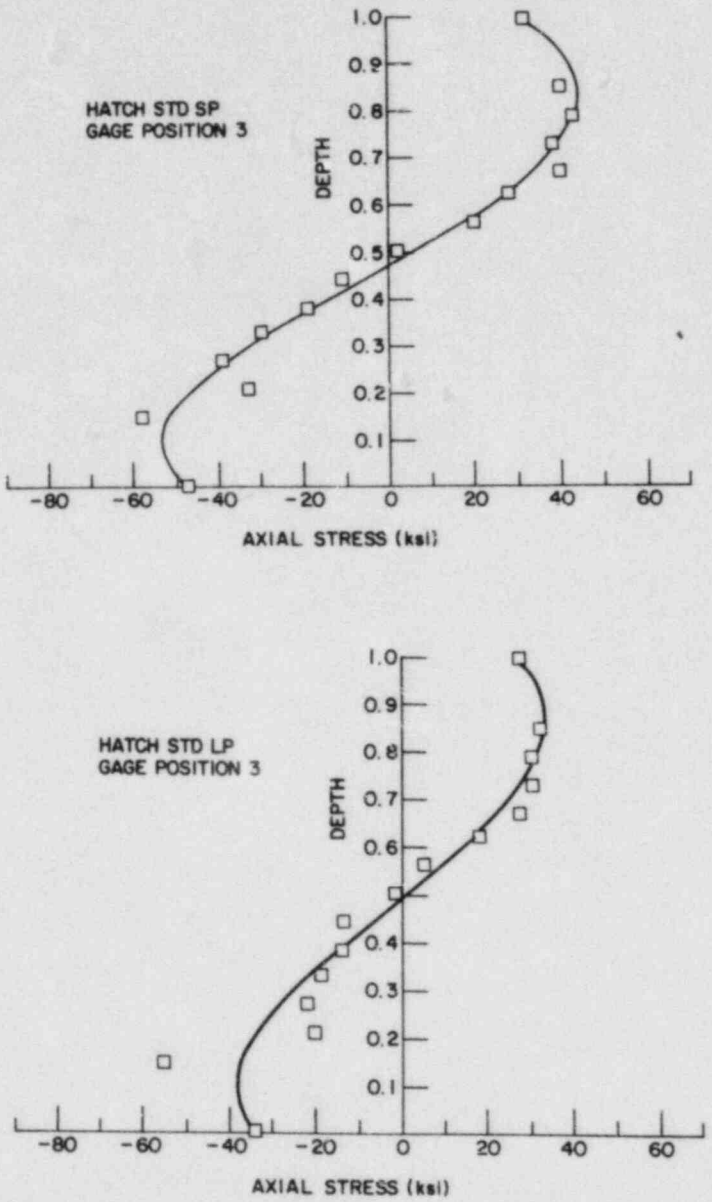

Fig. 1.14. (a) Throughwall Axial Residual Stresses at Gage Position 3 on the Short Weld Prep Side of the Hatch Standard Overlay Mockup Weldment; (b) Throughwall Axial Residual Stresses at Gage Position 3 on the Long Weld Prep Side of the Hatch Standard Overlay Mockup Weldment.

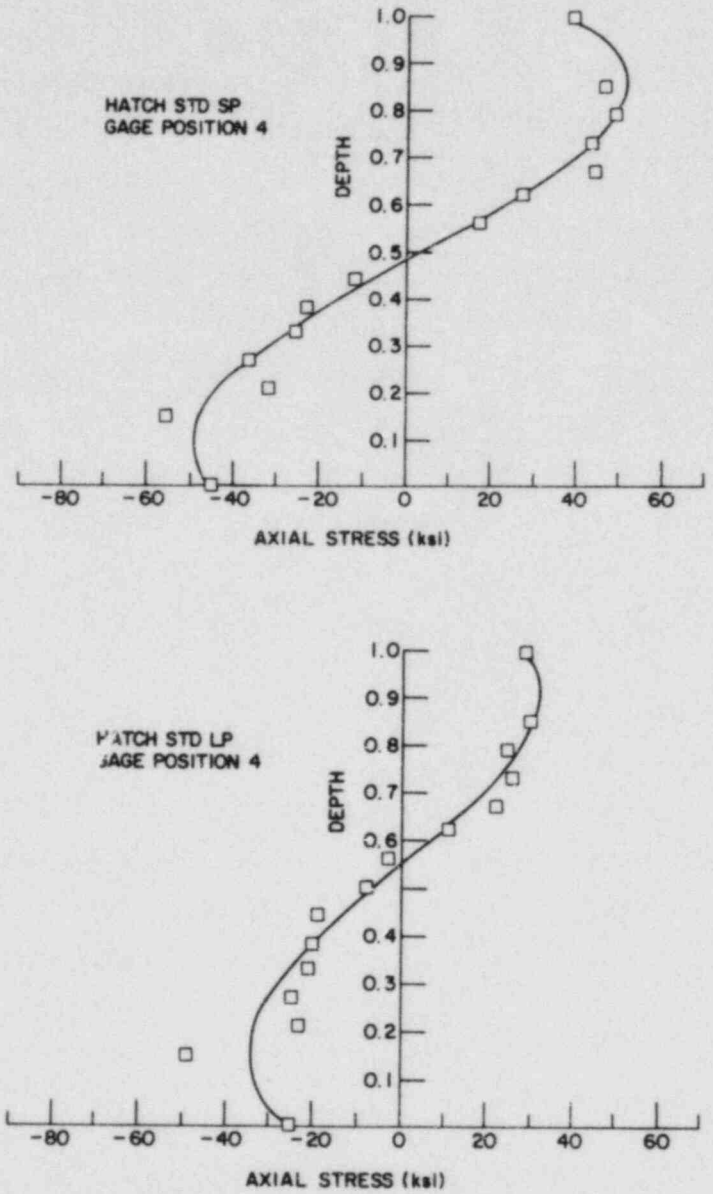

Fig. 1.15. (a) Throughwall Axial Residual Stresses at Gage Position 4 on the Short Weld Prep Side of the Hatch Standard Overlay Mockup Weldment; (b) Throughwall Axial Residual Stresses at Gage Position 4 on the Long Weld Prep Side of the Hatch Standard Overlay Mockup Weldment.

D. Evaluation of Environmental Corrective Actions (W. E. Ruther, W. K. Soppet, and T. F. Kassner)

1. Introduction

The objective of this subtask is to evaluate the potential effectiveness of proposed actions to solve or mitigate the problem of IGSCC in BWR piping and safe ends through modifications of the water chemistry. Although the reactor coolant environment has a profound influence on the performance and reliability of nuclear power-plant components, the synergistic effects of oxygen (produced by radiolytic decomposition of the water) and impurities (e.g., H_2SO_4 from decomposition of ion exchange resins during periodic intrusions into the primary system) on the IGSCC susceptibility and crack growth properties of sensitized Type 304 SS have not been investigated adequately. Also, it is not clear whether the potential benefits associated with small additions of hydrogen to the coolant can be realized in the presence of impurities within the normal operating limits on pH (5.6 to 8.6 at 25°C) and specific conductance ($\leq$1.0 μS/cm at 25°C) of the reactor coolant water.

During this reporting period, information on the effect of different anion impurity species on the SCC susceptibility of sensitized Type 304 SS has been obtained from CERT experiments in 289°C water containing 0.2 ppm dissolved oxygen. The influence of temperature over the range 110 to 320°C on the SCC behavior of the steel was also investigated in high-purity water and in water with 0.1 and 1.0 ppm sulfate as H_2SO_4 at a dissolved oxygen concentration of 0.2 ppm. Experiments to determine the effect of dissolved oxygen and sulfate concentration on crack growth rates in the steel with several levels of sensitization are continuing under low-frequency, moderate-stress intensity, high-R loading at 289°C.

2. Technical Progress

a. Sources of Anion Impurity Species and Their Effect on SCC Susceptibility

In addition to dissolved oxygen (produced by radiolytic decomposition of the water) and corrosion products, other impurity species can

enter the reactor coolant water through a number of sources (e.g., condensate and reactor-water cleanup demineralizers, condensate storage tank, the suppression pool and reactor heat removal system, etc.). The demineralizer systems on BWRs increase plant availability by reducing the time required to meet feedwater chemistry specifications during plant startup and also remove contaminants introduced by condenser in-leakage and unanticipated upsets in water chemistry. However, the demineralizer resins are also a source of contamination due to leakage of ion-exchange resin fragments into the system during normal operation and to the release of ions to the water following regeneration of the resins. In the later case, the regeneration equipment and processes must be optimized to reduce impurity ingress to the system. For example, a major difficulty in achieving low impurity leakage levels after regeneration of mixed beds arises from resin cross contamination during hydraulic separation of the anion and cation resins, and in the case of double vessel regenerations, the subsequent transfer of some of the cation resin with the anion resin to the anion regeneration vessel. Incomplete separation of the resins or improper transfer of the anion resin causes conversion of a portion of the cation resin to the sodium form during regeneration of the anion resin with an NaOH solution. Similarly, some of the anion resin will be converted to the bisulfate form when the cation resin is regenerated with sulfuric acid. Thus, incomplete separation leads to the release of sodium and/or sulfate when the mixed beds are put into operation.[10] Different regeneration processes have been developed to minimize cross contamination of the resins (e.g., Ammonex, patented by the Cochrane Division of the Crane Company; Seprex, developed by Graver Water Division of Ecodyne Corp.; the Triobed process[11] developed by Diaprosim Company in France; and others).

The problem of resin release and transport for condensate polisher systems on the secondary side of several pressurized water reactors (PWRs)[12] has been evaluated in relation to corrosion-induced tube and tube support plate degradation in steam generators. The results of this study[12] indicate that both the powdered-resin and deep-bed-type systems release resin fragments in the effluent streams during vessel cut-in, and steady-state and flow-transient operation. In general, powdered-resin condensate polisher systems exhibited higher resin leakage than deep-bed systems during vessel cut-ins, although the extent of resin leakage was similar during normal

operation. Resin leakage increases during flow transients over short-time periods (10-20 min) and then decreases to the original levels; however, the majority of the resin loss from each type of polisher system occurs during steady-state operation rather than during vessel cut-in. It was also determined that significantly higher resin leakage occurred during cut-in of deep-bed polisher vessels with new resin beds that were not backwashed prior to use, than for beds which were backwashed and regenerated. Estimates of total resin losses into the secondary system of several PWR plants that use 100% condensate polishing range between ~20 and 180 kg per year.[12]

The extent of impurity ingress to the recirculation loop water of BWRs during normal operation has not been evaluated in detail. However, the frequency and magnitude of water chemistry transients in 20 domestic BWRs from the startup dates to mid-1979[13] has been investigated. This study revealed that along with unavailability of the reactor water cleanup system, resin ingress and condenser tube leakage are the major causes of off-standard water chemistry. Five of the six plants with deep-bed demineralizers replaced the exhausted resin in lieu of regeneration. The other 14 plants use precoat systems with powdered resins. The condensate treatment systems were of the same type with the exception of several plants with sea-water-cooled condensers that used deep-bed or deep-bed plus precoat systems. The resins in the condensate treatment systems are regenerated in 18 of the 20 plants.

The portion of the feedwater flow that actually passes through the demineralizer on the reactor water cleanup system is considerably greater for the deep-bed type (5 to 13%, where the actual vessel flow rates are ~200 to 600 gal/min) compared to the precoat systems (~1% flow or ~65 to 100 gal/min). This difference coupled with the condition of the resin can influence water quality during normal operation as well as under transient events, e.g., cooling water in-leakage through condenser tube leaks or removal of resin degradation products.

The combined effect of high temperature and the neutron flux in the reactor core causes rapid decomposition of resin fragments that enter the recirculation water loop of a BWR.[14,15] More recent laboratory studies of the thermal stability of Dowex 1 x 8 anion and Dowex 50 x 8 cation resins at 288°C

also reveal rapid degradation of the resin into organic fragments and functional groups accompanied by the release of retained ions.[16,17] Scission of the sulfonic acid group from the polystyrene divinyl benzene structure yielded a high concentration of sulfuric acid after reaction with water and relatively small amounts of nitrite, nitrate, and chloride presumably from impurities in the cation resin. The thermal degradation of the anion resin produced carbon from scission ion-active quaternary amine group, and trimethylamine and ammonia from decomposition of the amine group as well as some chloride and sulfate retained by the resin. These studies[14-17] indicate that a number of anion species can be released to the high-temperature coolant from resin ingress and decomposition (viz., SO_4^{2-}, HH_3-NH_4^+, NO_2^-, NO_3^-, as well as those anions present from ion exchange, e.g., Cl^-, CO_3^{2-}, PO_4^{3-}, etc.).

The relative effect of various anion species, in conjunction with hydrogen and sodium cations, on the SCC susceptibility of lightly sensitized (EPR = 2 C/cm^2) Type 304 SS has been evaluated in a series of CERT tests in 289°C water containing 0.2 ppm dissolved oxygen. The anion concentration of the feedwater was set at 0.1 ppm without consideration of the actual concentration of the species that results from dissociation equilibria at high temperature. However, the concentrations of various species at 289°C can be calculated from dissociation constants[18] for equilibria involving many of the anions that are likely to be present in BWR water. The influence of different anions with sodium at total conductivity values of $\lesssim$1 μS/cm and a dissolved oxygen concentration of the water of ~0.2 ppm on the CERT parameters is shown in Table 1.9. The results indicate that a ductile plus transgranular failure mode occurred in high-purity water and in water containing nitrate and borate. Only a small decrease in the time to failure resulted from the addition of these ions. The effect of the carbonate and chloride on IGSCC was virtually identical in terms of the various CERT parameters. Phosphate, silicate, and hydroxide appear slightly more detrimental than carbonate and chloride. The sulfur species (viz., sulfate, sulfite, thiosulfate, and sulfide) produced the highest degree of IGSCC in terms of the amount of intergranular cracking and the largest reduction in the time to failure, maximum stress, etc. The relative effect of the various anions on the time-to-failure is shown in Fig. 1.16. Our results are in reasonable agreement with those[19] obtained on as-welded Type 304 SS specimens (EPR = 0.9 to 3.8 C/cm^2) in 274°C water

TABLE 1.9. Influence of Different Anions at Concentration[a] of 0.1 ppm on the SCC Susceptibility of Sensitized (EPR = 2 C/cm^2) Type 304 SS Specimens[b] (Heat No. 30956) in 289°C Water Containing 0.2 ppm Dissolved Oxygen

	Feedwater Chemistry				CERT Parameters				
Test No.	Oxygen, ppm	Impurity Species	Cond. at 25°C, µS/cm	pH at 25°C	Failure Time, h	Maximum Stress, MPa	Total Elong., %	Reduction in Area, %	Fracture Morphology[c]
A2	0.24	-	0.14	6.12	166	493	60	66	0.80D, 0.20T
A50	0.24	$NaNO_3$	0.34	6.03	152	516	55	60	0.85D, 0.15T
A51	0.26	$Na_2B_4O_7$	0.21	6.40	142	523	51	68	0.88D, 0.12T
A48	0.30	Na_2CO_3	0.43	6.80	103	476	37	43	$0.60D, 0.40G_3$
A49	0.31	NaCl	0.51	6.05	98	476	35	50	$0.58D, 0.42G_2$
A65	0.22	Na_3PO_4	0.47	6.93	84	448	30	30	$0.57D, 0.43G_3$
A66	0.25	Na_2HPO_4	0.33	6.47	84	425	30	54	$0.29D, 0.71G_3$
A47	0.25	Na_2SiO_3	0.53	7.62	69	398	25	43	0.55D, 0.45I
A71	0.21	NaOH	1.16	8.34	68	390	24	52	$0.22D, 0.34T, 0.44G_3$
A12	0.20	Na_2SO_4	0.66	6.90	54	345	20	29	$0.22D, 0.78G_3$
A53	0.26	Na_2SO_3	0.36	6.44	47	329	17	22	0.22D, 0.78I
A52	0.23	$Na_2S_2O_3$	0.47	6.15	49	299	18	14	$0.12D, 0.88G_3$
A54	0.22	Na_2S	1.03	8.05	49	317	18	23	$0.22D, 0.78G_3$

[a]Anion concentration of 0.1 ppm is based on complete dissociation of the amount of the salt added to the feedwater without consideration of the actual dissociation equilibria at 25 or 289°C.
[b]Specimens were exposed to the environment for ~20 h at 289°C before straining at a rate of 1×10^{-6} s^{-1}.
[c]Ductile (D), transgranular (T), granulated (G), intergranular (I), in terms of the fraction of the reduced cross-sectional area. Characterization of the fracture surface morphologies is in accordance with the illustrations and definitions provided in Alternate Alloys for BWR Pipe Applications: Sixth Semiannual Progress Report, April-September 1980, General Electric Company Report NEDC-23750-8, pp. 5-70 to 5-81.

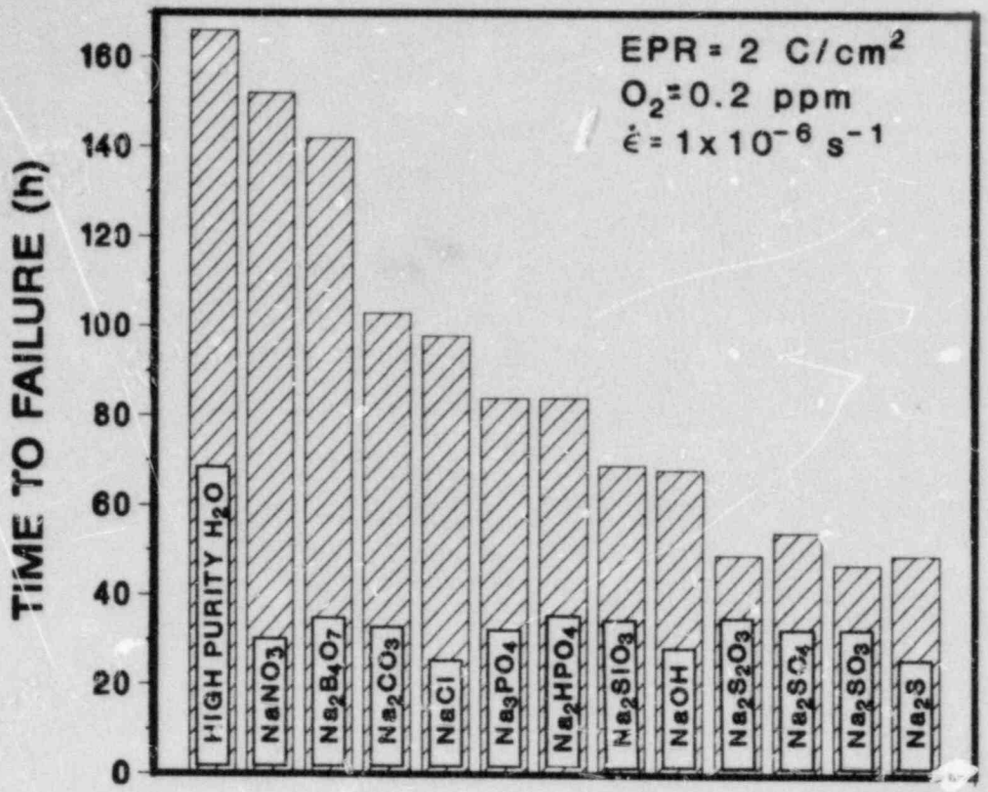

Fig. 1.16. Effect of Various Sodium Salts at an Anion Concentration of 0.1 ppm in Water Containing 0.2 ppm Dissolved Oxygen on the Time-to-Failure of Lightly Sensitized Type 304 SS Specimens in CERT Experiments at 289°C and a Strain Rate of 1×10^{-6} s^{-1}.

containing ~0.2 ppm dissolved oxygen and a conductivity of ~1 μS/cm by the addition of Na_2SO_4, Na_2CO_3, NaF, and $NaNO_3$.[19] Nitrate was least deleterious; sulfate and carbonate were equivalent and produced the highest degree of IGSCC in CERT tests at a strain rate of 3.7×10^{-7} s^{-1}. The fracture mode was ductile plus intergranular for the specimens in the different environments including high-purity water with ~0.2 ppm dissolved oxygen.

The effect of the different anions added in acid form on the SCC susceptibility of the steel has also been investigated. The anion concentration was ~0.1 ppm as in the previous experiments and yielded conductivity values of $\lesssim$1 μS/cm in water with ~0.2 ppm dissolved oxygen. A gas mixture of 0.035% CO_2, 0.54% O_2, and the balance nitrogen was bubbled through deoxygenated feedwater to establish the desired oxygen and carbonate concentrations at 25°C. The other species were added as dilute acids. The results in

Table 1.10 indicate that the silicate, borate, nitrate, and phosphate produced the smallest reduction in CERT parameters relative to high-purity water; carbonate and chloride were somewhat more deleterious and the sulfur species caused the highest degree of IGSCC. The time to failure of the specimens in the different environments is shown in Fig. 1.17. The fracture morphology was ductile plus intergranular (i.e., granulated) in these impurity environments.

A comparison of these results with the information in Table 1.9 and Fig. 1.16 for sodium salts indicates that nitrate, borate, carbonate, and chloride are somewhat more deleterious when added in acid form; however, there is essentially no difference with respect to the sulfur species. It was reported previously[20] that the pH of dilute H_2SO_4-Na_2SO_4 solutions and additions of other metal cations (viz., Fe^{3+}, Cr^{3+}, Al^{3+}, Fe^{2+}, Ni^{2+}, Cu^{2+}, and Zn^{2+}) with 0.1 ppm sulfate did not produce significant differences in the IGSCC behavior of the lightly sensitized steel in water with 0.2 ppm dissolved oxygen.

It is clear from the present results that various anion species at low concentrations (corresponding to conductivity values of $\lesssim$1 μS/cm) differ considerably in their effect on the IGSCC behavior of the steel. Consequently, it is unlikely that the cracking behavior of sensitized austenitic stainless steels in laboratory tests or in reactor coolant systems can be correlated with the conductivity and pH without specific knowledge of the various ions present. In the case of reactor coolant systems, the standard instrumentation used for analyses of the coolant water is, in general, not adequate to determine the concentration of sulfur species that are particularly deleterious from the standpoint of IGSCC even though sulfate is likely to be present in BWR water at low concentrations ($\lesssim$0.1 ppm) from normal resin leakage and from resin regeneration and replacement operations.

A semi-continuous on-line instrument based on ion chromatography, ion-exchan separation, followed by either conductivity or photometric detection that is capable of measuring ion concentrations at the part-per-billion to part-per-million levels has been developed[21]. The instrument has been used to evaluate condensate polisher efficiency and to detect polisher resin leaks in the secondary cycle of several PWRs.[22] Because of

TABLE 1.10. Influence of Different Acids at an Anion Concentration[a] of 0.1 ppm on the SCC Susceptibility of Sensitized (EPR = 2 C/cm^2) Type 304 SS Specimens[b] (Heat No. 30956) in 289°C Water Containing 0.2 ppm Dissolved Oxygen

	Feedwater Chemistry				CERT Parameters				
Test No.	Oxygen, ppm	Impurity Species	Cond. at 25°C, μS/cm	pH at 25°C	Failure Time, h	Maximum Stress, MPa	Total Elong., %	Reduction in Area, %	Fracture Morphology[c]
A2	0.24	-	0.14	6.12	166	493	60	66	0.80D, 0.20T
A59	0.18	H_2SiO_3	0.12	6.25	123	514	44	48	$0.63D, 0.37G_3$
A57	0.23	H_3BO_3	0.14	6.30	109	492	39	41	$0.59D, 0.41G_3$
A56	0.24	HNO_3	0.70	5.75	101	481	36	41	$0.69D, 0.31G_3$
A64	0.23	H_3PO_4	0.53	5.90	99	460	36	53	$0.44D, 0.56G_3$
A60	0.22	H_2CO_3	0.69	5.77	91	459	33	38	$0.52D, 0.48G_2$
A58	0.26	HCl	1.19	5.58	83	440	30	37	$0.43D, 0.57G_2$
A3	0.20	H_2SO_4	0.91	5.74	79	402	29	37	$0.22D, 0.78G_2$
A63	0.23	H_2SO_4	0.94	5.75	54	326	19	18	0.25D, 0.75I
A61	0.21	H_2SO_3	0.6?	5.78	51	320	18	20	$0.22D, 0.78G_3$

[a]Anion concentration of 0.1 ppm is based on complete dissociation of the amount of acid added to the feedwater without consideration of actual dissociation equilibria at 25 or 289°C.
[b]Specimens were exposed to the environment for ~20 h at 289°C before straining at a rate of 1×10^{-6} s^{-1}.
[c]Ductile (D), transgranular (T), granulated (G), and intergranular (I) in terms of the fraction of the reduced cross-sectional area. Characterization of the fracture surface morphologies is in accordance with the illustrations and definitions provided in Alternate Alloys for BWR Pipe Applications: Sixth Semiannual Progress Report, April-September 1980, General Electric Company Report NEDC-23750-8, pp. 5-70 to 5-81.

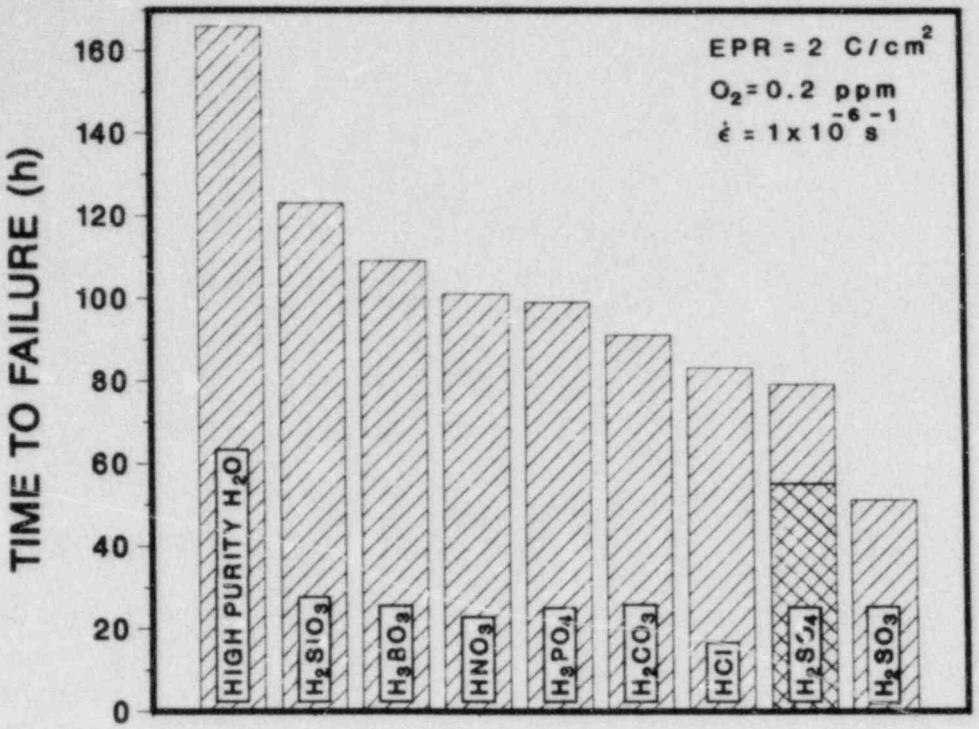

Fig. 1.17. Influence of Various Acids at an Anion Concentration of 0.1 ppm in Water Containing 0.2 ppm Dissolved Oxygen on the Time-to-Failure of Lightly Sensitized (EPR = 2 C/cm^2) Type 304 SS Specimens in CERT Experiments at 289°C and a Strain Rate of 1 x 10^{-6} s^{-1}.

its high sensitivity, the instrument was able to detect significant increases in the sodium, sulfate, and chloride ion concentrations during plant transients and also to demonstrate that the efficiency of the polisher for the removal of the sulfate ion was relatively poor (possibly due to the condition of the resin, residence time in the bed, and reaction kinetics). Measurements of the concentration of various ionic species present in BWR recirculation loop water and the corrosion potential of the steel at 289°C would be quite useful in determining the role of the environment in the propagation of shallow cracks.

b. Effect of Temperature on SCC Susceptibility

The effect of temperature over the range of 110 to 320°C on the SCC behavior of lightly sensitized (EPR = 2 C/cm^2) Type 304 SS was investigated in high-purity water and in water containing 0.1 and 1.0 ppm sulfate

as H_2SO_4 at a dissolved oxygen concentration of 0.2 ppm. The open-circuit corrosion potential of Type 304 SS and the potential of a platinum electrode were measured against an external 0.1M KCl/AgCl/Ag reference electrode during each CERT experiment.[23] The values were converted to the standard hydrogen electrode based on a correction for the thermocell and liquid junction potentials at each temperature.[24] As in previous CERT experiments,[20,25] the specimens were exposed to the environment for ~20 h before straining at a rate of 1×10^{-6} s^{-1}. The SCC susceptibility in terms of the various CERT parameters is given in Tables 1.11 to 1.13 for high-purity water and water with 0.1 and 1.0 ppm sulfate as H_2SO_4. The crack growth rates are based on a measurement of the depth of the largest crack in an enlarged micrograph of the fracture surface and the time period from the onset of yield to the point of maximum load on the tensile curve, as described in the previous report.[25] The dependence of the time-to-failure and the crack growth rate on temperature is shown in Figs. 1.18 and 1.19, respectively. In terms of the time-to-failure data,

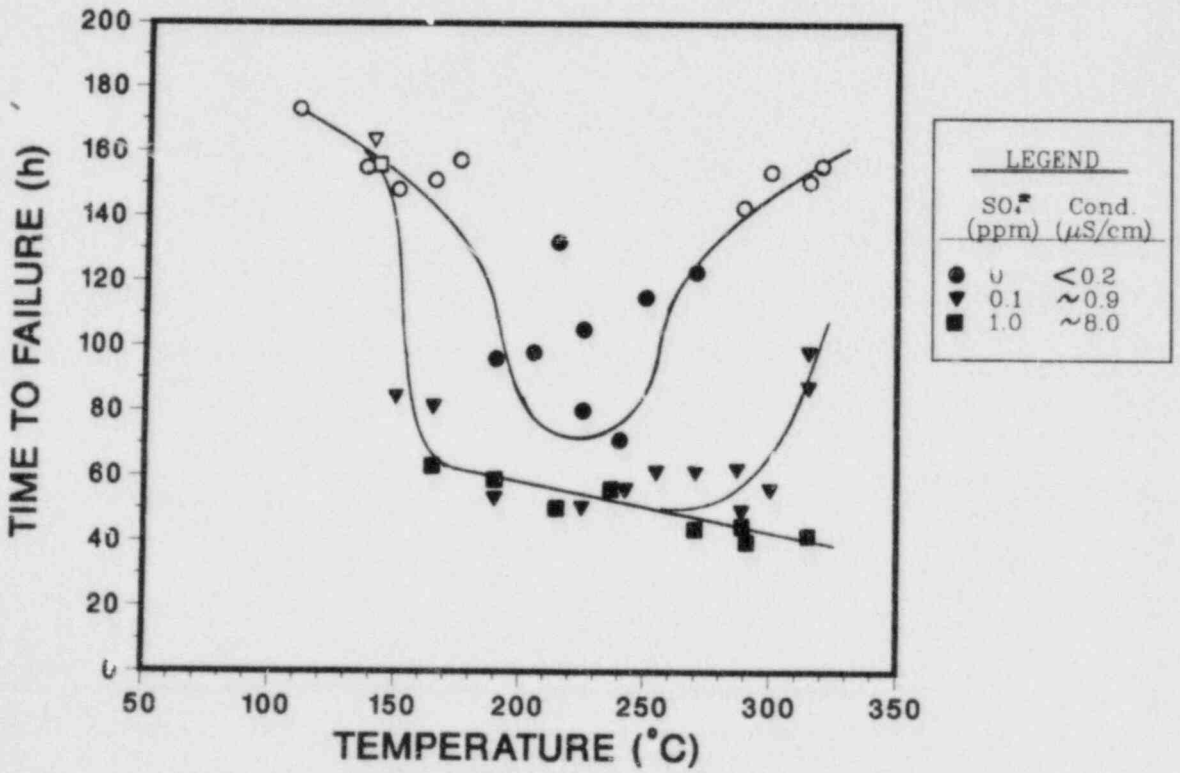

Fig. 1.18. Effect of Temperature on the Time-to-Failure of Lightly Sensitized (EPR = 2 C/cm^2) Type 304 SS Specimens in CERT Experiments at a Strain Rate of 1×10^{-6} s^{-1} in Water Containing 0.2 ppm Dissolved Oxygen and 0, 0.1, and 1 ppm Sulfate as H_2SO_4. Open and closed symbols denote either ductile or ductile plus transgranular and ductile plus intergranular fracture morphology, respectively.

TABLE 1.11. Effect of Temperature on the SCC Susceptibility and Crack Growth Rate of Lightly Sensitized (EPR = 2 C/cm^2) Type 304 SS Specimens[a] (Heat No. 30956) from CERT Experiments in Water Containing 0.2 ppm Dissolved Oxygen

Test No.	Temp., °C	Feedwater Chemistry				Failure Time, h	Maximum Stress, MPa	Total Elong., %	Reduction in Area, %	Fracture Morphology[b]	SCC Growth Rate,[c]	
		Oxygen, ppm	Sulfate, ppm	Cond., µS/cm	pH at 25°C						mm·h^{-1}	m·s^{-1}
123	320	0.17	0	0.11	6.28	156	534	56	72	1.07D	0	0
96	315	0.21	0	0.13	6.19	151	538	55	75	1.00D	0	0
122	300	0.18	0	0.19	6.18	154	538	55	76	0.97D, 0.03T	1.9×10^{-3}	5.3×10^{-10}
2	289	0.25	0	0.20	6.80	143	492	50	52	0.69D, 0.31T	7.9×10^{-3}	2.2×10^{-9}
94	270	0.24	0	0.12	6.08	123	513	44	49	0.43D, 0.57G_3	1.4×10^{-2}	3.9×10^{-9}
98	250	0.22	0	0.10	6.21	115	499	41	46	0.28D, 0.72G_3	1.3×10^{-2}	3.6×10^{-9}
91	240	0.24	0	0.10	6.15	71	328	25	31	0.40D, 0.60I	3.3×10^{-2}	9.2×10^{-9}
95	225	0.23	0	0.12	6.15	105	448	40	64	0.41D, 0.59I	1.7×10^{-2}	4.7×10^{-9}
97	225	0.21	0	0.11	6.19	80	448	29	33	0.50D, 0.50I	2.2×10^{-2}	6.1×10^{-9}
125	215	0.21	0	0.14	6.17	132	516	48	72	0.80D, 0.20I	1.4×10^{-2}	3.9×10^{-9}
119	205	0.23	0	0.14	6.26	98	456	35	66	0.67D, 0.33G_3	1.9×10^{-2}	5.2×10^{-9}
92	190	0.24	0	0.13	6.07	96	449	34	62	0.67D, 0.33I	2.3×10^{-2}	6.4×10^{-9}
124	175	0.22	0	0.14	6.23	157	509	57	80	1.0D	0	0
120	165	0.21	0	0.15	6.24	151	502	54	80	0.79D, 0.21T	7.2×10^{-3}	2.0×10^{-9}
121	150	0.19	0	0.13	6.24	148	491	53	80	0.99D, 0.01T	1.7×10^{-3}	4.7×10^{-10}
93	140	0.22	0	0.12	6.10	155	514	56	81	1.00D	0	0
99	110	0.20	0	0.12	6.20	173	523	62	84	1.00D	0	0

[a]Specimens were exposed to the environment for ~20 h before straining at a rate of 1×10^{-6} s^{-1}.

[b]Ductile (D), transgranular (T), granulated (G), intergranular (I), in terms of the fraction of the reduced cross-sectional area. Characterization of the fracture surface morphologies is in accordance with the illustrations and definitions provided in Alternate Alloys for BWR Pipe Applications: Sixth Semiannual Progress Report, April-September 1980, General Electric Company Report NEDC-23750-8, pp. 5-70 to 5-81.

[c]SCC growth rates are based on measurement of the depth of the largest crack in an enlarged micrograph of the fracture surface and the time period from the onset of yield to the point of maximum load on the tensile curve.

TABLE 1.12. Effect of Temperature on the SCC Susceptibility and Crack Growth Rate of Lightly Sensitized (EPR = 2 C/cm^2) Type 304 SS Specimens[a] (Heat No. 30956) from CERT Experiments in Water Containing 0.2 ppm Dissolved Oxygen and 0.1 ppm Sulfate as H_2SO_4

Test No.	Temp., °C	Feedwater Chemistry				Failure Time, h	Maximum Stress, MPa	Total Elong., %	Reduction in Area, %	Fracture Morphology[b]	SCC Growth Rate,[c]	
		Oxygen, ppm	Sulfate, ppm	Cond., µS/cm	pH at 25°C						mm·h^{-1}	m·s^{-1}
116	315	0.20	0.1	0.89	5.70	98	477	35	41	0.44D, 0.28T, 0.28I	3.0×10^{-2}	8.3×10^{-9}
100	315	0.22	0.1	0.87	5.71	87	435	31	48	0.33D, 0.44T, 0.23I	2.3×10^{-2}	6.4×10^{-9}
118	300	0.19	0.1	0.91	5.75	56	382	20	20	0.32D, 0.68I	4.1×10^{-2}	1.1×10^{-8}
17	289	0.18	0.1	0.90	5.80	49	315	18	10	0.08D, 0.92I	8.2×10^{-2}	2.3×10^{-8}
115	289	0.22	0.1	0.90	5.76	62	372	22	21	0.22D, 0.78G_3	3.2×10^{-2}	8.9×10^{-9}
101	270	0.22	0.1	0.87	5.75	61	324	22	21	0.21D, 0.79I	3.9×10^{-2}	1.1×10^{-8}
104	255	0.20	0.1	0.90	5.78	61	358	22	30	0.25D, 0.75I	3.9×10^{-2}	1.1×10^{-8}
102	240	0.22	0.1	0.87	5.73	56	339	20	19	0.35D, 0.65I	4.0×10^{-2}	1.1×10^{-8}
103	225	0.22	0.1	0.88	5.76	50	317	18	26	0.28D, 0.72I	6.0×10^{-2}	1.7×10^{-8}
105	190	0.23	0.1	0.86	5.68	53	340	19	24	0.31D, 0.69I	4.4×10^{-2}	1.2×10^{-8}
106	165	0.19	0.1	0.86	5.71	81	434	29	46	0.44D, 0.56I	3.1×10^{-2}	8.6×10^{-9}
117	150	0.20	0.1	0.88	5.77	84	405	30	27	0.36D, 0.64I	2.7×10^{-2}	7.5×10^{-9}
107	140	0.22	0.1	0.87	5.75	163	504	59	81	1.00D	0	0

[a]Specimens were exposed to the environment for ~20 h before straining at a rate of 1×10^{-6} s^{-1}.

[b]Ductile (D), transgranular (T), granulated (G), intergranular (I), in terms of the fraction of the reduced cross-sectional area. Characterization of the fracture surface morphologies is in accordance with the illustrations and definitions provided in Alternate Alloys for BWR Pipe Applications: Sixth Semiannual Progress Report, April-September 1980, General Electric Company Report NEDC-23750-8, pp. 5-70 to 5-81.

[c]SCC growth rates are based on measurement of the depth of the largest crack in an enlarged micrograph of the fracture surface and the time period from the onset of yield to the point of maximum load on the tensile curve.

TABLE 1.13. Effect of Temperature on the SCC Susceptibility and Crack Growth Rate of Lightly Sensitized (EPR = 2 C/cm^2) Type 304 SS Specimens[a] (Heat No. 30956) from CERT Experiments in Water Containing 0.2 ppm Dissolved Oxygen and 1.0 ppm Sulfate as H_2SO_4

Test No.	Temp., °C	Feedwater Chemistry				Failure Time, h	Maximum Stress, MPa	Total Elong., %	Reduction in Area, %	Fracture Morphology[b]	SCC Growth Rate,[c]	
		Oxygen, ppm	Sulfate, ppm	Cond., µS/cm	pH at 25°C						mm•h^{-1}	m•s^{-1}
108	315	0.22	1.0	8.0	4.78	42	264	15	16	0.14D, 0.86G_3	7.1×10^{-2}	2.0×10^{-8}
39	289	0.20	1.0	8.0	4.80	45	291	16	15	0.19D, 0.81I	9.6×10^{-2}	2.4×10^{-8}
19	289	0.20	1.0	9.0	4.80	40	277	14	11	0.06D, 0.94I	1.1×10^{-1}	3.1×10^{-8}
109	270	0.23	1.0	8.3	4.77	44	291	16	19	0.22D, 0.78I	5.3×10^{-2}	1.5×10^{-8}
110	240	0.23	1.0	8.2	4.77	56	336	20	23	0.14D, 0.86I	5.6×10^{-2}	1.6×10^{-8}
114	215	0.27	1.0	8.0	4.77	50	307	18	15	0.14D, 0.86I	8.1×10^{-2}	2.3×10^{-8}
111	190	0.25	1.0	8.1	4.77	59	359	21	18	0.15D, 0.85I	6.2×10^{-2}	1.7×10^{-8}
113	165	0.26	1.0	8.2	4.78	63	395	23	17	0.05D, 0.95I	5.0×10^{-2}	1.4×10^{-8}
112	140	0.21	1.0	8.2	4.78	156	506	56	-	-	-	-

[a]Specimens were exposed to the environment for ~20 h before straining at a rate of 1×10^{-6} s^{-1}.
[b]Ductile (D), transgranular (T), granulated (G), intergranular (I), in terms of the fraction of the reduced cross-sectional area. Characterization of the fracture surface morphologies is in accordance with the illustrations and definitions provided in Alternate Alloys for BWR Pipe Applications: Sixth Semiannual Progress Report, April-September 1980, General Electric Company Report NEDC-23750-8, pp. 5-70 to 5-81.
[c]SCC growth rates are based on measurement of the depth of the largest crack in an enlarged micrograph of the fracture surface and the time period from the onset of yield to the point of maximum load on the tensile curve.

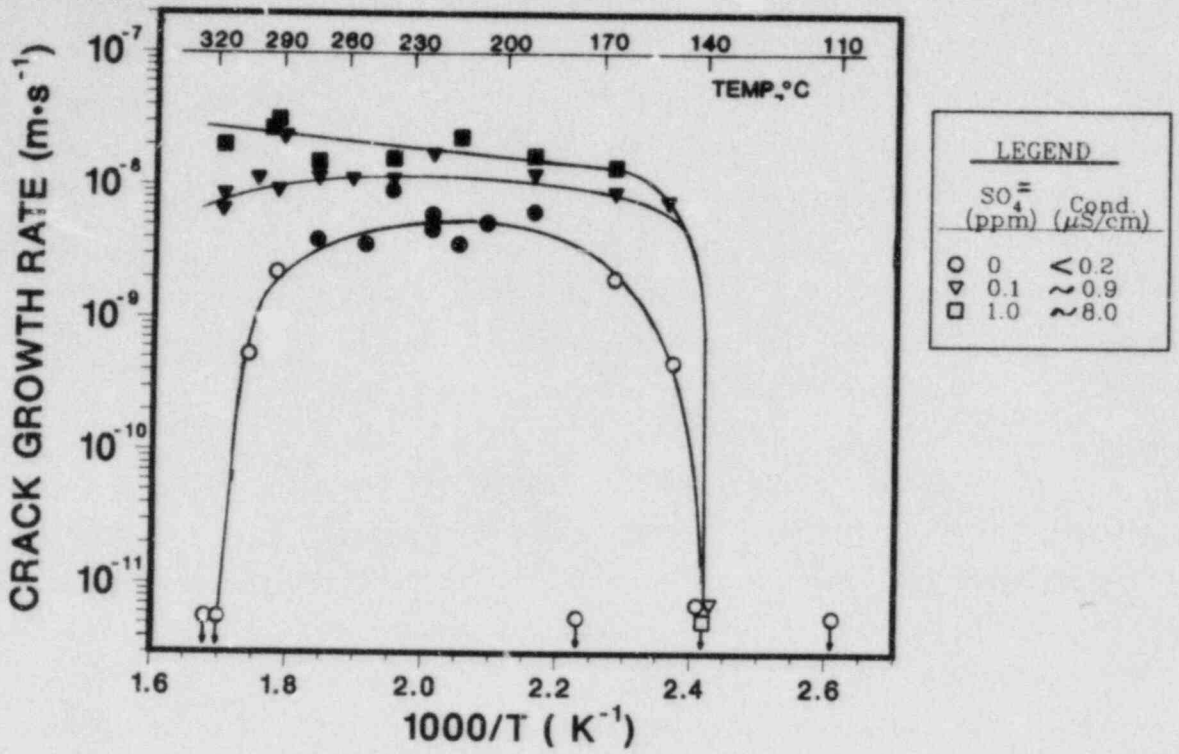

Fig. 1.19. Effect of Temperature on the Crack Growth Rate of Lightly Sensitized (EPR = 2 C/cm^2) Type 304 SS Specimens from CERT Experiments at a Strain Rate of 1 x 10^{-6} s^{-1} in Water Containing 0.2 ppm Dissolved Oxygen and 0, 0.1, and 1 ppm Sulfate as H_2SO_4. Open and closed symbols denote either ductile or ductile plus transgranular and ductile plus intergranular fracture morphology, respectively.

the maximum IGSCC susceptibility occurs at temperatures between ~200 and 250°C in high-purity water with ~0.2 ppm dissolved oxygen. The addition of 0.1 ppm sulfate increases both the degree of susceptibility (i.e., decreases the time-to-failure) and the temperature range over which maximum susceptibility occurs. At a sulfate concentration of 1.0 ppm, the IGSCC susceptibility increases markedly at temperatures $\gtrsim$150°C; however, the decrease in susceptibility at temperatures above ~250°C observed in high-purity water does not occur. Relative to high-purity water, sulfate at a concentration of 1 ppm is most deleterious at high temperatures.

The relatively high degree of scatter in the time-to-failure data for the CERT experiments in high-purity water at temperatures between ~170 and 250°C compared to the impurity environments can be attributed to the

difference in the number of cracks that initiate at the specimen surface. In the impurity environments, typically three to five thumbnail SCC cracks of approximately equal depth were present on the fracture surface, whereas in high-purity water only one deep crack was evident in the specimens for which the failure times fall above the curve in Fig. 1.18. However, a large crack depth coupled with a long failure time (i.e., the time period from yield to the point of maximum load) produced crack-growth-rate values that are consistent with data based on a larger number of cracks, smaller maximum crack depths, and a correspondingly shorter failure times.

The temperature dependence of the crack growth rates in the three environments are shown in Fig. 1.19. These data also reveal the large effect of sulfate at low concentrations, particularly at temperatures above ~270°C. The broad maximum in the crack growth rate of sensitized Type 304 SS at temperatures between ~200 and 250°C has also been observed in constant load experiments in high-purity water with 40 ppm dissolved oxygen,[26] and in CERT experiments in high-purity water with 0.2[27] and 8 ppm[28] dissolved oxygen and in water containing 8 ppm oxygen and 500 and 1500 ppm boron as H_3BO_3.[28] In the latter experiments, boric acid at relatively high concentrations did not have a deleterious effect on the SCC susceptibility of the steel over the temperature range of 60 to 360°C. At temperatures below ~150°C, boric acid and lithium hydroxide inhibited SCC of sensitized Type 304 SS in aerated water.[28]

A transition from an intergranular to a ductile fracture mode occurred at temperatures above ~270°C and below ~190°C in high-purity water with 0.2 ppm dissolved oxygen. In the impurity environments, ductile failures occurred at temperatures below ~150°C in water with 0.1 and 1.0 ppm sulfate. The transition in the fracture mode (Table 1.11) from intergranular to transgranular and ultimately to 100% ductile failure in high-purity water with 0.2 ppm dissolved oxygen as the temperature increases from ~270 to 315°C can, in part, be explained by the dependence of the open-circuit corrosion potential of the steel on temperature. The measurements of the steady-state corrosion potential of the steel shown in Fig. 1.20 indicate that the potential decreases more rapidly with temperature above ~250°C, and approaches

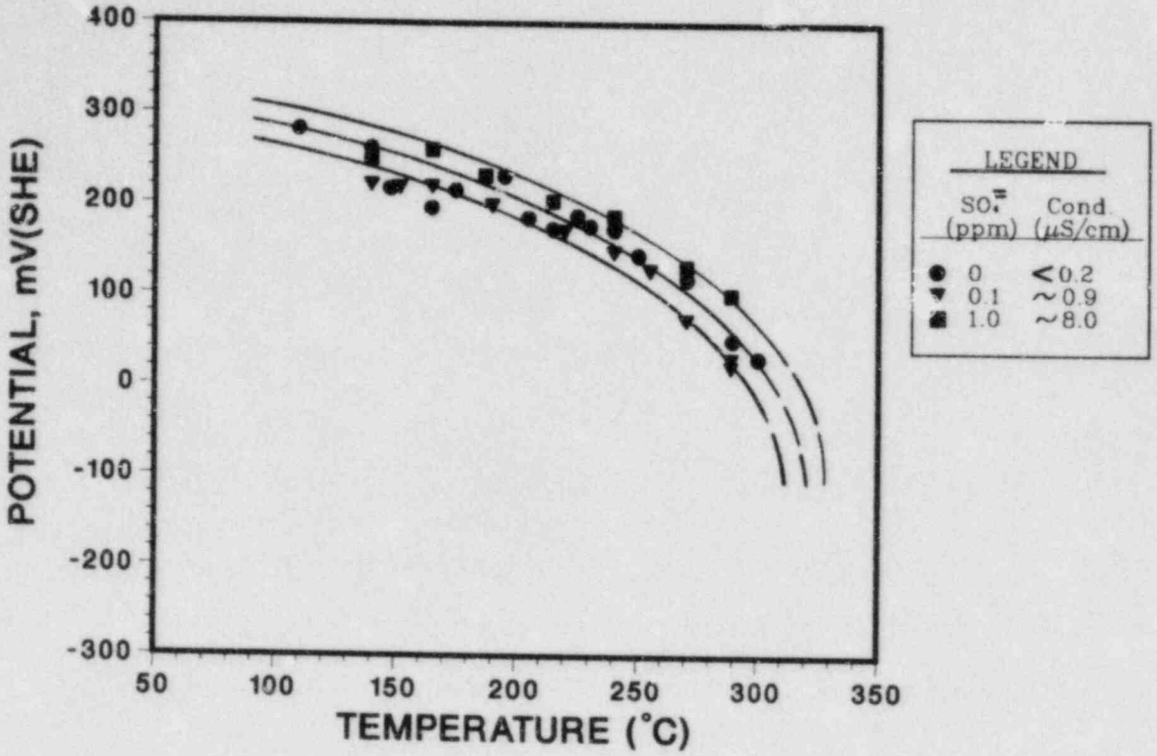

Fig. 1.20. Effect of Temperature on the Electrochemical Potential of Type 304 SS in Water Containing 0.2 ppm Dissolved Oxygen and 0, 0.1, and 1 ppm Sulfate as H_2SO_4.

~0 mV(SHE) at 315°C. Actual measurements of the corrosion potential at this temperature were not possible because of failure of the reference electrode due to softening of the teflon tubing and loss of the electrolyte solution. If the behavior at 315°C is similar to that at 289°C as shown in Fig. 1.21,[29] a relatively small decrease in the potential [i.e., from +100 to ~0 mV(SHE)] at a conductivity of ~0.1 μS/cm produces a transition from intergranular to predominately ductile plus transgranular fracture. A similar transition in failure mode at a potential of ~0 mV(SHE) will not occur for conductivity values of 0.9 and 8.0 μS/cm, since the potentials would have to drop below -475 and -560 mV(SHE), respectively. As indicated in Tables 1.12 and 1.13, the fracture morphology of the specimens at 315°C is predominantly intergranular in the impurity environments.

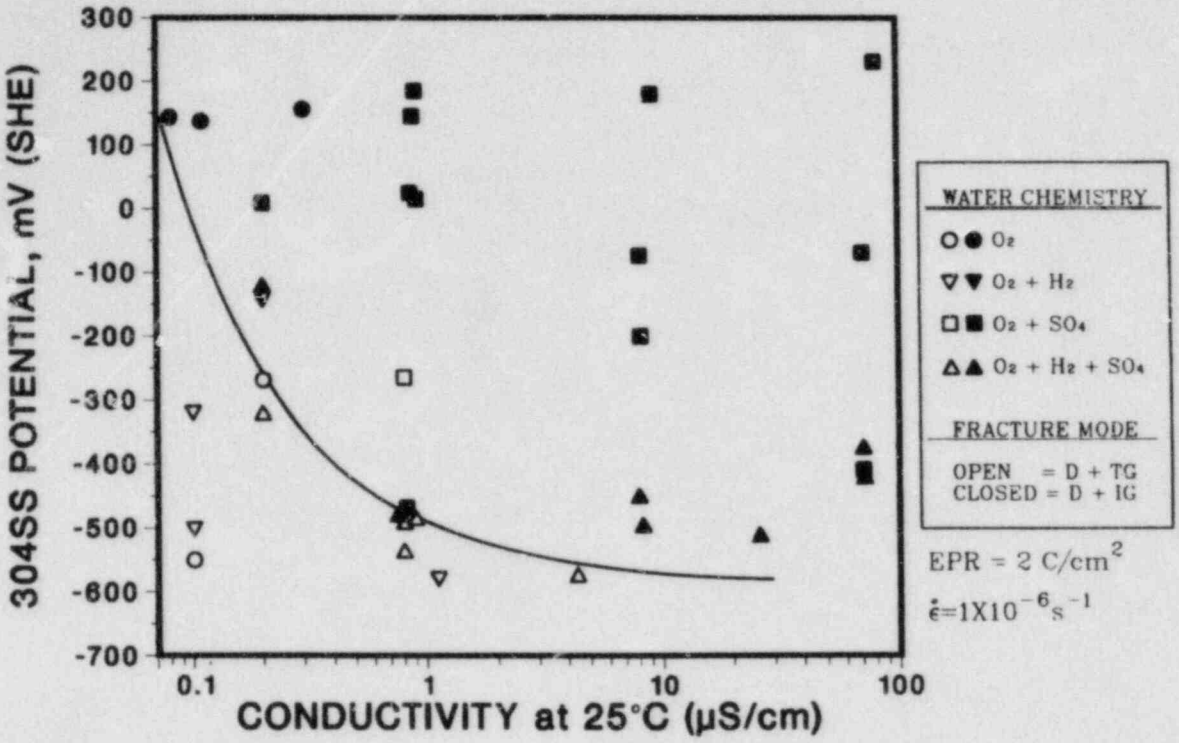

Fig. 1.21. Regime of Corrosion Potential and Feedwater Conductivity that Results in Immunity to IGSCC of Lightly Sensitized (EPR = 2 C/cm^2) Type 304 SS in CERT Experiments at 289°C in Simulated BWR-Quality Water Containing Dissolved Oxygen, Hydrogen, and Sulfate as H_2SO_4.[28]

In general, the temperature dependence of the crack growth rate of sensitized Type 304 SS observed in CERT (Refs. 27 and 28 and Fig. 1.19) and constant-load[26] experiments, resembles the behavior of Stage II (K-independent) crack growth of Fe-18Ni maraging steels in hydrogen,[30-32] AISI 4130 steel in hydrogen[33-35] and distilled water,[35] H-11 steel in hydrogen,[36] and AISI 4340 steel in hydrogen,[37,38] H_2S[39,40] and water.[37,41,42] In the gaseous environments, the crack growth rates obtained from fracture-mechanics-type specimens exhibit three distinct regions of temperature dependence. In the low-temperature range ($\lesssim$0°C in the case of the maraging and 4130 steels and $\lesssim$60°C in the 4340 and H-11 steels), hydrogen-assisted Stage II crack growth is a thermally activated process and follows an Arrhenius-type relationship [$da/dt \approx \exp(-\Delta H/RT)$]. At somewhat higher temperatures, the rates reach a maximum and then decrease rapidly with further increases in temperature. The latter transition is strongly dependent on the yield strength of the material and the hydrogen pressure, i.e., the temperature at which the material becomes

essentially immune to gaseous hydrogen embrittlement, increases with hydrogen pressure and yield strength. The crack growth rates of the maraging steels in hydrogen and the 4340 steel in H_2S decrease precipitously as the temperature increases compared to the behavior of the 4340 and 4130 steels in hydrogen. In the low-temperature region, the fracture mode of the 4340 steel is predominantly intergranular with respect to the prior austenite grain boundaries, and as the temperature increases, the amount of transgranular dimpled separation increases. For this material, the effect of temperature on the fracture surface morphology in H_2S was essentially identical to that in hydrogen.[40] Over the temperature range of ~1 to 90°C in water, the crack growth rate of AISI 4130 steel increases rapidly with temperature[35] and reaches a maximum value at ~70 to 90°C. Data were not obtained at higher temperatures to determine if the crack growth rates decrease as in the case of the gaseous environments.

In these materials, the transition in the fracture mode and the precipitous decrease in the crack growth rate has been attributed to the partitioning or distribution of hydrogen to different microstructural elements in the low-alloy steel, which is a function of temperature and hydrogen pressure.[40] At low temperatures, it is postulated that most of the hydrogen concentrates at the prior austenite boundaries and crack growth is controlled by the supply of hydrogen from the environment, whereas at higher temperatures, more of the hydrogen may go into the martensite lattice. The gas-adsorbate equilibrium may also shift with temperature in a manner which further reduces the availability of hydrogen at the more susceptible sites and elsewhere in the microstructure, and thus contributes to the decrease in crack growth rate at higher temperature.[40]

Ford[43] has recently reviewed various mechanisms for environmentally controlled fracture and has suggested that there are many common interrelated steps or microprocesses involved in crack advance in ductile alloy/aqueous environments either by hydrogen embrittlement or slip dissolution at the crack front. For example, for given conditions of electrode potential, pH, and anion concentration at the crack tip, both mechanisms depend on the rates of liquid diffusion of species to and from the crack tip, passivation, and oxide rupture since these factors affect the charge passed

per unit time in the slip-dissolution model and the adatom coverage and subsequent hydrogen permeation in hydrogen embrittlement models. Thus, it is possible that the mechanisms associated with hydrogen embrittlement and slip dissolution at the crack tip operate simultaneously. A better understanding of the relative contribution of these mechanisms to IGSCC of sensitized Type 304 SS under simulated BWR-water-chemistry conditions can be obtained from investigations of the influence of temperature and loading mode (i.e., tension versus torsion) on crack propagation behavior. This information will contribute to improved predictive capability for material performance and a better basis for evaluation of remedial actions regarding stress corrosion cracking of reactor materials.

E. References for Chapter I

1. J. Y. Park, in Materials Science and Technology Division Light-Water-Reactor Safety Research Program: Quarterly Progress Report, October-December 1983, NUREG/CR-3689 Vol. IV, ANL-83-85 Vol. IV (August 1984), pp. 22-25.

2. J. Y. Park and W. J. Shack, in Materials Science and Technology Division Light-Water-Reactor Safety Research Program: Quarterly Progress Report, October-December 1983, NUREG/CR-3689 Vol. IV, ANL-83-85 Vol. IV (August 1984), pp. 26-30.

3. P. S. Maiya and W. J. Shack, in Light-Water-Reactor Safety Research Program: Quarterly Progress Report, January-March 1983, NUREG/CR-3689 Vol. I, ANL-83-85 Vol. I (April 1983), pp. 34-46.

4. P. S. Maiya and W. J. Shack, in Light Water Reactor Safety Research Program: Annual Report, October 1982-September 1983, NUREG/CR-3806, ANL-84-36 (June 1984), pp. 58-83.

5. P. S. Maiya and W. J. Shack, "Effects of Nominal and Crack-tip Strain Rate on IGSCC Susceptibility in CERT Tests," Proceedings of the Symposium on Localized Chemistry and Mechanics in Environment-Assisted Fracture, TMS-AIME Fall Mtg., Philadelphia, PA, October 3-6, 1983, in press.

6. P. S. Maiya and W. J. Shack, in Light-Water-Reactor Safety Research Program: Quarterly Progress Report, October-December 1983, NUREG-CR-3689 Vol. IV, ANL-83-85 Vol. IV (August 1984), pp. 31-50.

7. E. W. Hart, Constitutive Relations for the Non-elastic Deformation of Metals, J. Eng. Mater. Technol. 93 (3), p. 193 (1976).

8. W. J. Shack, Measurement of Throughwall Residual Stresses in Large-Diameter Type 304 Stainless Steel Piping Butt Weldments, ANL-82-15, Argonne National Laboratory (1982).

9. W. J. Shack et al., Environmentally Assisted Cracking in Light Water Reactors: Annual Report, October 1982-September 1983, NUREG/CR-3806, ANL-84-36 (June 1984), pp. 83-92.

10. D. P. Siegwarth, K. A. Friedman, and D. A. McNea, A Review of Condensate Demineralizer Regeneration Procedures, EPRI Topical Report NP-2975 (April 1983).

11. M. A. Sadler, J. C. Bates, D. J. Gardner, and A. D. Thomas, A Study of Performance of the Triobed Condensate Polishing at Doel Power Station, Nuclear Energy 18, 389-399 (1979).

12. C. C. Stouffer and P. C. Doss, Condensate Polisher Resin Leakage Quantification and Resin Transport Studies, EPRI Topical Report NP-2981 (April 1983).

13. R. H. Asay, J. Blok, and J. H. Holloway, Water Quality in Boiling Water Reactors, EPRI Final Report, NP-1603 (November 1980).

14. A. D. Miller, Brunswick-2 Water Chemistry, EPRI Interim Report, NP-1795 (April 1981).

15. A. D. Miller, Water Chemistry Characterizations of a Boiling Water Reactor, Nucl. Tech. 37, 111-117 (1978).

16. B. Francis, F. M. Kustas, and E. C. Martin, Evaluation of BWR Resin Intrusions on Stress Corrosion Cracking of Reactor Structural Materials, Battelle Pacific Northwest Laboratories, Second Progress Report, January-June 1980, EPRI Project RP 1562-3 (January 1981).

17. R. J. Kurtz, D. W. Shannon, B. Francis, F. M. Kustas, and P. L. Koelmstedt, Evaluation of BWR Resin Intrusions on Stress Corrosion Cracking of Reactor Structural Materials, EPRI Final Report, NP-3145 (June 1983).

18. J. W. Cobble, R. C. Murry, Jr., P. J. Turner, and K. Chen, High-Temperature Thermodynamic Data for Species in Aqueous Solution, EPRI Final Report, NP-2400 (May 1982).

19. R. B. Davis and M. E. Indig, The Effect of Aqueous Impurities on the Stress Corrosion Cracking of Austenitic Stainless Steels in High-Temperature Water, Corrosion 83, Anaheim, CA, April 1983, National Association of Corrosion Engineers, Paper Number 128.

20. W. E. Ruther, W. K. Soppet, and T. F. Kassner, in Environmentally Assisted Cracking in Light-Water Reactors: Annual Report, October 1982 to September 1983, NUREG/CR-3086, ANL-84-36 (June 1984), pp. 101-124.

21. J. L. Simpson, M. N. Robles, and S. A. Moss, In-Plant System for Continuous Low-Level Ion Measurement in Steam Producing Water, General Electric Company Report, ASRD-00174 (February 1982).

22. M. N. Robles and J. L. Simpson, On-Line Ion Chromatographic Measurement of Impurities in the Secondary Water/Steam Systems of a Pressurized Water Reactor, General Electric Company Report, ASRD-00115 (June 1982).

23. P. L. Andresen, Innovations in Experimental Techniques for Testing in High-Temperature Aqueous Environments, General Electric Company CRD Report 81CRD 088 (May 1981).

24. D. D. Macdonald, A. C. Scott, and P. Wentrcek, External Reference Electrodes for Use in High-Temperature Aqueous Systems, J. Electrochem. Soc. 126(6), 908-911 (1979).

25. W. E. Ruther, W. K. Soppet, and T. F. Kassner, in Materials Science and Technology Division Light-Water Reactor Safety Research Program: Quarterly Progress Report, October-December 1983, NUREG/CR-3689 Vol. IV, ANL-83-85 Vol. IV (August 1984), pp. 51-91.

26. N. Ohnaka, S. Syoji, A. Minato, and K. Tanno, "Environmental Effects on the Intergranular Stress Corrosion Cracking Susceptibility of Sensitized Type 304 Stainless steel in High-Temperature Water," in Predictive Methods for Assessing Corrosion Damage to BWR Piping and PWR Steam Generators, NACE, H. Okada and R. Staehle, eds., pp. 90-92, 1978.

27. F. P. Ford and M. J. Povich, The Effect of Oxygen Temperature Combinations on the Stress Corrosion Susceptibility of Sensitized Type 304 Stainless Steel in High-Purity Water, Corrosion 35(12), 569-574 (1979).

28. K. Arioka, M. Hourai, S. Okamoto, and K. Onimura, The Effects of Boric Acid, Solution Temperature, and Sensitization on the SCC Behavior under Elevated Temperature Water, Corrosion 83, Anaheim, CA, April 18-22, 1983, Paper Number 135.

29. W. E. Ruther, W. K. Soppet, and T. F. Kassner, in Materials Science and Technology Division Light-Water Reactor Safety Research Program: Quarterly Progress Report, April-June 1983, NUREG/CR-3689 Vol. II, ANL-83-85 Vol. II (June 1984), pp. 31-60.

30. S. J. Hudak and R. P. Wei, Hydrogen Enhanced Crack Growth in 18Ni Maraging Steels, Met. Trans. 7A, 235-241 (1976).

31. P. S. Pao and R. P. Wei, Hydrogen Assisted Crack Growth in 18Ni (300) Maraging Steel, Scripta Met. 11, 515-520 (1977).

32. R. P. Gangloff and R. P. Wei, Gaseous Hydrogen Embrittlement of High Strength Steels, Met. Trans. 8A, 1043-1053 (1977).

33. D. P. Williams and H. G. Nelson, Embrittlement of 4130 Steel by Low-pressure Gaseous Hydrogen, Met. Trans. 1, 63-68 (1970).

34. H. G. Nelson, D. P. Williams, and A. S. Tetelman, Embrittlement of a Ferrous Alloy in a Partially Dissociated Hydrogen Environment, Met. Trans. 2, 953-959 (1971).

35. H. G. Nelson and D. P. Williams, "Quantitative Observations of Hydrogen-induced Slow Crack Growth in a Low Alloy Steel," in Stress Corrosion Cracking and Hydrogen Embrittlement of Iron-base Alloys, J. Hochmann, J. Slater, and R. W. Staehle, eds., NACE, pp. 390-404 (1978).

36. H. H. Johnson, "Hydrogen Brittleness in Hydrogen and Hydrogen-Oxygen Gas Mixtures," ibid., pp. 382-389 (1978).

37. G. W. Simmons, P. S. Pao, and R. P. Wei, Fracture Mechanics and Surface Chemistry Studies of Subcritical Crack Growth in AISI 4340 Steel, Met. Trans. 9A, 1147-1158 (1978).

38. M. Lu, P. S. Pao, N. H. Chan, K. Klier, and R. P. Wei, "Hydrogen Assisted Crack Growth in AISI 4340 Steel," in Hydrogen in Metals, Supplement to Trans. of the Japan Inst. of Metals 21, 449-452 (1980).

39. M. Lu, P. S. Pao, T. W. Weir, G. W. Simmons, and R. P. Wei, Rate Controlling Processes for Crack Growth in Hydrogen Sulfide for an AISI 4340 Steel, Met. Trans. 12A, 805-811 (1981).

40. M. Gao, M. Lu, and R. P. Wei, Crack Paths and Hydrogen-assisted Crack Growth Response in AISI 4340 Steel, Met. Trans. 15A, 735-746 (1984).

41. W. A. Van Der Sluys, Mechanisms of Environment Induced Subcritical Flaw Growth in AISI 4340 Steel, Eng. Fract. Mech. 1, 447-462 (1969).

42. J. D. Landes and R. P. Wei, The Kinetics of Subcritical Crack Growth under Sustained Loading, Int. Journ. of Fracture 9, 277-293 (1973).

43. F. P. Ford, "Stress Corrosion Cracking," in Corrosion Processes, R. N. Parkins, ed., Applied Science Publishers, New York, pp. 271-309 (1982).

II. LONG-TERM EMBRITTLEMENT OF CAST DUPLEX STAINLESS STEELS IN LWR SYSTEMS

Principal Investigators:
O. K. Chopra and H. M. Chung

A program is being conducted to investigate the significance of in-service embrittlement of cast duplex stainless steels nder light water reactor (LWR) operating conditions and to evaluate possible remedies to the embrittlement problem for existing and future plants. The existing data on embrittlement of duplex stainless steels and single-phase ferritic steels were reviewed to determine the critical parameters that control the embrittlement phenomenon and to establish the test matrices for microstructural studies and mechanical property measurements.[1,2] The scope of the program includes work to: (1) characterize and correlate the microstructure of in-service reactor components and laboratory-aged material with loss of fracture toughness and identify the mechanism of embrittlement; (2) determine the validity of laboratory-induced embrittlement data for predicting the toughness of component materials after long-term aging at reactor operating temperatures; (3) characterize the loss of fracture toughness in terms of fracture mechanics parameters in order to provide the data needed to assess the safety significance of embrittlement; and (4) provide additional understanding of the effects of key compositional and metallurgical variables on the kinetics and degree of embrittlement.

The relationship between aging time and temperature for onset of embrittlement will be determined by microstructural examination and measurements of hardness, Charpy impact strength, tensile strength, and J_{IC} fracture toughness. The kinetics and fracture toughness data generated in this program and from other sources will provide the technical basis to define the aging histories, chemical compositions, and metallurgical structures that lead to significant embrittlement of cast stainless steels under LWR operating conditions. Estimates of the degree of embrittlement will be compared with data obtained from examination of material from actual reactor service. Data pertaining to the effects of compositional and metallurgical variables on the embrittlement phenomenon will help to evaluate the possible remedies for existing and future plants.

A. Material Characterization and Mechanical Tests (O. K. Chopra)

Material was obtained from various experimental and commercial heats of CF-8, -8M, and -3 grades of cast stainless steel. Nineteen experimental heats were obtained in the form of keel blocks approximately 180 mm long, 120 mm high, and a thickness that tapered from 30 to 90 mm. The compositions of the heats were varied to provide different concentrations of nickel, chromium, carbon, and nitrogen in the material and ferrite contents in the range of 3 to 30%. Six large experimental heats, in the form of 76 mm thick slabs, were obtained for J_R-curve testing. Sections from four centrifugally cast pipes (grades CF-3, -8, and -8M), a static-cast pump impeller (grade CF-3), and a pump casing ring (grade CF-8) were also procured. The outer diameter and wall thickness of the cast pipes range from 0.6 to 0.9 m and 38.1 to 76.2 mm respectively.

Characterization of the various cast materials is in progress to determine the chemical composition, ferrite content, hardness, and grain structure. The castings were examined in the three orientations, i.e., axial, circumferential, and radial planes, as well as different locations, namely, material near the center and the inner and outer surfaces of the pipes, and top (Row 6) and bottom (Row 3) regions of the keel blocks. Orientation of the material had little or no effect on either hardness or the ferrite content and morphology. The ferrite morphology in the various cast materials was globular for ferrite contents of <5%, lacy for ferrite contents between 5 and 20%, and acicular for material with larger amounts of ferrite. The ferrite morphology in the keel blocks was different from that in the centrifugally cast pipes. For the same ferrite content, the islands of ferrite in the keel blocks were smaller and had a finer dispersion than in the pipe material.

The chemical composition, hardness, and ferrite content of the various heats of cast stainless steel are given in Table 2.1. The results show some differences in hardness and ferrite content for material from different locations in the castings. The ferrite content is lower and the hardness is slightly higher toward the inner surface of the various cast pipes. This behavior appears to be related to the nickel content in the material, i.e., the concentration of nickel is higher near the inner surface. Differences in

TABLE 2.1. Chemical Composition, Hardness, and Ferrite Content of the Various Heats of Cast Stainless Steel

Heat	Grade	Composition,[a] wt %							Location	Hardness, R_B	Ferrite Content,[b] %
		Mn	Si	Mo	Cr	Ni	N	C			
						Cast Keel Blocks					
58	CF-8	0.66	1.21	0.29	19.56	10.37	0.040	0.050	Row 3	76.0	3.6
									Row 6	78.2	2.1
57		0.69	1.24	0.28	18.45	8.94	0.041	0.060	Row 3	80.1	5.1
									Row 6	80.3	2.8
54		0.58	1.08	0.31	19.42	8.91	0.073	0.065	Row 3	82.6	1.2
									Row 6	83.9	2.3
53		0.70	1.28	0.35	19.62	8.86	0.045	0.070	Row 3	82.6	9.5
									Row 6	83.6	7.8
56[c]		0.60	1.16	0.30	19.33	8.93	0.031	0.060	Row 3	81.9	11.9
									Row 6	83.1	8.2
59		0.63	1.14	0.26	20.35	8.95	0.040	0.070	Row 3	83.5	14.2
									Row 6	82.8	12.7
61		0.70	1.20	0.27	20.54	8.59	0.063	0.060	Row 3	85.1	13.0
									Row 6	85.5	13.1
60[c]		0.71	1.01	0.26	21.02	8.07	0.050	0.070	Row 3	86.2	20.4
									Row 6	87.2	21.7
50	CF-3	0.57	1.26	0.28	17.63	8.84	0.064	0.019	Row 3	79.6	5.0
									Row 6	80.6	3.7
49		0.66	1.11	0.29	19.32	10.10	0.064	0.022	Row 3	76.1	8.0
									Row 6	77.2	6.3
48		0.67	1.21	0.26	19.42	9.90	0.071	0.016	Row 3	77.6	8.9
									Row 6	78.6	8.5
47		0.65	1.23	0.45	19.67	10.04	0.027	0.018	Row 3	79.0	16.5
									Row 6	80.3	16.2
52		0.63	1.04	0.31	19.51	9.07	0.049	0.021	Row 3	81.4	10.3
									Row 6	81.8	16.7
51[c]		0.66	1.06	0.28	20.36	8.69	0.048	0.023	Row 3	83.7	18.0
									Row 6	83.9	18.0
62	CF-8M	0.84	0.64	2.46	18.38	11.35	0.030	0.070	Row 3	78.2	6.3
									Row 6	78.0	2.6
63		0.69	0.75	2.52	19.39	11.22	0.030	0.050	Row 3	81.0	10.9
									Row 6	82.1	10.0

TABLE 2.1. (Contd.)

Heat	Grade	Composition,[a] wt % Mn	Si	Mo	Cr	Ni	N	C	Location	Hardness, R_B	Ferrite Content,[b] %
66[c]	CF-8M	0.71	0.60	2.36	19.41	9.13	0.030	0.060	Row 3	84.6	19.2
									Row 6	85.8	20.5
65		0.66	0.63	2.53	20.95	9.39	0.060	0.060	Row 3	88.4	21.4
									Row 6	89.5	25.4
64[c]		0.70	0.71	2.41	20.87	9.01	0.030	0.050	Row 3	89.7	27.5
									Row 6	89.7	29.3
					Cast Components						
C1	CF-8	1.22	1.19	0.64	19.10	9.32	0.041	0.036	O.D.	78.3	2.3
					18.89	9.42			I.D.	80.6	1.7
P1		0.56	1.07	0.04	20.38	8.00	0.053	0.032	O.D.	84.5	27.6
					20.60	8.20			I.D.	85.3	19.5
P3	CF-3	1.04	0.86	0.01	18.93	8.33	0.159	0.020	O.D.	80.6	2.5
					18.85	8.56			I.D.	83.7	0.9
P2		0.72	0.92	0.16	20.20	9.24	0.041	0.020	O.D.	82.4	15.9
					20.20	9.51			I.D.	85.1	13.2
I		0.46	0.80	0.44	20.08	8.50	0.030	0.016	Vane 3	81.1	20.2
					20.20	0.80			Vane 1	82.2	14.3
					20.34	8.64			Shroud	78.1	18.9
					20.20	8.84			Hub	81.0	19.1
P4	CF-8M	1.07	1.02	2.06	19.63	10.00	0.153	0.039	O.D.	83.0	11.1
					19.65	9.99			I.D.	83.2	9.8

[a]Chemical composition of the keel blocks supplied by the vendor.
[b]Ferrite content measured by Ferrite Scope, Auto Test FE, Probe Type FSP-1.
[c]Chemical composition of the large experimental heats.

hardness and ferrite content are also observed for material from different locations in the static-cast keel blocks. Hardness is always higher toward the top of the keel blocks. However, variations in the ferrite content depend on the Cr_{eq}/Ni_{eq} ratio in the material; the ferrite content toward the top of the casting is lower for material with Cr_{eq}/Ni_{eq} <1.13 and higher for material with Cr_{eq}/Ni_{eq} >1.13. In general, the hardness of the cast material increases with an increase in ferrite content. For the same ferrite content, the hardness of CF-8 and -8M material is comparable while the hardness of CF-3 material is lower. An increase in nitrogen content increases the hardness of all grades of cast stainless steel.

The ferrite content and the different structures present in the four pipe sections and pump casting ring are given in Table 2.2. The grain structures

TABLE 2.2. Ferrite Content and Grain Structure of Various Cast Stainless Steel Pipes

Heat	OD, m	Wall, mm	Process	Grade	Ferrite Content,[a] % OD	Ferrite Content,[a] % ID	Grain Structure
C1	0.60	57.1	Static	CF-8	2.3	1.7	Banded, columnar/equiaxed radial to axial growth near ends
P1	0.89	63.5	Centr.	CF-8	27.6	19.5	Equiaxed across thickness
P3	0.58	51.6	Centr.	CF-3	2.5	0.9	Banded, radially oriented columnar one equiaxed band (~4 mm deep) near ID
P2	0.93	73.0	Centr.	CF-3	15.9	13.2	Equiaxed across thickness
P4	0.58	31.8	Centr.	CF-8M	11.1	9.8	Radially oriented columnar

[a]Ferrite content measured by Ferrite Scope, Auto Test FE, Probe Type FSP-1.

were examined in the axial, circumferential, and radial planes. Two castings, P1 and P2, contained equiaxed grains across the entire thickness of the pipe. The grain size and distribution were not significantly different in the three orientations. The equiaxed grains were probably produced intentionally by a low pouring temperature or by shear between the liquid and solid. The shear could cause dendrite arms to break off and disperse in the liquid-solid region. These castings are expected to exhibit uniform properties in all directions.

The other two centrifugally cast pipes, P3 and P4, showed radially oriented columnar grains. Pipe section P3 also contained a band of small equiaxed grains near the ID. This band was relatively thin, i.e., ~4-mm deep, and probably formed accidentally. The columnar grain castings are expected to have uniform properties in the axial and circumferential directions. The static-cast pump casing ring showed a mixed structure of columnar and equiaxed grains. A change from radial to axial growth of the columnar grains was also observed. The equiaxed and columnar grain structures in the cast pipes P1, P2, and P3 are shown in Fig. 2.1.

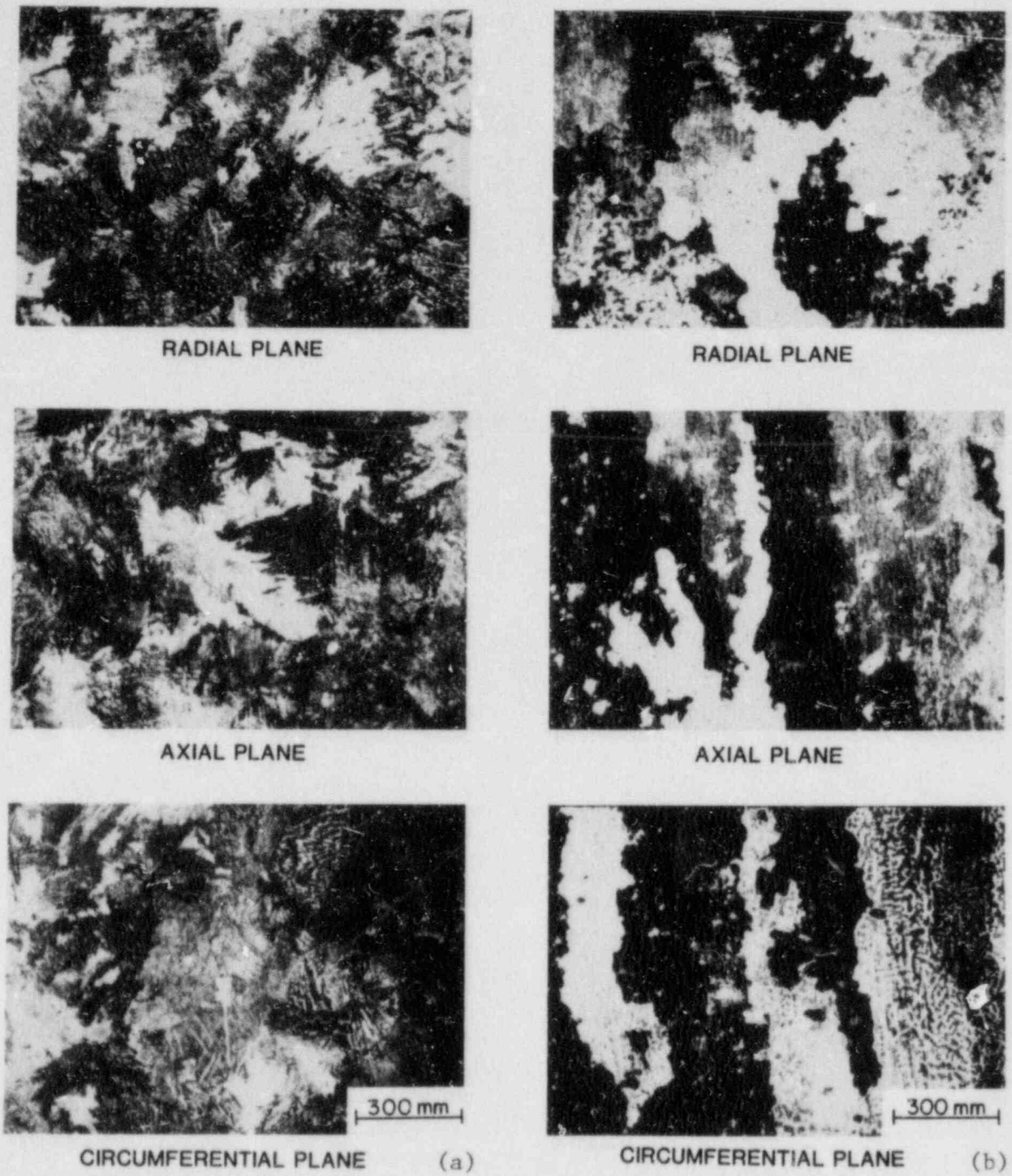

Fig. 2.1. Microstructures along the Three Orientations of Centrifugally Cast Stainless Steel Pipe. (a) and (b) CF-3 and (c) CF-8. The planes of the micrographs are designated by the direction normal to plane, i.e., the radial-circumferential plane of the pipe is designated as axial.

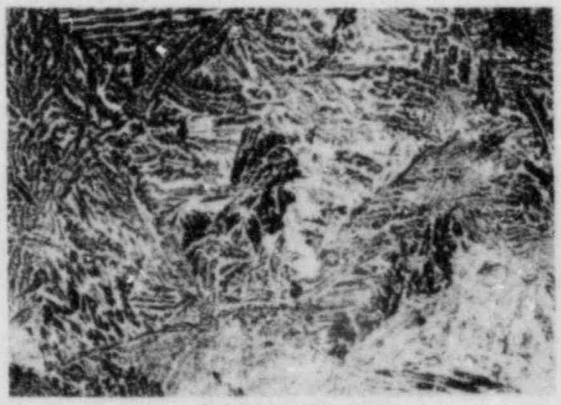

RADIAL PLANE

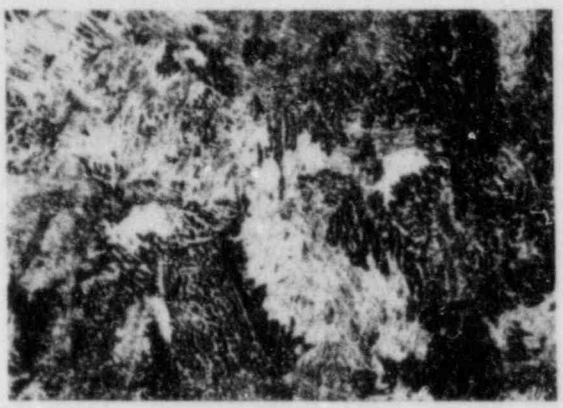

AXIAL PLANE

CIRCUMFERENTIAL PLANE (c)

Fig. 2.1. (Contd.)

Charpy impact specimen blanks were prepared from keel blocks of the experimental heats and material from the six reactor components. Blanks for the 1-T compact tension specimens were obtained from sections of two centrifugally cast pipes and the static-cast pump casing ring, pump impeller, and the six large experimental heats. Blanks for 2-T compact tension specimens were also prepared from three of the large experimental heats. The specimens are being aged at 450, 400, 350, 320, and 290°C. The aging times range from 100 to 50,000 h. Charpy impact tests are in progress on the unaged material and material that was aged up to 1000 h at the different temperatures.

B. Microstructural Characterization of the Aged Material (H. M. Chung)

Results of microstructural characterization by transmission electron microscopy (TEM) of several ferritic alloys and cast duplex stainless steels (aged at 300-475°C) have been reported previously.[3] A total of five different types of precipitates have been identified. The α' phase was observed in all alloys aged at 475°C, i.e., 26Cr-1Mo and 29Cr-4Mo-2Ni ferritic steels and cast duplex stainless steel CF-8, Heat B. However, the α' phase was not observed in two heats of cast duplex stainless steel annealed up to eight years at 300-400°C at the Georg Fischer Company of Switzerland. Since long-term aging at the lower temperatures is more prototypic of a reactor operating conditions, TEM characterization during this reporting period concentrated on the materials obtained from the Georg Fischer Company. SEM characterization of the fracture surfaces of specimens, which were impact tested at room temperature, was also initiated during this reporting period. Information from the SEM fractographic characterization will be correlated with results of the TEM investigation and Charpy impact tests.

1. Characterization of Precipitates in Aged Cast Duplex Stainless Steel

The five types of precipitates observed in the ferrite phase of the steels can be summarized as follows:

(1) α' - chromium-rich phase giving rise to mottled bright-field images but producing no detectable changes in the diffraction patterns;

(2) Type P - platelet precipitate producing strong strain-field contrast in bright-field images and giving rise to streaks of the ferrite diffraction spots;

(3) Type M - $M_{23}C_6$-like precipitate rich in Ni and Si and exhibiting a distinct diffraction pattern that contains superlattice spots;

(4) Type X - precipitates observed on dislocations giving rise to very weak and streaked reflections as a result of small volume fraction and very fine size;

(5) Type ML - precipitates that are observed in association with Type M, coating the Type M precipitates and dislocations.

Table 2.3 summarizes the aging conditions and materials in which five types of precipitates were observed. For the cast duplex stainless steels aged at the lower temperatures, the Type M, X, or ML precipitates rather than the α' phase are likely to influence the toughness and fracture behavior of the material.

TABLE 2.3. Summary of Types of Precipitates Observed in Ferritic Alloys and Cast Duplex Stainless Steel After Long-Term Aging at 300-475°C

Alloy	Aging Conditions		Precipitate Phases				
	Temp., °C	Time, h	α'	Type P	Type M	Type X	Type ML
26Cr-1Mo ferritic	475	1,000	Yes				
	400	1,000	No	No			
29Cr-4Mo-2Ni ferritic	475	1,000	Yes	Yes			
	400	1,000	No	Yes			
Cast duplex stainless steel CF-8, Heat B	475	1,000	Yes		Yes		
	400	1,000	No	No	No	No	No
Cast duplex stainless steel CF-8, Heat 280	400	66,650	No		Yes	Yes	
	400	10,000	No		No	Yes	
	300	70,000	No		No	Yes	
Cast duplex stainless steel CF-8, Heat 278	400	70,000	No		Yes		
	350	70,000	No				
	300	70,000	No		Yes		
Cast Duplex Stainless Steel CF-8M, Heat 286	400	10,000	No		Yes		Yes

Examination of the cast duplex stainless steel CF-8 material (Heat 280, ferrite content ~40%), aged at 400°C for 66,650 h, showed another type of precipitate, designated tentatively as Type S. The presence of the Type S phase could be detected only through a very careful examination of the diffraction patterns. An example is shown in Fig. 2.2. In Fig. 2.2(A), a bright-field image shows an area containing precipitates. The corresponding selected area diffraction (SAD) pattern of Fig. 2.2(B) indicates that the precipitates were predominantly Type M ($M_{23}C_6$-like precipitate). However, extra reflections indicating the presence of another phase are visible in the circled regions of Fig. 2.2(B). The reflections are extremely weak, indicating a small volume fraction, and could barely be detected on the microscope screen. As a result, no dark-field images could be obtained. The weak spots could be detected only from the developed negatives of the SAD pattern. The specks are very sharp compared to reflections from the matrix or Type M phases, indicating that the reflecting sphere intersects thin, flattened needle-like reciprocal lattice rods.

Figure 2.3 shows another example of the Type S reflections that are barely visible in the SAD pattern. Similar reflections were also observed from specimens of cast duplex stainless steel CF-8 (Heat 278, ferrite content 15%), aged at 300°C for 70,000 h. The SAD pattern of Fig. 2.3(B) shows, in addition to the matrix and Type S phase reflections, diffuse streaked reflections (not Kikuchi bands) indicating the presence of another phase. The positions of the diffuse streaked reflections are virtually the same as those of the ferrite matrix. An examination of the dark-field image of Fig. 2.3(C), obtained from the arrowed reflections containing a diffuse reflection and $(\bar{1}\bar{1}2)_\alpha$, shows precipitate particles of $\lesssim$10 nm in size on and away from dislocations.

2. SEM Fractographic Characteristics

Fracture characteristics of the cast duplex stainless steel CF-8, Heat 278, obtained from the Georg Fischer Company of Switzerland after aging for 10,000 h at 400 and 300°C, were examined by scanning electron microscopy.

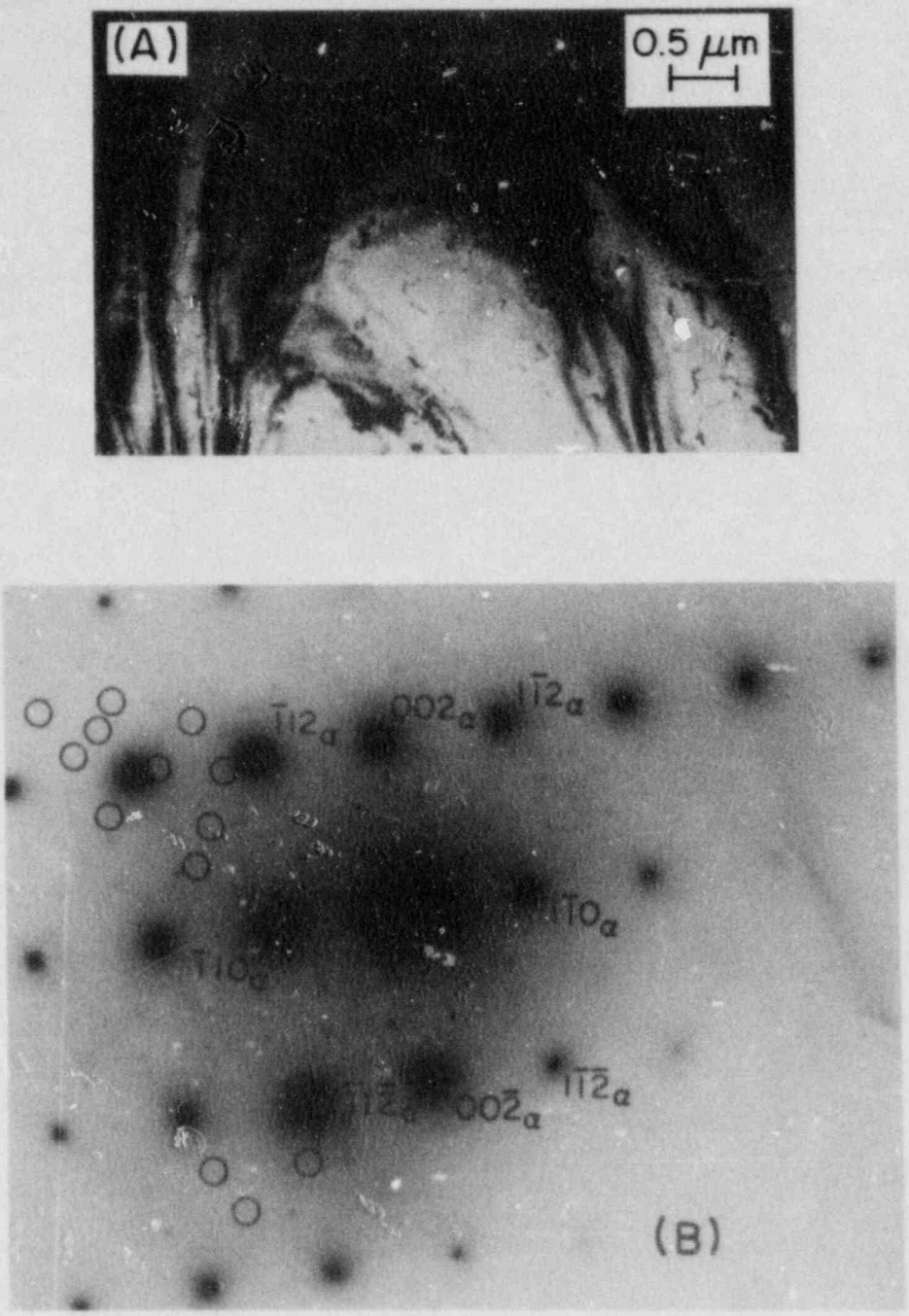

Fig. 2.2. TEM Micrographs of Cast Duplex Stainless Steel CF-8 (Heat 280) Aged at 400°C for 66,650 h. (A) Bright-field morphology showing precipitates; (B) selected-area diffraction pattern showing reflections from Type M ($M_{23}C_6$-like) precipitates. Extremely weak reflections from another unknown precipitate are visible in the circled areas.

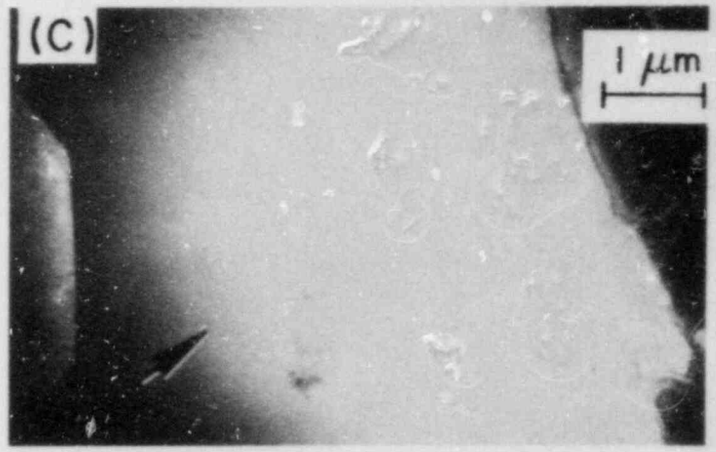

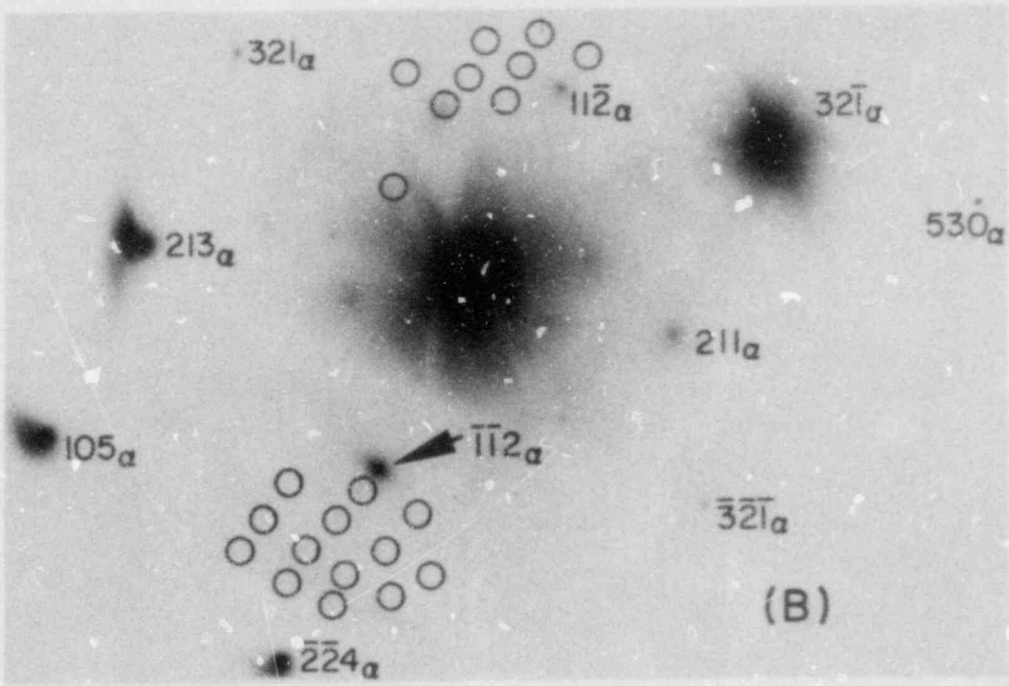

Fig. 2.3.

Micrographs Similar to Those of Fig. 2.2. (A) Bright-field image of an area containing precipitates; (B) SAD pattern showing diffuse and streaked reflections from one type of precipitate and extremely weak reflections from another type of unknown precipitate in the circled areas; (C) dark-field image produced from the arrowed reflection of (B) showing fine precipitates on and away from dislocations.

Fracture surface morphologies of the material, aged at 400°C and fractured at room temperature by Charpy impact loading, are shown in Fig. 2.4. The overall fracture surface is shown in the low-magnification micrograph of Fig. 2.4(A). More detailed examination of Fig. 2.4(A) at higher magnification showed that approximately 20-25% of the fracture surface was composed of brittle cleavage and the remainder exhibited a ductile dimple morphology [Fig. 2.4(B)]. A higher magnification of the cleavage morphology region [Fig. 2.4(C)] reveals river patterns characteristic of brittle fracture.

In comparison to the specimen aged at 400°C for 10,000 h, the extent of the cleavage feature in the fracture surface of the specimen aged at 300°C for a comparable period was minimal. The overall fracture surface and magnified regions of the specimen are shown in Fig. 2.5(A)-(C). A localized area of cleavage morphology is shown in the encircled regions of Fig. 2.5(C).

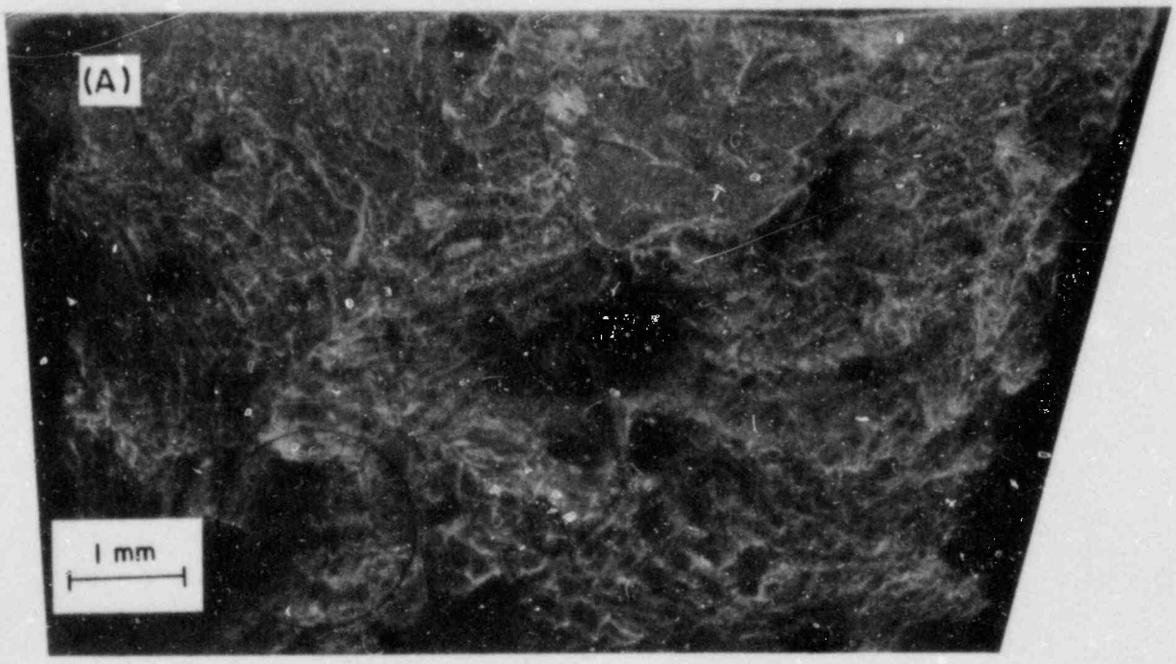

Fig. 2.4. SEM Fracture Surface Morphologies of Cast Duplex Stainless Steel CF-8 (Heat 278) Aged at 400°C for 10,000 h. (A) Overall fracture surface; (B) higher magnification of the encircled area of (A) showing mixture of cleavage and dimple morphologies; (C) higher magnification of the encircled area of (B) showing cleavage.

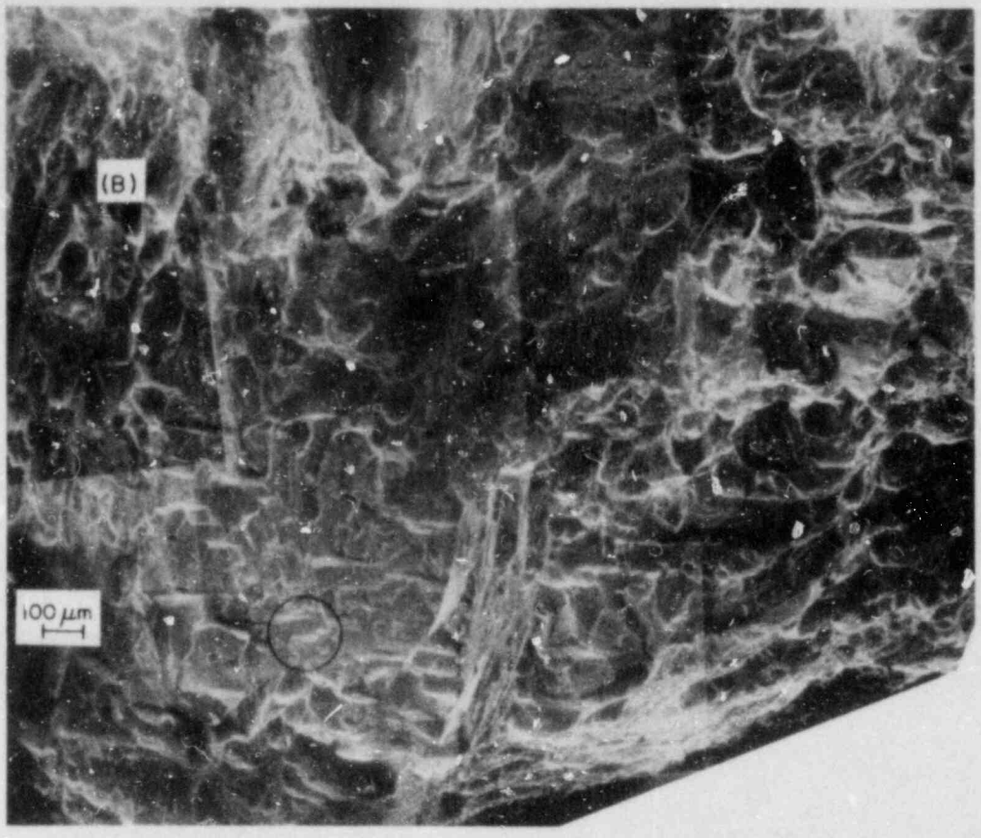

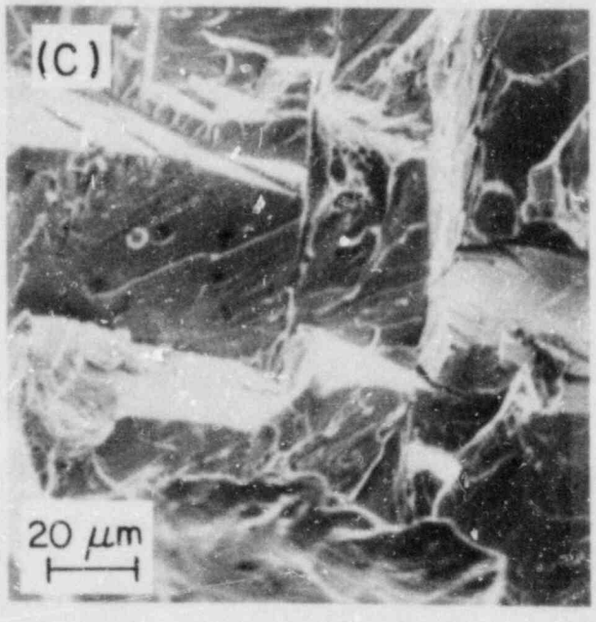

Fig. 2.4. (Contd.)

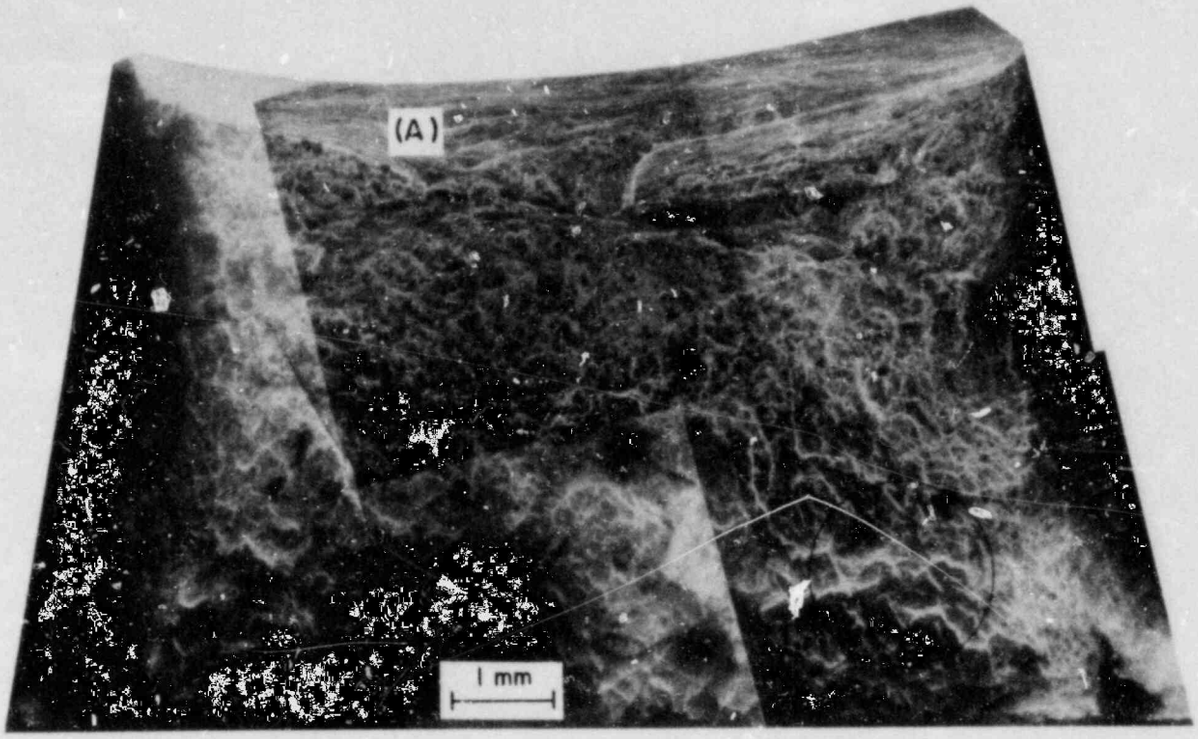

Fig. 2.5. SEM Fractographs of Cast Duplex Stainless Steel CF-8 (Heat 278) Aged at 300°C for 10,000 h. (A) Overall fracture surface; (B) higher magnification of the encircled area of (A); (C) higher magnification of the encircled area of (B) showing limited areas of cleavage in the encircled regions.

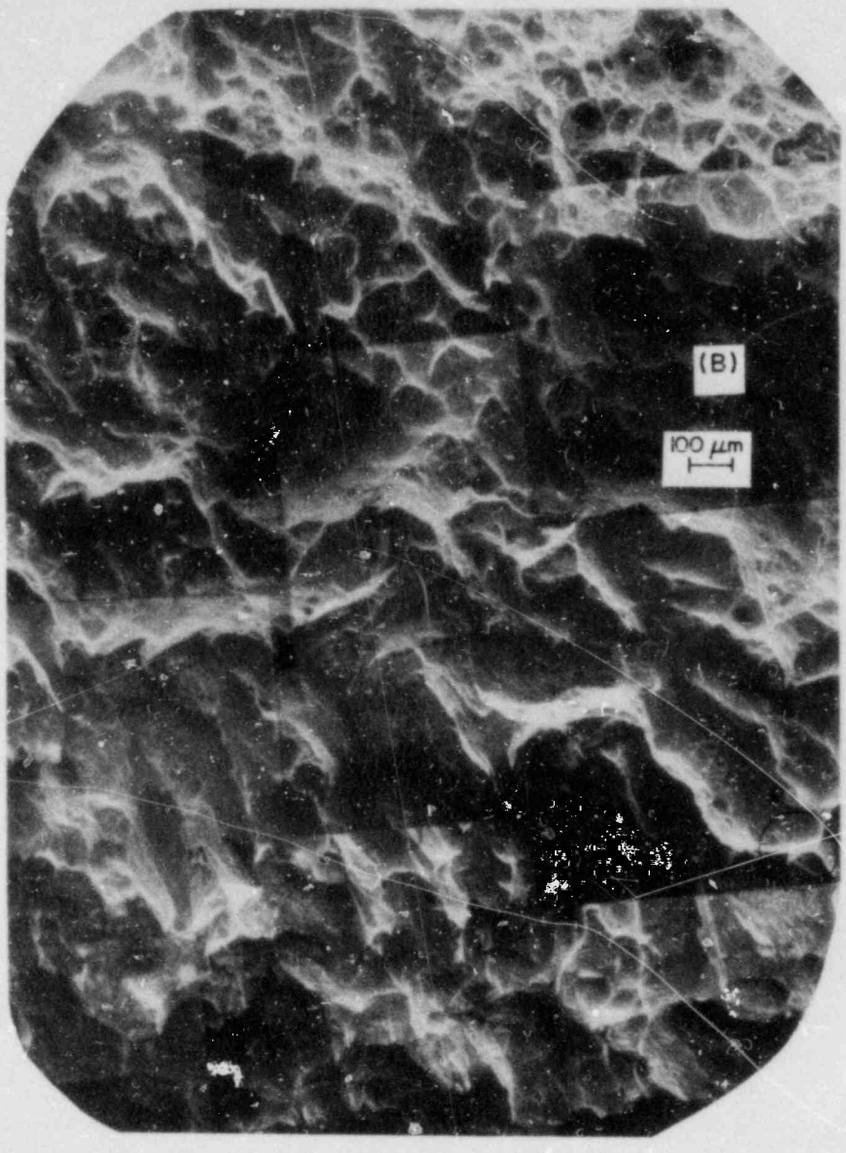

Fig. 2.5. (Contd.)

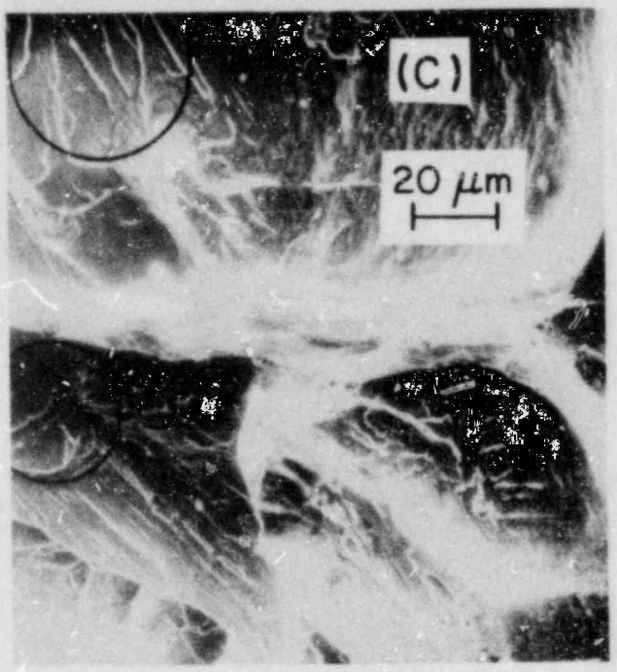

Fig. 2.5. (Contd.)

C. References for Chapter II

1. O. K. Chopra et al., in Materials Science and Technology Division Light-Water-Reactor Safety Research Program: Quarterly Progress Report, October-December 1982, NUREG/CR-2970 Vol. IV, ANL-82-41 Vol. IV (November 1983), pp. 99-110.

2. O. K. Chopra and G. Ayrault, Long-Term Embrittlement of Cast Duplex Stainless Steels in LWR Systems: Annual Report, October 1982-September 1983, NUREG/CR-3857, ANL-84-44 (July 1984).

3. O. K. Chopra and G. Ayrault, "Aging Degradation of Cast Stainless Steel: Status and Program," Proc. Eleventh Water Reactor Safety Research Information Meeting, October 24-28, 1983, Gaithersburg, MD, NUREG/CR-0048, Vol. 4, pp. 152-169.

4. A. Trautwein and W. Gysel, (a) Influence of Long Time Aging of CF-8 and CF-8M Cast Steel at Temperatures Between 300 and 500 Deg. C on the Impact Toughness and the Structure Properties, Spectrum, Technische Mitteilungen aus dem GF+Konzern, No. 5, May 1981; Stainless Steel Castings, eds. V. G. Behal and A. S. Melilli, ASTM STP 756 (1982), p. 165; (b) figure in EPRI NP-2705-SR (October 1982), p. 3.18.

III. NONDESTRUCTIVE EVALUATION AND LEAK DETECTION

Principal Investigator:
D. S. Kupperman

No currently available, single leak-detection method combines optimal leakage detection sensitivity, leak-locating ability, and leakage measurement accuracy.[1] For example, while quantitative leakage determination is possible with condensate flow monitors, sump monitors, and primary coolant inventory balance, these methods are not adequate for locating leaks and are not necessarily sensitive enough to meet regulatory guide goals.

Technology is available to improve leak detection capability at specific sites by use of acoustic monitoring or moisture-sensitive tape. However, current acoustic monitoring techniques provide no source discrimination (e.g., to distinguish between leaks from pipe cracks and valves) and no flow-rate information (a small leak may saturate the system). Moisture-sensitive tape provides neither quantitative leak-rate information nor specific location information other than the location of the tape; moreover, its usefulness with "soft" insulation needs to be demonstrated. Leak detection techniques need further improvement to permit: (1) identifying leak sources through location information and leak characterization, to eliminate false calls; (2) quantifying and monitoring leak rates; and (3) minimizing the number of installed transducers in a "complete" system through increased sensitivity.

Many cracks are missed during ultrasonic in-service inspection (ISI) and are detected only because of leakage. The present ASME Code Sections V and XI pertaining to ultrasonic testing procedures for ferritic weldments do not appear to be adequate for the detection and evaluation of IGSCC in austenitic stainless steel (SS) piping. While the probability of detecting IGSCC under field conditions has increased since the issuance of NRC IE Bulletins 83-02 and 82-03, the detection of intergranular cracks is still difficult. Intergranular cracks that can be detected by conventional ultrasonic methods under laboratory conditions may be missed during a field examination by even the most skilled operator.

A. Objectives

The objectives of this program for leak detection are to (a) develop a facility to quantitatively evaluate acoustic leak detection (ALD) systems, (b) assess the effectiveness and reliability of ALD techniques, (c) evaluate a prototype ALD system, (d) establish sensitivity, reliability, and decision making capability of a prototype system through laboratory testing, and (e) assess the effectiveness of field-implementable ALD systems. The program will establish whether meaningful quantitative data on leak rates and location can be obtained from acoustic signatures of leaks due to cracks (IGSCC and fatigue) in low- and high-pressure lines, and whether these can be distinguished from other types of leaks. It will also establish calibration procedures for acoustic data acquisition and show whether advanced signal processing can be employed to enhance the adequacy of ALD schemes.

The program objectives for ultrasonic NDE are to (a) assess the capability of a multielement skew-angle probe to distinguish intergranular cracks from geometrical reflectors, (b) assess methods for characterizing the microstructure of cast stainless steel to determine ISI reliability, and (c) evaluate new ultrasonic inspection problems (i.e., weld overlays).

B. Ultrasonic NDE for Cast Stainless Steel (D. S. Kupperman, T. N. Claytor, and R. N. Lanham)

It is well known that the coarse grain size and elastic anisotropy of cast stainless steel (CSS) make ultrasonic inspection difficult. Although the ASME code requires that cast stainless piping be inspected, it has not been possible to demonstrate that current inspection techniques are adequate. For the near term, improvements that may increase the reliability of ultrasonic inspection include: (a) the development of methods to establish the microstructure of the material (to help optimize the inspection technique), (b) calibration standards that are more representative of the material to be inspected, and (c) training that uses CSS samples with cracks. For the long term, it will be necessary to establish (a) the variability of the microstructure of CSS, (b) the effect of microstructure on inspection reliability, (c) the improvements possible with electronics, techniques, and transducers

designed specifically for CSS, e.g., focused transducers and lower frequencies than those used conventionally, and (d) qualification of requirements for CSS inspections. Recent work carried out at ANL to address some of these points is presented in this report.

1. Variation of Sound Velocity with Microstructure

The variation of the velocity of sound with propagation direction has been discussed in a previous report.[2] When the material is isotropic, the variation in velocity is small (<2%), whereas for anisotropic material (columnar grains) the variation in velocity can be as large as 100% for shear waves. The magnitude of the velocity of sound may also be used as a measure of the degree of anisotropy and thus an indicator of microstructure. Relatively low longitudinal velocities indicate a columnar grain structure, high velocities indicate an equiaxed (isotropic) structure. Intermediate values indicate the presence of both microstructures. The validity of this concept has been demonstrated on CSS samples with different microstructures. Figure 3.1 shows the longitudinal velocities of sound for seven samples of a 28-in. pipe (400 x 180 x 60 mm thick) provided by PNL and eighteen samples of a comparable large-diameter pipe provided by Westinghouse. The PNL samples were fabricated from a weldment in which material with a well-defined equiaxed grain structure was joined to material with a well-defined columnar grain structure. The Westinghouse samples are also made from a weldment. These specimens, however, were machined flat and have a coarse and poorly defined grain structure. The velocity of sound was measured by standard pulse-echo methods with a 37-mm-dia, 1-MHz transducer. Echo transit times were measured with a Tektronix oscilloscope. In all cases the longitudinal waves propagate in a radial direction through the pipe wall. As can be seen in Fig. 3.1, the equiaxed and columnar sides of the PNL samples can be easily distinguished by measurements of the longitudinal sound velocity. The sample-to-sample variation is relatively small. The Westinghouse samples, however, show large variations in sound velocity from sample to sample as well as within a sample (two velocities were measured in each sample). The wide range of the values is indicative of large variations in the microstructure of these samples. The

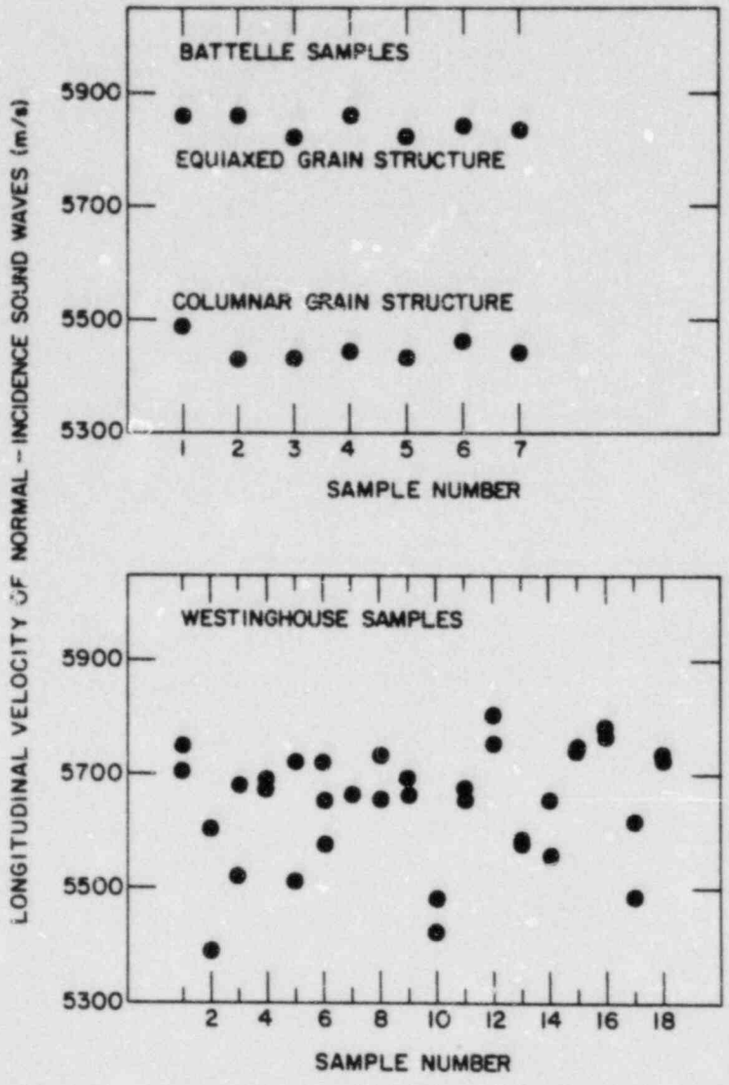

Fig. 3.1. Variation of Longitudinal Velocity of Sound in Equiaxed, Columnar, and Undefined Coarse Grained (Westinghouse) Cast Stainless Steel Large-diameter Pipe Sections. Sample wall thicknesses are nominally 60 mm. 1-MHz, longitudinal waves in a pulse-echo mode were propagated normal to the pipe outer diameter surface.

complex microstructure could cause significant, unpredictable distortion of the ultrasonic waves used to interrogate the material and lead to an unreliable examination.

Velocity of sound measurements on CSS were also acquired during a visit to the Commonwealth Edison Byron Station. A CSS reference block and two CSS elbows were examined. The longitudinal velocity of sound was measured in the reference block without any significant difficulty, but measurements in the cast elbows were limited by attenuation and an absence of reliable wall-thickness data.

On the cast portion of the 7.6 mm thick reference block the velocity of sound for longitudinal waves was measured at 11 points covering about 0.01 m^2. The measurements are shown in Fig. 3.2. The average velocity was 6090 m/s with a variation of about ±1.5% due to the microstructure. The relatively high velocity of sound strongly suggests that the calibration block has an equiaxed grain structure that may be significantly different from the material found in the plant piping and elbows. As a check on the accuracy of the measurement, the carbon steel portion of the reference block was also examined. A sound velocity of 5890 m/s was obtained, which is consistent with previous data for this material.

Two elbows in the plant were examined. The steam generator and pipe sides of the loop 4 crossover were selected for this test. The area adjacent to the elbow-to-pipe weld was ground smooth. The remaining portion of the elbow was rough and ultrasonic waves could not propagate efficiently into this part of the elbow. Ultrasonic backwall echoes could be detected in most but not all of the smooth areas. On the pump side where the elbow and pipe appear to have the same wall thickness, estimates of the velocity of sound were made using the wall thickness stamped on the pipe section. Although no backwall echo was detected on the top of the elbow, the velocity of sound could be measured elsewhere. The velocity varied from 5200 to 5860 m/s away from the top of the elbow as shown in Fig. 3.2. This suggests that the microstructure of the elbow was quite different from the reference block.

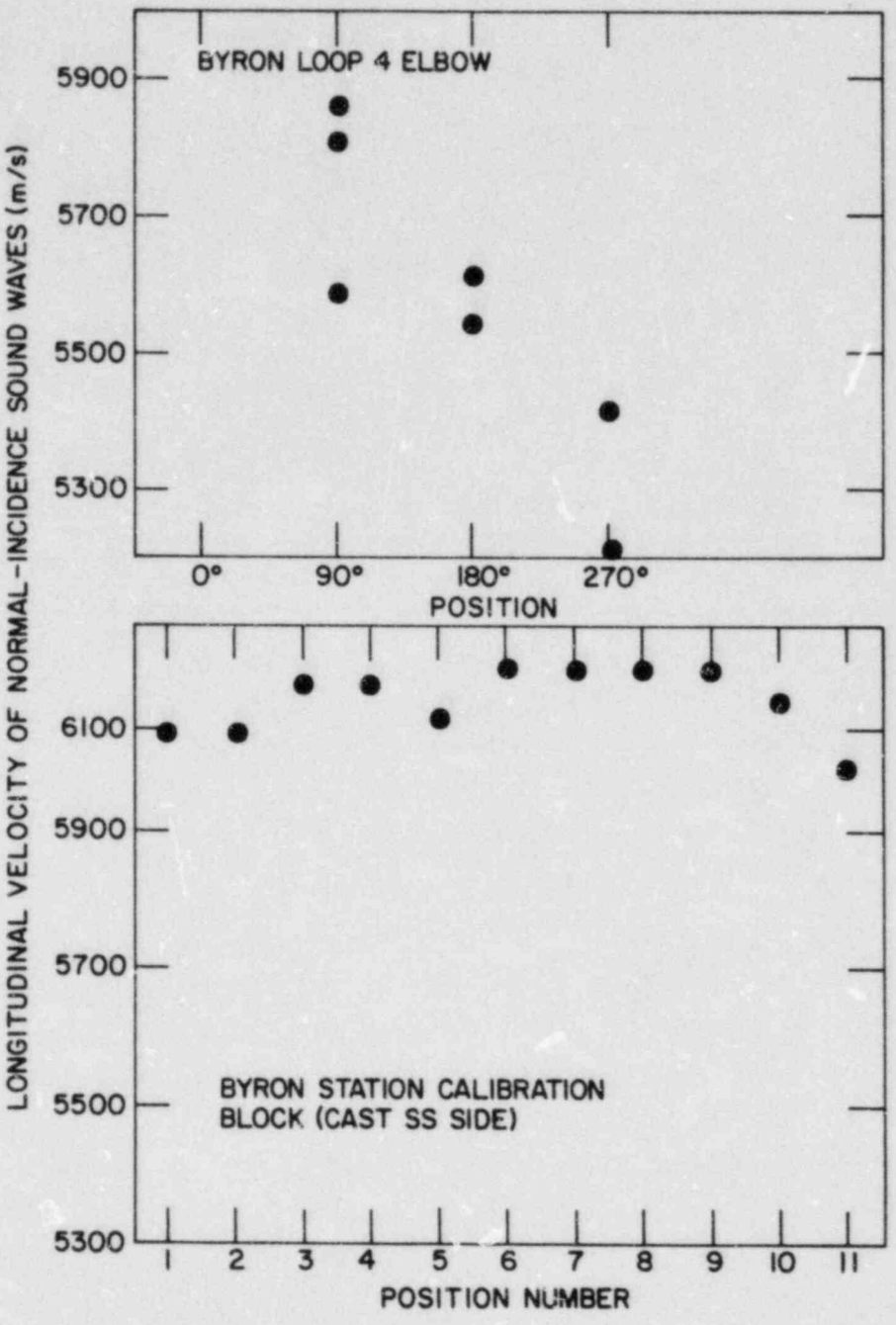

Fig. 3.2. Variation of Longitudinal Velocity of Sound with Position in a CSS Calibration Block and in a Commonwealth Edison Byron Station Loop 4 Elbow. 1-MHz, normal-incidence longitudinal waves were used.

On the steam-generator side the wall thickness could not be estimated because of the elbow geometry. Although absolute velocities were not determined, it appeared that the velocity varied by about 5%. The velocity of sound in the straight (wrought) section was found to be 5760 m/s, which is consistent with previous measurements on stainless steel.

Attempts were also made to propagate 1-MHz, 45° longitudinal waves in the cast material with two transducers in a pitch-catch mode. No backwall echo was detected in the reference block, which is consistent with the conclusion that the material is equiaxed. No echo signal could be detected on the pump-side elbow, but echoes were present on the steam-generator side elbow. The two elbows have distinctly different wave propagation characteristics. However, in both cases there was considerable ultrasonic noise. The results obtained by ANL are consistent with the suppositions that ultrasonic inspections of CSS are very unreliable at best, that ultrasonic-wave propagation characteristics vary considerably from component to component and within an individual component, and that reference-block material may not be representative of the material to be inspected.

2. Microstructure and Deviation of Ultrasonic Beams

In an elastically isotropic material (equiaxed grains) the energy in an ultrasonic beam propagates in the direction of the wavefront normal, as expected. However, in elastically anisotropic material (columnar grain structure) the direction of propagation of ultrasonic energy in a beam can be different from the direction of wavefront normal. Because of this phenomenon, it may be possible to distinguish columnar from equiaxed grain structures nondestructively. In CSS with equiaxed grains, a 45° longitudinal wave will propagate as expected. Thus, as shown in Fig. 3.3, for a specimen 60 mm thick with the transducer placed on the top surface, the maximum acoustic signal at the bottom will be detected ~60 mm from the point directly opposite the beam entry point. For a similar specimen with columnar grains, the energy in the beam deviates from the expected 45° path and is directed nearly downward to the surface of the specimen (see Fig. 3.3). The maximum signal will be detected at a point almost opposite to the beam entry point (~16 mm). The beam in the equiaxed material will be reflected to a point ~120 mm from the

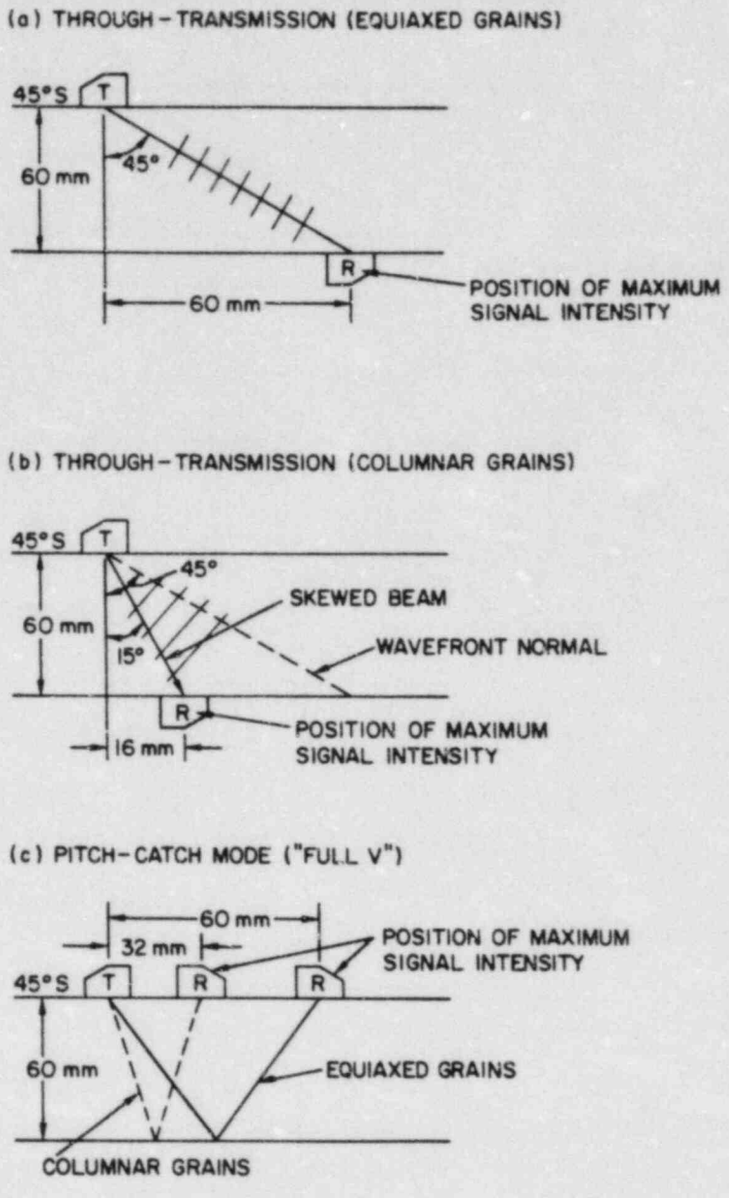

Fig. 3.3. Schematic Representation of the Path of Ultrasonic Energy in Cast Stainless Steel with Equiaxed and Columnar Grain Structures. (a) Transmit from outer surface and receive at inner (equiaxed grains), (b) transmit from outer surface and receive at inner (columnar grains), and (c) transmit and receive at outer surface. Expected position for maximum received signals is shown in (a) and (b).

transmitting transducer (following the expected "full V" path), while the maximum beam intensity in the columnar material will be found much closer to the transmitting transducer (~32 mm away). If the angular deviation of longitudinal waves as a function of propagation angle is known, the point of maximum signal intensity for the pitch-catch configuration of Fig. 3.3 can be calculated from Snell's law:

$$\frac{\sin \theta_w}{V_w} = \frac{\sin \theta_{CSS}}{V_{CSS}(\theta)} \text{ , where } \frac{\sin \theta_w}{V_w} = 0.22. \qquad (3.1)$$

θ_w and V_w are the angle of incidence and velocity of sound in the wedge, and θ_{CSS} and V_{CSS} are the angle of refraction and longitudinal velocity of sound in the cast stainless steel.

Velocity-of-sound data for CSS is found in Ref. 2. The angular dependence of the velocity of sound must be known in order to calculate the angle of refraction. Based on velocity measurements in two different directions in the columnar grain stainless steel the orthotropic elastic constants were calculated using the Christoffel equations. These constants can then be used to calculate the velocity as a function of the angle of incidence, and hence, to calculate the angle of refraction from Eq. (1). For the wedge which was used, the calculated angles of refraction are 36° for the columnar grain stainless steel and 45° for equiaxed material. For this propagation direction in the columnar material, the energy of the beam propagates in a direction inclined 15° to the surface normal.[3] The angle between the velocity vector and the direction of maximum energy propagation is 21° (i.e., 36° - 15°). The reflected wave should have a maximum signal intensity at the transmitting surface ~32 mm from the transmitting probe in a sample 60 mm thick. This is much less than the calculated separation distance of ~127 mm for the equiaxed specimen (the angle of refraction was actually 47° leading to a separation distance slightly larger than the expected value of 120 mm for a 45° angle).

Experiments were carried out to verify this prediction. Two 1-MHz nominally 45° shear-wave transducers (1-in. dia) were placed on the pipe section outer-diameter surface. The experimentally determined value of 42 mm in the columnar grain material compares favorably to the predicted value of

32 mm. The predicted separation in the equiaxed grain material of 127 mm is also reasonably close to the experimentally determined value of 105 mm. Table 3.1 summarizes these results.

TABLE 3.1. Transducer Pair Separation for Maximum Received Signal Using 45° Shear Waves in Pitch-Catch "Full V" Configuration

Material	Wall Thickness, mm	Grain Structure	Predicted Value, mm	Measured Value (0.5 MHz), mm
Cast SS	60	columnar	32	42
Cast SS	60	equiaxed	127	105

Another way to observe the beam deviation phenomenon is to map the beam profile. Figure 3.4 compares the distortion of the 45° shear wave at the pipe inner surface for the columnar and equiaxed materials. The beam deviation phenomenon as well as the distortion of the beam in general is clearly evident in these beam profiles. Note that the amplitudes are normalized and that the apparent attenuation in the columnar material at 1 MHz is about 0.1 dB/mm less than in the equiaxed material. A 45°, 1-MHz, 25-mm-dia transducer was used to transmit the shear wave while a 6 mm-dia transducer was used to receive it. This method of characterizing microstructure appears to be more sensitive than using the velocity of sound which is more dependent on accurate wall-thickness measurements. Other samples of CSS are being studied to determine if microstructures that are not well defined can be characterized by ultrasonic techniques.

C. Distinguishing Intergranular Cracks from Geometrical Reflectors

As is well known, one of the main obstacles to reliable ultrasonic detection of IGSCC is the difficulty of distinguishing cracks from geometric reflectors. Because of the irregular and generally branched character of intergranular cracks, they may produce a broader scattering pattern than a geometrical reflector. It may be possible to use this characteristic to distinguish cracks from geometric reflectors.

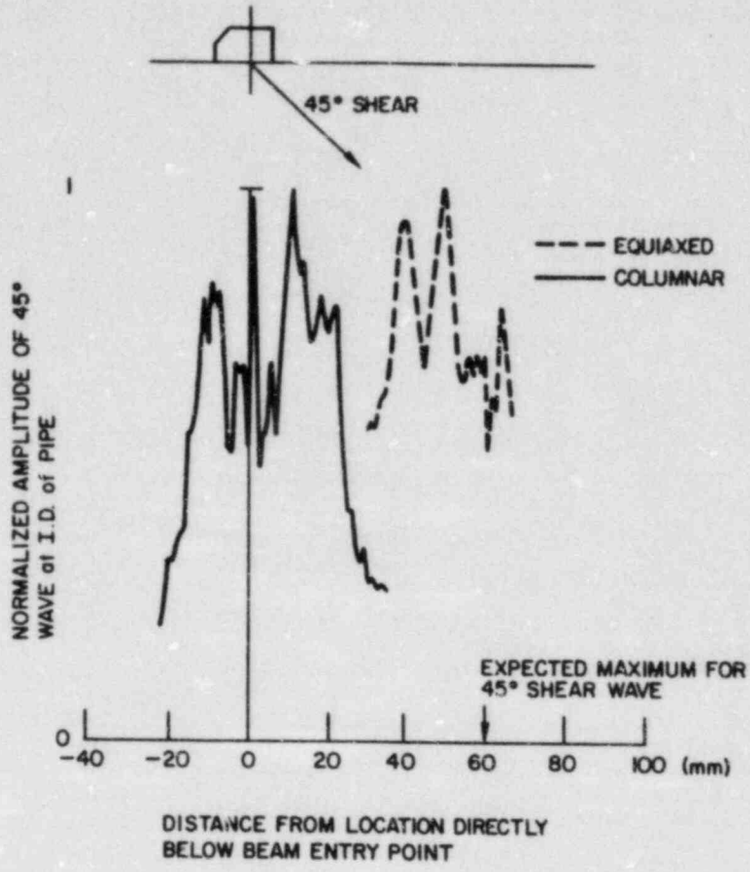

Fig. 3.4. Map of Amplitude vs Position of 1.0-MHz, 25-mm, 45° Shear-Wave Beam Transmitted through Two 60-mm-thick Cast Stainless Steel Specimens, One with Equiaxed, the Other with Columnar Grains. Expected maximum signal intensity is 16 mm from the entry position for the columnar structure. A 6-mm-dia transducer was used to receive and map the beam profile.

Seven cracks and four geometrical reflectors in Type 304 SS pipe specimens (12 to 20-in. dia) were examined with 2.25-MHz, 45° shear waves (1/4-in. miniature shear-wave transducer from Aerotech) in a pulse-echo mode. The amplitude (actually, the gain setting required to bring the echo height to 80% of full-screen height) was detertmined as a function of the skew angle θ by peaking the signal for each θ. The change in signal with θ was sharper for the geometrical reflectors than for the cracks.[4]

On the basis of this work, a probe has been designed and built that can be used with a multiscanner to provide the data needed for intergranular crack discrimination. The initial design[5] for inspection of 28-in. (0.7m)-dia pipes, makes use of seven miniature, 45°-angle shear-wave probes in a "frame", with a multiscanner and individual gain control for each channel. The gain for each element can be adjusted to compensate for decrease in amplitude with skew angle that characterizes geometrical reflectors. After the gain of the pulser-receiver is adjusted to the calibrated level, intergranular cracks may be identified by the presence of above-threshold echo signals for the transducers positioned at large skew angles; the signals at large skew angles generated by a geometrical reflector will fall below the threshold.

To test the viability of this concept the multielement skew angle (MESA) probe was used to examine 6 field-induced intergranular cracks (2 circumferential, 2 axial, and 2 skewed) and several geometrical reflectors in two samples from 28-in.-dia pipe removed from the Nine-Mile Point Reactor. A 10% notch was used as a reference. Table 3.2 indicates the MESA probe response to 10% notch used to set the thresholds. The echo amplitude from the center transducer in the array was set to trigger the threshold alarm (dark circle) while echo signals from the other transducers remain below the preset threshold and are not triggered (open circle). This pattern indicates a geometrical reflector. When a circumferential intergranular crack is examined the amplitude of the system gain is normalized to make the echo from the center transducer just exceed the alarm threshold. Strong signals from the skewed transducers, which exceed most of the thresholds (more dark circles) should reveal the crack. The MESA probe response to the cracks and several geometric reflectors is shown in Table 3.2. The results for IGSCC-Circ. 2 show the expected pattern. However, these data indicate the difficulty in demonstrating the effect, reproducing the patterns, and coupling the transducer (in part due to hand-fatigue). Attempts were made to obtain a statistical average based on many passes over the cracks and geometrical reflectors and different procedures were tried in order to optimize the results.

TABLE 3.2. MESA Probe Response for Various Reflectors in 28-in. Pipe Sections

Reflector	Trial No.	Transducer Element and Response to Threshold Level Setting[a]						
		1	2	3	4	5	6	7
10% Notch (10N)	1	0	0	0	●	0	0	0
	2	0	0	0	0	●	0	0
	3	0	0	0	●	0	0	0
	4	0	0	0	●	0	0	0
Geometry A	1	0	0	0	●	0	0	0
	2	0	0	0	●	0	0	0
	3	0	0	0	●	0	●	0
Geometry C	1	0	0	●	●	0	0	0
	2	0	0	X	●	0	0	0
	3	0	X	●	●	0	0	0
	4	0	0	0	●	0	0	0
	5	0	0	X	●	0	0	0
	6	0	0	X	●	0	0	0
	7	●	0	●	●	0	0	0
	8	0	0	X	●	0	0	0
	9	0	0	●	●	0	0	0
IGSCC-Circ. P-3	1	0	0	●	●	●	0	0
	2	0	0	0	●	0	0	0
	3	0	0	●	●	0	0	0
	4	0	0	●	●	0	0	0
	5	0	●	●	●	0	0	0
IGSCC-Circ. 2 (effect of hand fatigue)	1	●	●	●	●	●	●	●
	2	0	●	●	●	●	●	0
	3	0	●	●	●	●	●	0
	4	0	0	0	●	0	●	0
	5	0	0	0	●	0	●	0
	6	0	0	0	●	0	●	0
	7	0	●	●	●	●	0	0
IGSCC-Axial A-2 (hand fatigue indicated)	1	●	0	●	●	0	0	0
	2	0	0	●	●	0	0	0
	3	0	0	0	●	0	0	0
	4	0	0	0	●	0	0	0
	5	0	0	0	●	0	0	0
IGSCC-Axial A-1	1	0	0	0	0	0	0	0
IGSCC-Skew K-1	1	0	0	●	●	●	0	0
	2	0	0	●	●	●	0	0
IGSCC-Skew K-2	1	0	●	0	●	●	●	0
	2	0	0	0	●	●	●	●
	3	0	●	●	●	●	●	0
	4	X	0	●	●	0	●	0

[a]Multiscanner indications: 0, below threshold level; ●, exceeds threshold level; X, transition level.

Table 3.3 shows the average number of echoes that exceed the threshold (out of a possible seven) for the MESA probe used in a pulse-echo mode when probe yaw was not permitted during the scan. In the two trials indicated, the average value for the geometrical reflectors ranged from 1.2 to 1.9 while the values for the cracks ranged from 1.0 to 4.1. Based on these values the circumferential and skewed cracks are distinguishable (though barely) from the geometrical reflectors. Table 3.4 shows the results for scans in the pulse-echo mode when probe yaw was allowed. In this test one of the circumferential cracks would not be separated from the geometrical reflectors if the criterion of "number of echoes exceeding the threshold" is used. Table 3.5 shows the results from the MESA probe in the pitch-catch mode when the center transducer is used as the transmitter and the seven transducers in the array were used as

TABLE 3.3. Laboratory MESA Probe Data[a] from 28-in. Pipe Sections with Field-Induced Intergranular Cracks Using Pulse-Echo Configuration (No Probe Yaw)

Reflector Type	Identification	Average Number of Echoes Exceeding Threshold (out of 7)
Geometry	G-2	1.7
Geometry	A	1.5
Circ. IGSCC	P-3	4.0
Circ. IGSCC	2	2.0
Skewed IGSCC	K-1	2.2
Skewed IGSCC	K-2	3.4
Axial IGSCC	A-1	1.0[b]
Axial IGSCC	A-2	1.6[b]
		Geometry 1.5-1.7
		Crack 1.0-4.0
10% Notch	10N	1.0
Geometry	A	1.2
Geometry	G-AVE	1.9
Circ. IGSCC	P-3	2.2
Circ. IGSCC	2	3.9
Skew IGSCC	K-1	3.0
Skew IGSCC	K-2	4.1
Axial	A-2	1.6[b]
		Geometry 1.2-1.9
		Crack 1.6-4.1

[a]Procedure for Data Acquisition: Examine pipe with scanner set to pulse-echo using center crystal No. 4. Maximize signal from reflector by moving probe and adjust system gain to provide echo amplitude 80% FSH (just exceeding threshold). Probe yaw not allowed. Scan all seven transducers.

[b]Miscall.

TABLE 3.4. Laboratory MESA Probe Data[a] from 28-in. Pipe Sections with Field-Induced Intergranular Cracks Using Pulse-Echo Configuration with Yaw

Reflector Type	Identification	Average Number of Echoes Exceeding Threshold (out of 7)
10% Notch	10N	1.0
Geometry	G-1	2.0
Geometry	A	2.5
Geometry	C	3.5
Circ. IGSCC	P-3	3.0[b]
Circ. IGSCC	2	4.5
Skewed IGSCC	K-2	3.8
Skewed IGSCC	K-1	5.0
Axial IGSCC	A-2	4.2
Axial IGSCC	A-1	5.5
		Geometry 1.0-3.5
		Crack 3.0-5.5

[a]Procedure for Data Acquisition: Set system to run, scan, and maximize number of signals exceeding threshold; probe yaw allowed. Adjust system gain using crystal No. 4 (80% FSH). Acquire data from each reflector more than once if not reproducible.

[b]Miscall.

TABLE 3.5. Laboratory MESA Probe Data[a] from 28-in. Pipe Sections with Field-Induced Intergranular Cracks Using Pitch-Catch Configuration with Yaw

Reflector Type	Identification	Average Number of Echoes Exceeding Threshold (out of 7)
10% Notch	10N	2.3
Geometry	A	2.0
Geometry	C	1.7
Circ. IGSCC	P-3	3.8
Circ. IGSCC	2	3.6
Skew IGSCC	K-2	2.7
Skew IGSCC	K-1	1.5[b]
Axial IGSCC	A-2	0.3[b]
Axial IGSCC	A-1	2.1[b]
		Geometry 1.7-2.3
		Crack 0.3-3.8

[a]Procedure for Data Acquisition: Examine pipe with scanner and probe in pitch-catch mode transmitting from center crystal No. 4 and receiving sequentially with all 7 elements. Adjust pulse-echo from element 4 to 40% FSH (just exceeding alarm threshold). Probe yaw allowed.

[b]Miscall.

the receivers. In this case one skewed crack and both axial cracks could not be distinguished from geometrical reflectors, whereas the two circumferential cracks could clearly be identified. Finally, Table 3.6 summarizes additional results from tests with pitch-catch and pulse-echo modes. Again based on the average number of signals in the transducer array that exceed a preset threshold level, circumferential cracks can be separated from geometrical reflectors for the pitch-catch mode but not for the pulse-echo mode.

TABLE 3.6. Laboratory MESA Probe Data from 28-in. Pipe Comparing Pulse-Echo and Pitch-Catch Configurations

Reflector Type	Identification	Average Number of Echoes Exceeding Threshold (out of 7)	
		Test 1 (P-C)	Test 2 (P-C)
IGSCC	2	5.1	4.9
IGSCC	P-3	5.7	3.4
Axial IGSCC	A-1	-	2.0[a]
Skew IGSCC	K-1	-	2.0[a]
Skew IGSCC	K-2	-	2.5[a]
Geometry	A	1.5	1.9
Weld Metal	HA	2.6	1.8
Weld Metal	AA	2.8	1.8
		Geometry 1.5-2.8	
		Cracks 2.0-5.7	
		Test 1 (P-E)	Test 2 (P-E)
IGSCC	2	6.5	4.7[a]
IGSCC	P-3	3.3	2.5[a]
Geometry	A	1.8	3.7
Weld Metal	HA	4.5	3.3
Weld Metal	AA	5.2	4.3
		Geometry 1.8-5.2	
		Circ. Cracks 2.5-6.5	

[a]Miscalled.

These results point out how difficult it is to use a hand-held MESA probe and suggest that an automated scanning system may be required to generate the amount of data necessary to distinguish intergranular cracks from geometrical reflectors. Data would have to be acquired in both pulse-echo and pitch-catch configurations.

In addition to tests performed in the laboratory, the MESA probe was tested under field conditions during an outage at the Commonwealth Edison Dresden Station. Field tests carried out on two 28-in. lines showed that the effectiveness of the probe decreased when protective clothing and awkward positioning of personnel were required to carry out a pipe inspection. These tests also indicated a need for an automated scanning system to minimize the coupling problem encountered with a hand scan. A computer interface would also be necessary to log the data and analyze the skew angle versus amplitude information for the different types of transducer configurations.

D. References for Chapter III

1. W. J. Shack, T. F. Kassner, D. S. Kupperman, F. A. Nichols, J. Y. Park, and R. W. Weeks, Environmentally Assisted Cracking in Light Water Reactors: Critical Issues and Recommended Research, NUREG/CR-2541, ANL-82-2, (February 1982), pp. 3.1-3.29.

2. D. S. Kupperman et al., in Materials Science Division Light-Water-Reactor Safety Research Program: Quarterly Progress Report, NUREG/CR-2970 Vol. I, ANL-82-41 Vol. I, January-March 1982, (October 1982), pp. 9-15.

3. D. S. Kupperman, K. J. Reimann, and D. I. Kim, "Ultrasonic Characterization and Microstructure of Stainless Steel Weld Metal", in Nondestructive Evaluation: Microstructural Characterization and Reliability Strategies, O. Buck and S. M. Wolf, Eds., The Metallurgical Society of AIME, (1981), pp. 191-216.

4. D. S. Kupperman et al., in Materials Science Division Light-Water-Reactor Safety Research Program: Quarterly Progress Report, NUREG/CR-2970 Vol. II, ANL-82-41 Vol. II, April-June 1982 (May 1983), pp. 12-14.

5. D. S. Kupperman et al., in Materials Science Division Light-Water-Reactor Safety Research Program: Quarterly Progress Report, NUREG/CR-2970 Vol. IV, ANL-82-41 Vol. IV, October-December 1982 (November 1983), pp. 26-27.

Distribution for NUREG/CR-3998 Vol. I (ANL-84-60 Vol. I)

Internal:

R. Avery
G. Ayrault
M. Blander
F. A. Cafasso
O. K. Chopra
H. M. Chung
T. N. Claytor
L. W. Deitrich
D. R. Diercks
F. Y. Fradin
B. R. T. Frost
D. M. Gruen
P. R. Huebotter
T. F. Kassner (10)
K. L. Kliewer
D. S. Kupperman
P. S. Maiya
V. A. Maroni
D. K. Moores
K. Natesan
F. A. Nichols
J. Y. Park
R. B. Poeppel
K. J. Reimann
J. Rest
G. S. Rosenberg
W. E. Ruther
R. A. Scharping
W. J. Shack (3)
W. K. Soppet
E. M. Stefanski (2)
C. E. Till
R. A. Valentin
R. W. Weeks
H. Wiedersich
R. S. Zeno
ANL Patent Dept.
ANL Contract File
ANL Libraries (2)
TIS Files (6)

External:

NRC, for distribution per R5 (350)
DOE-TIC (2)
Manager, Chicago Operations Office, DOE
R. Dalton, DOE-CH
Materials Science and Technology Division Review Committee:
- B. Alcock, U. Toronto
- A. Arrott, Simon Fraser U.
- R. C. Dynes, Bell Labs., Murray Hill
- A. G. Evans, U. California, Berkeley
- H. K. Forsen, Bechtel Group, San Francisco
- E. Kay, IBM San Jose Research Lab.
- B. Maple, U. California, San Diego
- P. G. Shewmon, Ohio State U.
- J. K. Tien, Columbia U.
- J. W. Wilkins, Cornell U.

R. B. Adamson, General Electric Co., Vallecitos Nuclear Center, P. O. Box 460, Pleasanton, Calif. 94566
P. L. Andresen, General Electric Corporate Research and Development, Schenectady, N. Y. 12301
G. A. Arlotto, Office of Nuclear Regulatory Research, USNRC, Washington
D. Atteridge, Battelle Pacific Northwest Lab., P. O. Box 999, Richland, Wash. 99352
W. H. Bamford, Structural Materials Engineering, Westinghouse Electric Corporation, WNES, Box 355, Pittsburgh, Pa. 15230
W. Berry, Battelle-Columbus Labs., 505 King Ave., Columbus, OH 43201
C. Y. Cheng, Office of Nuclear Reactor Regulation, USNRC, Washington
R. A. Clark, Battelle Pacific Northwest Lab., P. O. Box 999, Richland, Wash. 99352
W. J. Collins, Office of Inspection and Enforcement, USNRC, Washington
A. Cowan, Risley Nuclear Power Development Labs., United Kingdom Atomic Energy Authority (Northern Division), Risley, Warrington WA3 6AT, UK
G. Cragnolino, Dept. of Metallurgical Engineering, Ohio State U., Columbus, OH 43210
D. Cubiciotti, Electric Power Research Inst., P. O. Box 10412, Palo Alto, Calif. 94304

W. H. Cullen, Materials Engineering Associates, Inc., 9700 B. George Palmer Highway, Lanham, Maryland 20706
J. C. Danko, Electric Power Research Inst., P. O. Box 10412, Palo Alto, Calif. 94304
B. J. L. Darlaston, CEGB, Berkeley Nuclear Laboratories, Berkeley, Glos., England
B. J. Elliot, Office of Nuclear Reactor Regulation, USNRC, Washington
M. Fox, Fox Enterprises, 7490 Stanford Place, Cupertino, Calif. 95014
Y. S. Garud, S. Levy, Inc., 1901 S. Bascom Ave., Campbell, Calif. 95008
J. H. Gittus, Springfields Nuclear Power Development Labs., U. K. Atomic Energy Authority, Springfields, Salwick, Preston, PR4 ORR, England
W. Gysel, George Fischer, Ltd., Schaffhausen, Switzerland
D. O. Harris, 750 Welch Rd., Palo Alto, Calif. 94304
W. S. Hazelton, Office of Nuclear Reactor Regulation, USNRC, Washington
B. Hemsworth, HM Nuclear Installations Inspectorate, Thames House North, Millbank, London SW1P 42J, England
R. E. Johnson, Office of Nuclear Reactor Regulation, USNRC, Washington
W. V. Johnston, Office of Nuclear Reactor Regulation, USNRC, Washington
R. L. Jones, Electric Power Research Inst., P. O. Box 10412, Palo Alto, Calif. 94304
P. M. Lang, Office of Converter Reactor Deployment, USDOE, Washington, D. C. 20545
J. Muscara, Office of Nuclear Regulatory Research, USNRC, Washington
D. M. Norris, Electric Power Research Inst., P. O. Box 10412, Palo Alto, Calif. 94304
D. R. O'Boyle, Commonwealth Edison Co., P. O. Box 767, Chicago, Ill. 60690
J. T. A. Roberts, Electric Power Research Inst., P. O. Box 10412, Palo Alto, Calif. 94304
E. J. Rowley, Commonwealth Edison Co., P. O. Box 767, Chicago, Ill. 60690
E. F. Rybicki, Dept. of Mechanical Engineering, Univ. of Tulsa, Tulsa, Okla. 74110
C. Z. Serpan, Office of Nuclear Regulatory Research, USNRC, Washington
L. Shao, Office of Nuclear Regulatory Research, USNRC, Washington
V. K. Sikka, Oak Ridge National Laboratory, P. O. Box X, Oak Ridge, TN 37830
R. D. Silver, Office of Nuclear Reactor Regulation, USNRC, Washington
G. Slama, Framatome, Tour FIAT, Cedex 16, 92084, Paris La Defense, France
P. Smerd, Combustion Engineering, Inc., P. O. Box 500, Windsor, Conn. 06095
L. J. Sobon, NUTECH Engineers, 6835 Via del Oro, San Jose, Calif. 95119
A. A. Solomon, School of Nuclear Engineering, Purdue U., West Lafayette, Ind. 47907
H. D. Solomon, General Electric Company, P. O. Box 43, Schenectady, N. Y. 12301
D. M. Stevens, Lynchburg Research Center, Babcock & Wilcox Co., P. O. Box 239, Lynchburg, VA 24505-0239
J. Strosnider, Office of Nuclear Regulatory Research, USNRC, Washington
A. Taboada, Office of Nuclear Regulatory Research, USNRC, Washington
J. R. Weeks, Brookhaven National Lab., Upton, N. Y. 11973
K. R. Wichman, Office of Nuclear Reactor Regulation, USNRC, Washington

NRC FORM 335 (2 84) NRCM 1102 3201 3202

U.S. NUCLEAR REGULATORY COMMISSION

BIBLIOGRAPHIC DATA SHEET

SEE INSTRUCTIONS ON THE REVERSE

1 REPORT NUMBER (Assigned by TIDC add Vol. No., if any)
NUREG/CR-3998 Vol. I
ANL-84-60 Vol. I

2 TITLE AND SUBTITLE
Light-Water-Reactor Safety Materials Engineering Research Programs: Quarterly Progress Report, January--March 1984

3 LEAVE BLANK

4 DATE REPORT COMPLETED
MONTH | YEAR

5 AUTHOR(S)
W. J. Shack et al.

6 DATE REPORT ISSUED
MONTH: September | YEAR: 1984

7 PERFORMING ORGANIZATION NAME AND MAILING ADDRESS (Include Zip Code)
Argonne National Laboratory
9700 South Cass Avenue
Argonne, Illinois 60439

8 PROJECT/TASK/WORK UNIT NUMBER

9 FIN OR GRANT NUMBER
A2212, A2243, A2250

10 SPONSORING ORGANIZATION NAME AND MAILING ADDRESS (Include Zip Code)
Division of Engineering Technology
Office of Nuclear Regulatory Research
U. S. Nuclear Regulatory Commission
Washington, D. C. 20555

11a TYPE OF REPORT

b PERIOD COVERED (Inclusive dates)
January--March 1984

12 SUPPLEMENTARY NOTES

13 ABSTRACT (200 words or less)

This progress report summarizes the Argonne National Laboratory work performed during January, February, and March 1984 on water reactor safety problems related to out-of-core materials. The research and development areas covered are Environmentally Assisted Cracking in Light Water Reactors, Long-Term Embrittlement of Cast Duplex Stainless Steels in LWR Systems, and Nondestructive Evaluation and Leak Detection.

14 DOCUMENT ANALYSIS - a KEYWORDS/DESCRIPTORS
embrittlement cast stainless steel
nondestructive evaluation
stress corrosion cracking
water chemistry

b IDENTIFIERS/OPEN ENDED TERMS

15 AVAILABILITY STATEMENT
Unlimited

16 SECURITY CLASSIFICATION
(This page) unclassified
(This report) unclassified

17 NUMBER OF PAGES
95

18 PRICE